



Statistical modelling of blood flow and transport in brain micro-vascular networks

Florian Goirand

► To cite this version:

Florian Goirand. Statistical modelling of blood flow and transport in brain micro-vascular networks. Fluids mechanics [physics.class-ph]. Institut National Polytechnique de Toulouse - INPT, 2021. English. NNT : 2021INPT0060 . tel-04170869

HAL Id: tel-04170869

<https://theses.hal.science/tel-04170869>

Submitted on 25 Jul 2023

HAL is a multi-disciplinary open access archive for the deposit and dissemination of scientific research documents, whether they are published or not. The documents may come from teaching and research institutions in France or abroad, or from public or private research centers.

L'archive ouverte pluridisciplinaire **HAL**, est destinée au dépôt et à la diffusion de documents scientifiques de niveau recherche, publiés ou non, émanant des établissements d'enseignement et de recherche français ou étrangers, des laboratoires publics ou privés.



THÈSE

En vue de l'obtention du

DOCTORAT DE L'UNIVERSITÉ DE TOULOUSE

Délivré par :

Institut National Polytechnique de Toulouse (Toulouse INP)

Discipline ou spécialité :

Dynamique des fluides

Présentée et soutenue par :

M. FLORIAN GOIRAND

le vendredi 18 juin 2021

Titre :

Statistical modelling of blood flow and transport in brain micro-vascular networks

Ecole doctorale :

Mécanique, Energétique, Génie civil, Procédés (MEGeP)

Unité de recherche :

Institut de Mécanique des Fluides de Toulouse (IMFT)

Directeur(s) de Thèse :

MME SYLVIE LORTHOIS

M. TANGUY LE-BORGNE

Rapporteurs :

M. GWENNOU COUPIER, UNIVERSITE GRENOBLE ALPES

MME KAREN ALIM, TECHNISCHE UNIVERSITAT MUNICH

Membre(s) du jury :

M. PHILIPPE DAVY, UNIVERSITE RENNES 1, Président

MME SYLVIE LORTHOIS, TOULOUSE INP, Membre

M. OLIVIER BENICHOU, UNIVERSITE SORBONNE, Membre

M. TANGUY LE-BORGNE, UNIVERSITE RENNES 1, Membre

Statistical modelling of blood flow and transport in brain micro-vascular networks

Florian Goirand

July 7, 2021

One hand washes the other and both wash the face.

To my grandfather, my buddy, Louis.

Acknowledgments

First, I would like to thank the European Research Council for its financial support without which it would have been way more difficult to make this PhD project concrete. I also thank the whole administrative and scientific staffs of the Institut de Mécanique des Fluides de Toulouse (IMFT) and of the Observatoire des Sciences de l'Univers de Rennes (OSUR) for having provided the best conditions of work in this splitted organization. More specifically, I would like to thank the IT service of the IMFT for its high responsiveness to the problems I had with my machine along these years.

I warmly thank our research collaborators Marco Dentz (IDAEA-CSIC, Barcelona), Olivier Giraud (LPTMS, Saclay) and Bertrand Georgeot (LPT, Toulouse). In the context of the collaboration with Olivier Giraud and Bertrand Georgeot, I thank the LPTMS for its kind hospitality for a 10 days work visit. I also thank Satya Majumdar (LPTMS), that I have met during this visit, for interesting and illuminating discussions about the q-model. I also thank my teaching collaborators Martin Strecker (IRIT, Toulouse) and Marc Miscevic (LAPLACE, Toulouse) who provided me the opportunity to acquire a first teaching experience in ideal conditions.

Moreover, I would like to thank all the members of the ReactiveFronts and BrainMicroFlow teams for their scientific, and non-scientific, discussions that created a real synergy around these two projects. More specifically, I would like to thank Maxime Berg, Adlan Merlo and Myriam Peyrounette (BrainMicroFlow - IMFT) and Hugo Sanquer, Mélissa Garry, Tomás de Campos Aquino and Nicolas Waisbord (ReactiveFronts - OSUR).

Finally, I would like to give a special thank to my advisors Sylvie Lorthois (IMFT) and Tanguy Le Borgne (OSUR) for their support along these years that have not always been easy specially since the Covid-19 outbreak. I thank them for their solidarity and their involvement in the realization of this thesis work.

Preamble

How does brain work? Four words, a simple question and thousands of years of studies to unravel how this unique organ allows the emergence of consciousness in complex living matter. From the first description of the structure of the brain back in the Ancient Egypt¹, our knowledge of the mechanisms allowing brain functions considerably increased. Nowadays, one of the most important challenges to answer this question is the design of an accurate description of the feeding of brain cells. The design of such a description is challenging by the large amount of sources of complexity at stake in the brain. First, brain cells are fed by a network of blood vessels which is complex by its architecture and the variability of the size of the vessels composing it. Inside the brain, the vascular network is made of hundreds of millions of microscopic vessels. Furthermore, blood, which effectively carries vital chemical species like oxygen or nutrients, is a fluid exhibiting peculiar physical properties. Finally, the production of the energy necessary for brain cells to ensure their function involves complex (bio-)chemical reactions. As a consequence, this challenge has to be tackled accounting for numerous fields of science like medicine, biology, neurosciences, chemistry, fluid mechanics, graph theory etc... each exhibiting its own conceptual and/or technical issues. As a transverse framework, statistical physics appears to be an appropriate tool to bind together these various fields to offer an operational description of the cerebral blood flow properties.

Beyond scientific interest, an accurate description of the mechanisms of blood supply to brain cells is required to understand the emergence of brain pathologies associated to vascular impairments. These pathologies represent a real public health issue specially in developed countries. In France, we indeed estimate to about 140.000 each year the number of new CerebroVascular Accidents (CVAs). With a fatality rate of 20%, CVAs are the first cause of death for women. At the world scale, according to 2010 World Health Organization (WHO) figures, the number of victims of CVAs is evaluated to 17 millions with a fatality rate of one third and is considered as the second cause of mortality. Extrapolating its current increase, stroke incidence at the global scale is expected to reach about 80 millions in 2030². In addition to this high lethality rate, surviving people often experiment long time sequelae like motor function and/or cognitive deficits leading to a significantly increased risk of developing dementia. Dementia is also a common aspect of numerous neuro-degenerative diseases, the best known and most common of which is Alzheimer's Disease (AD). In 2015, 900.000 AD cases have been identified in France and more than 35 millions worldwide. According to WHO, the latter is expected to almost double every 20 years³. More generally, also according to WHO, the incidence of overall dementiae is expected to reach more

¹<https://blogs.ucl.ac.uk/researchers-in-museums/2018/02/21/neuroscience-in-ancient-egypt/comment-page-1/>

²<http://www.fondation-recherche-avc.org/frequence>

³<https://alzheimer-recherche.org/la-maladie-alzheimer/quest-maladie-dalzheimer/definition-et-chiffres/>

than 150 millions cases in 2050⁴. This public health challenge, coupled to the economic question of the dependency of patients, requires innovant early detection and therapeutic strategies for these pathologies and consequently, an important long term investment of the scientific community on this issue.

In this context a collaboration between Sylvie Lorthois, specialist in brain (fluid) mechanics, and Tanguy Le Borgne, specialist in the statistical description of (reactive) transport in geological fractured and porous media, has emerged taking this thesis as an anchorage point. The two environments of the Institut de Mécanique des Fluides de Toulouse (IMFT) and the Observatoire des Sciences de l'Univers de Rennes (OSUR) offered multiple stimulating point of views to tackle this innovative analysis of brain blood supply with the organizational counterpart of spending approximately 18 months in Toulouse and 18 months in Rennes. These environnements also provided the opportunity for developing enriching collaborations with, on one hand, Marco Dentz (IDAEA-CSIC, Barcelona) and, on the other hand, Oliver Giraud (LPTMS, Saclay) and Bertrand Georgeot (LPT, Toulouse). This thesis has been funded under the European Research Council (ERC) grants agreements 615102 (BrainMicroFlow) and 648377 (ReactiveFronts). This thesis work contains two papers that have already been submitted to peer-reviewed journals and which are currently under review. Furthermore, part of this work has been presented into several international conferences.

⁴<https://www.pasteur.fr/fr/centre-medical/fiches-maladies/alzheimer-maladie>

Contents

1	State of the art	9
1.1	The cerebral blood circulation	9
1.2	Modelling brain micro-circulation	13
1.3	Statistical models for flow and transport in disordered media	19
1.4	Objectives and outline	24
2	Blood flow organization and effective transport models	27
2.1	Blood flow and transport statistics modelling	27
2.2	Conclusion and perspectives	67
3	Random network flow statistics model	69
3.1	Preliminary observation	69
3.2	The mean-field q-model: theory and simulations	71
3.3	q-model and flow organization	75
3.4	Beyond the mean-field approximation	79
3.5	Conclusion and perspectives	82
4	Impact of occlusions on blood flow organization	83
4.1	Preliminary observations	83
4.2	Single occlusion	85
4.3	Successive occlusions	99
4.4	Perturbations induced by capillary occlusions	103
4.5	Conclusion and perspectives	105
5	General conclusion and perspectives	107

Chapter 1

State of the art

In this first chapter, we introduce key elements of the existing literature about the cerebral blood micro-circulation. Along this manuscript, these elements serve as a base to define the scientific context which motivates the different facets of this thesis work. From basic aspects of brain vascular anatomy, we primarily highlight the essential role of blood circulation in maintaining an optimal functioning of brain cells through the regulation of physical and chemical conditions. In a second part, we present the state of the art of pre-existing models of blood flow at the micro-vascular scale. Finally, we introduce some classical frameworks of statistical physics to model flow and transport into disordered porous media. We will show how these frameworks enable to relate micro-vascular structure to blood flow and transport properties within both qualitative and quantitative approaches, providing novel perspectives to understand the brain micro-circulation.

1.1 The cerebral blood circulation

Blood circulation is crucial in humans, but similarly in most complex life forms, as it plays a key role in cell homeostasis, i.e. blood circulation maintains numerous physical and chemical quantities under physiological conditions. Hence, its task is to transport vital chemical species (e.g. oxygen, nutrients, hormones...), but also cells of the immunitary system, from their dedicated production or absorption organs towards the rest of the body. Conversely, it ensures the removal of toxic species (e.g. metabolic wastes), from all the body towards the filtration organs. Blood circulation is furthermore involved in temperature regulation. Impulsed by the heart beat, blood flows from the heart to organs, and reciprocally from organs to the heart, through a collection of vessels known respectively as arteries and veins.

In the human brain, blood is supplied and drained to and from the brain by a complex network of arteries and veins which can be roughly decomposed as follows. Fresh blood supply is ensured by three principal arteries: anteriorly, a pair of Internal Carotid Arteries (ICAs) and, posteriorly, the Basilar Artery (BA). These three arteries meet at the base of the brain to form a redundant anastomotic structure called the circle of Willis (Fig. 1.1a) [1]. Three pairs of cerebral arteries emerge from the circle of Willis: the Anterior Cerebral Arteries (ACAs), the Middle Cerebral Arteries (MCAs), and the Posterior Cerebral Arteries (PCAs). All together, the ACAs, MCAs and PCAs effectively supply the brain in blood. These three arteries and their sub-branches manage this supply by meshing the surface of the brain, or pial surface, and the falx cerebelli¹ in

¹The falx cerebelli is a membrane separating the two cerebral hemispheres.

the deep brain (Fig. 1.1b) [2]. The overall redundancy of this arterial network allows increased resilience of the blood supply in case of arterial stenoses or thromboses [3,4]. Conversely, blood is collected back from the brain by a dense venous system differentiating mostly from arterial system by its much less redundant structure [2]. From the pial surface and the deep brain, tree-like veins merge together and drain blood to an ensemble of large cerebral veins which structure the whole brain venous system: the dural sinuses. Finally, with no venous equivalent of the circle of Willis, blood from dural sinuses flows directly into a unique pair of neck veins, known as Internal Jugular Veins (IJVs), before being recollected into the central circulatory system (Fig 1.2).

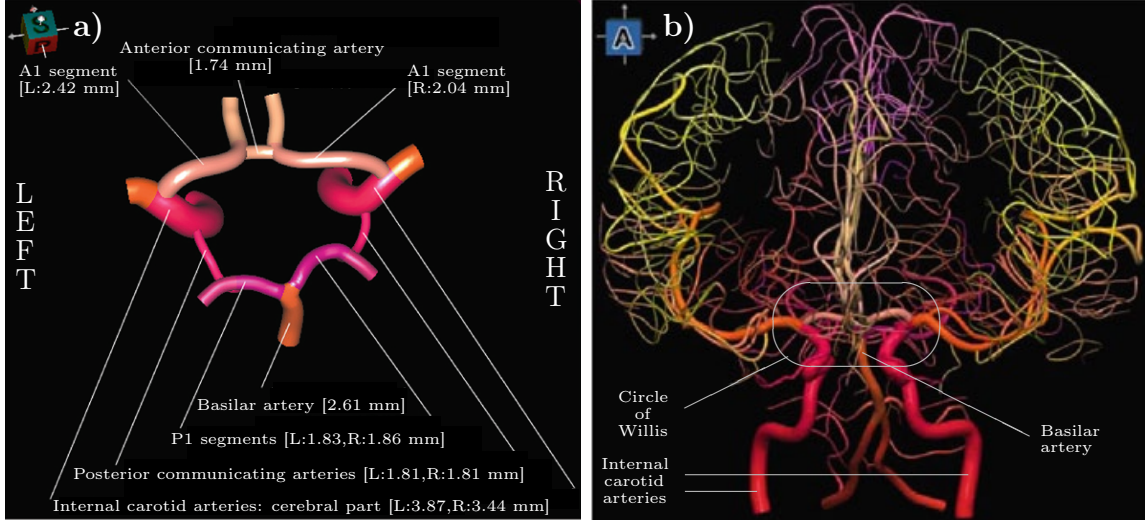


Figure 1.1: **The brain arterial network forms a redundant structure in charge of the blood supply.** a) A 3D reconstruction of the Circle of Willis ensuring the redundancy of the arterial network at the base of brain (adapted from [1]). b) Anterior view of a 3D reconstruction of the whole brain arterial system (adapted from [1]).

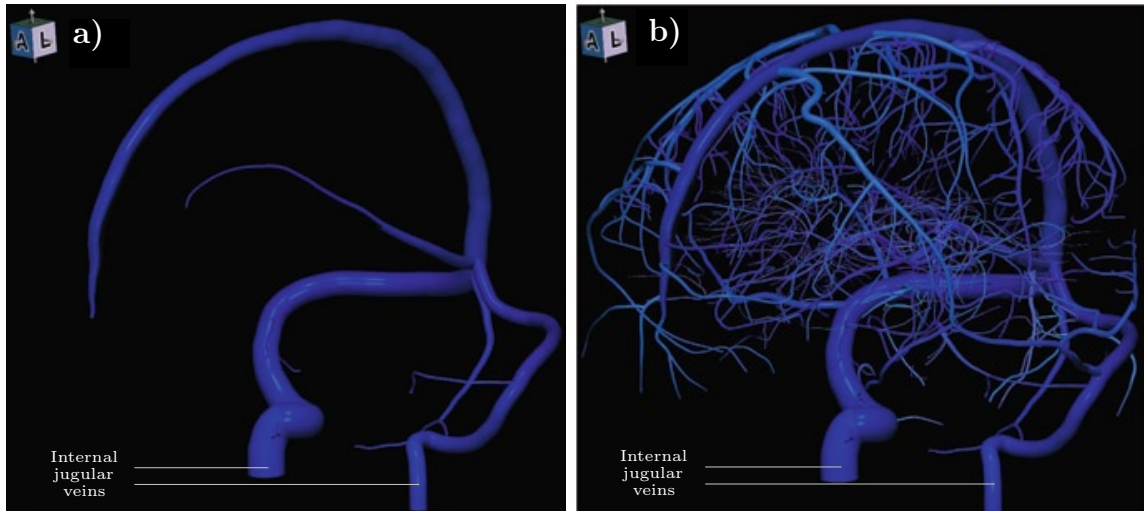


Figure 1.2: **The brain venous network forms a tree-like structure in charge of the blood draining.** a) Lateral view of a 3D reconstruction of the dural sinuses structuring the brain venous system (adapted from [1]). b) Lateral view of a 3D reconstruction of the whole brain venous system (adapted from [1]).

In this thesis, we focus on the outer thin layer of the brain which is irrigated and drained by the pial arterial and venous networks: the cortex [5]. Also called gray matter, the cortex, only 1 to 4.5 mm thick in humans, has a fundamental role in cognition as it contains the nuclei of the cells responsible for information processing, the neurons. The cortex surrounds an other type of tissue, the white matter, whose function is to mediate the communication between the different regions of the brain by the intermediary of nervous fibers, or tracts (Fig. 1.3). The colorimetric distinction between white and gray matters is mainly due to a large difference in the vascularization of these two tissues as the vascular density in the gray matter is up to two times larger than in the white matter [6]. This difference of vascular density might also hide dissimilarities in the structural properties of the vascular network, e.g. topology, in the white matter. This observation highlights the necessity of a careful transposition of the outcomes of this work to other regions of the brain than the gray matter.

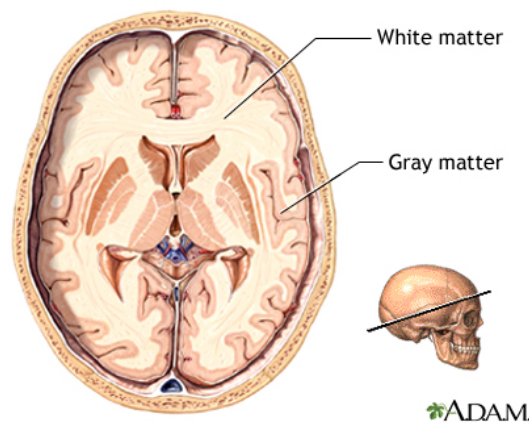


Figure 1.3: **The brain cortex is a thin layer (1 to 4.5 mm in humans) located in the outer part of the brain.** Drawing of a longitudinal brain slice highlighting white and gray matters (source: Animated Dissection of Anatomy for Medicine).

As both arterial and venous superficial networks develop, they intertwine at the surface of the cortex. Moreover, while arteries and veins ramify, they see both their diameter and length considerably decrease (Fig. 1.4a). When they reach a characteristic range of diameters, 10 to 75 microns and 20 to 120 microns in humans respectively, they dive within the gray matter generating a rather uniform spatial distribution of low-spaced blood flow inlets and outlets, respectively, at the cortical surface [2]. This order of magnitude of vessel diameters marks the edge of the micro-circulation and consequently the literature commonly refers to arteries and veins as arterioles and venules. From here, both arterioles and venules start to divide in a tree-like fashion. Akin to arteries and veins, arterioles and venules see both their length and diameter decrease as they ramify (Fig. 1.4b) [7].

Arterioles and venules are connected together by a dense and space-filling network of thin vessels, or capillaries, with diameters smaller than 10 microns in humans. The topology of this network of capillaries, or capillary bed, completely differs from the structure of arterioles and venules [7] (Fig. 1.5). Here, the tree-like organization of the latter is replaced by a mesh-like, or looped, network with local community structure [8, 9]. This dense space-filling structure is crucial to deliver blood to brain cells almost cell-by-cell [9, 10]. Interestingly, the structure of the capillary bed is quite similar accross mamalian species [8]. Hence, the use of animal models,

like mouse models, opens new avenues potentially relevant for the understanding of human blood micro-circulation.

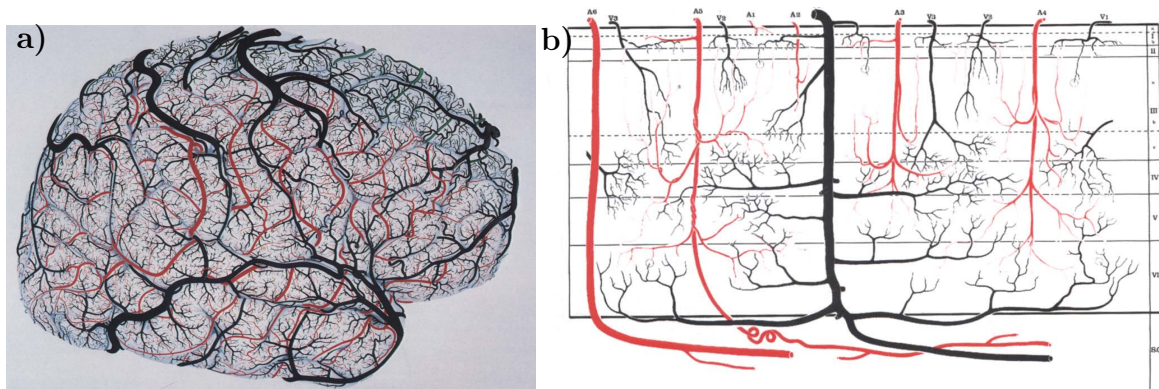


Figure 1.4: **Interwining arterial and venous networks define a rather uniform spatial distribution of low-spaced inlets and outlets at the cortical surface.** a) Drawing of a lateral view of the arterial and venous systems running over the cortical surface of the human brain. Tributaries of the middle cerebral artery are shown in red, tributaries of the anterior cerebral artery in green, tributaries of the posterior cerebral artery in blue and veins in black (extracted from [2]). b) Drawing of the diving of the arteriolar and venular sub-branches in depth of the cortical layer. Arterioles are shown in red, venules in black. The deepest region corresponds to sub-cortical white matter (extracted from [2]).

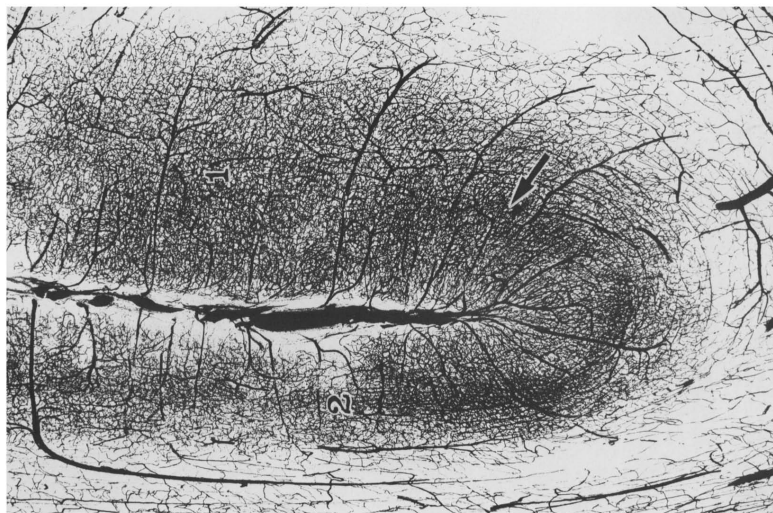


Figure 1.5: **The cortical capillary bed forms a dense mesh-like and space-filling network connecting arterioles and venules.** Micro-vascularisation in the vicinity of the central sulcus (extracted from [2]).

In addition to carrying blood to brain cells, the micro-vasculature plays an active role in the regulation of the Cerebral Blood Flow (CBF). For instance, the activation of a region of the cortex has been shown to be associated to a local increase of the CBF highlighting the coupling between neuronal activity and blood supply, a phenomenon known as neuro-vascular coupling [11]. First, the regulation of the CBF has been shown to be mediated by dilations or contractions of smooth

muscle cells, or myocytes, present in the walls of the perfusing arterioles [11–13]. Moreover, more recent studies tend to prove that capillaries also play an active part in neuro-vascular coupling and even that capillary dilation precedes arteriolar dilation [14]. Capillary dilation is made possible by the relaxation of contractile cells wrapping the capillaries, the pericytes. Conversely, abnormal contraction of the pericytes after a pathologic decrease of the oxygen concentration in brain tissues, also called ischemia, prevents the normal re-establishment of flow after stroke [14]. More generally, alterations of the micro-vascular networks, such as vessel shrinkage or occlusions, and their impact on blood flow is still an active field of research, especially in the context of understanding the onset and/or progression of Alzheimer’s disease [4, 11, 15–21].

1.2 Modelling brain micro-circulation

The design of micro-circulation models is a key step in the determination of the main physical mechanisms driving brain blood supply. Where the decomposition of a complex phenomenon into independent physical processes is not always accessible for experimentalists, models offer this possibility in order to perform a quantitative analysis of the impact of the modification of one parameter on another into a controlled framework defined by more or less sophisticated principles. The predictions emerging from such models hence guide the understanding of the dominant physical mechanisms leading to experimental observations. The amount of sources of complexity at stake in brain micro-circulation makes particularly interesting the use of such models. In the following, we present the evolution of micro-circulation models conjointly to the technical issues that have conditioned their design.

The principal challenge in the design of brain micro-circulation models is to have of a sufficiently accurate knowledge of the blood flow organization within the brain micro-vasculature. In that extent, along the years, a wide variety of imaging techniques have been developed or adapted to perform quantitative measurements of hemodynamic quantities like CBF or Red Blood Cell (RBC) velocities. The first measurements of statistics of hemodynamic quantities in brain micro-vascular networks of rodents date back to the end of the 70’s and the beginning of the 80’s [22, 23]. Thanks to classical light microscopy, these studies highlighted the presence of blood flow heterogeneities in the first micron decades of the cortex.

The development of the first minimally invasive imaging techniques few years later was a turning point in the way to tackle brain micro-circulation. Since the early 80’s, Positron Emission Tomography (PET) and, a decade later, functional Magnetic Resonance Imaging (fMRI) provided the first maps of the CBF organization at the brain scale [24–26]. On one hand, these techniques allowed to extensively study neuro-vascular coupling, initially speculated in 1890 [27], by imaging for instance the patterns of modification of the CBF and/or of brain metabolism induced by regional neuronal activations (Fig. 1.6). On the other hand, they allowed to assess the simultaneity of the blood flow decrease with cognitive decline in neuro-degenerative diseases and notably in Alzheimer’s [11, 15, 16]. The low invasivity and the ability to image the blood flow organization in the whole brain have made of these techniques a privileged tool for clinical detection of such diseases [17, 28]. However, for the time being, the characteristics of these imaging techniques go hand in hand with limited spatial resolutions to about one millimeter [29]. This limitation of the spatial resolution prevents PET and fMRI to image the whole blood flow organization within the micro-vasculature and it largely influenced the design of micro-circulation models in this period. Hence, the theoretical models developed between the beginning of the 80’s until the beginning of the 2000’s did not account for the complexity of micro-vascular structure. Instead,

these models consider the brain as a set of coarse compartments exchanging chemical species and in particular oxygen [30–34]. Useful notably to interpret and provide mathematical foundations of the observations made by PET and fMRI techniques, these spatially coarse-grained approaches nevertheless neglect local blood flow heterogeneities.

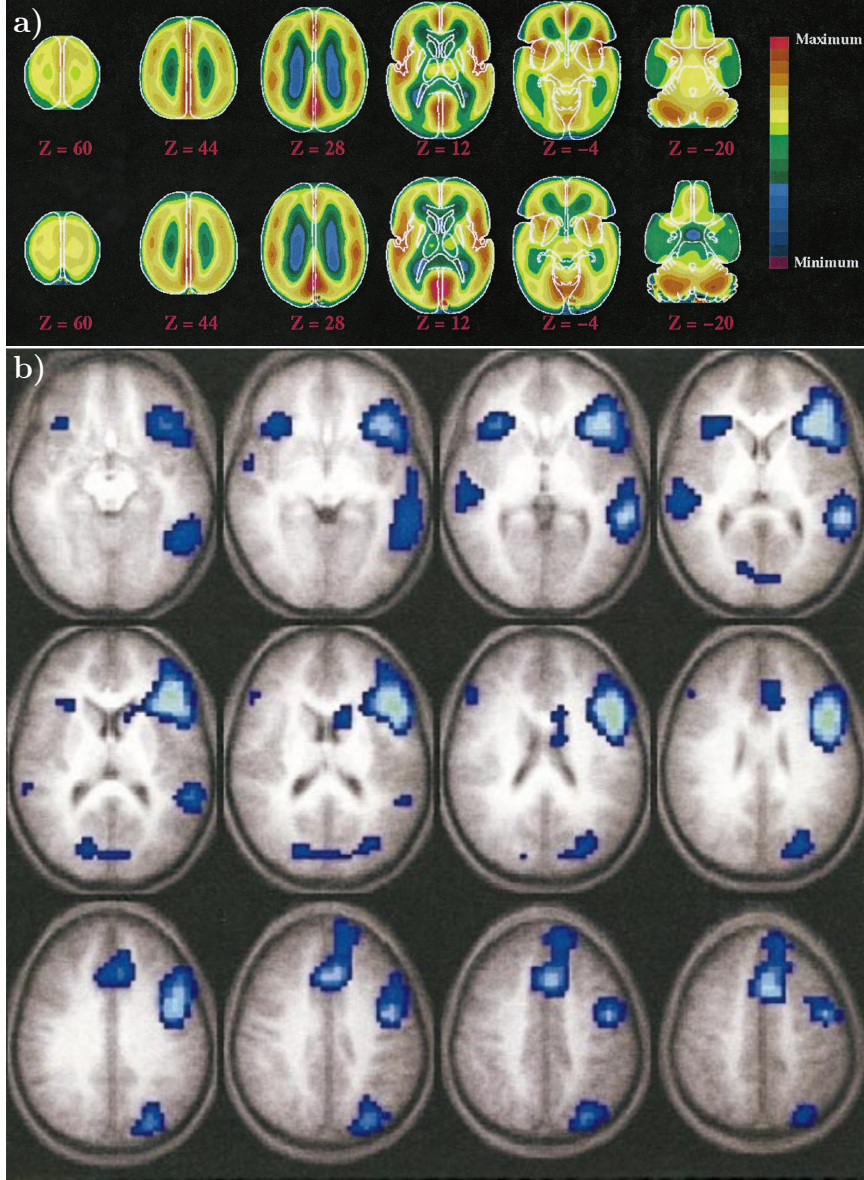


Figure 1.6: Minimally invasive imaging techniques like Positron Emission Tomography (PET) or functional Magnetic Resonance Imaging (fMRI) provides a coarse-grained description of the blood flow organization and/or of the metabolism at brain scale. **a)** PET imaging of blood flow (top) and oxygen consumption (bottom) at different depths for a subject at rest with eyes closed (extracted from [35]). **b)** fMRI of the formation of blood flow patterns during verb generation task (extracted from [36]).

During the 90's, the question of accounting for micro-circulation heterogeneities saw a renewed interest motivated notably by the will to improve the determination of the CBF from PET and fMRI. Based on the measure of the activity of radioactive tracers, like ^{15}O or ^{18}F , for PET

and on the variation of the magnetical susceptibility of hemoglobin due to deoxygenation for MRI, the determination of the CBF requires an *a priori* function linking uptake dynamics to the “local” concentrations of this contrast agent. This function, sometimes called transfer function [37], describes the statistics of time spent by contrast agents within the micro-vasculature and encodes the transport dynamics at stake within the micro-circulation. The choice of this function has been shown to impact significantly the quantification of the CBF. In this context, novel experiments have been developed to characterize accurately the transit time distribution of tracers within the micro-vasculature, the bolus experiments [38, 39].

With the improvement of imaging techniques, like confocal microscopy [40] and few years later Multi-Photon Microscopy (MPM) (see [41] for the historical paper and [42] for a review), the characterization of blood flow heterogeneities took a step forward. These techniques allowed to measure for the first time hemodynamic quantities with unprecedented micron-resolved accuracy and imaging depth in rodent brains [40, 43, 44]. These studies notably emphasized the heterogeneity of the blood velocity by direct measurements of RBC velocities and the dispersion of contrast agent travel times within the micro-vasculature thanks to enhanced bolus experiments. In parallel, blood flow models on simplistic networks [12, 45] provided the first fundamental aspects linking the blood flow organization and the micro-vascular structure. Even if yet not well understood, mainly due to the lack of physical description of blood flow organization into accurate micro-vascular networks, the interplay between local dynamic heterogeneities and dispersion of network travel times, has been embedded into a simple empirical micro-circulation model: the Capillary Transit Time Heterogeneity (CTTH) model [46]. The model parametrization is deduced empirically either by considering that the distribution of vessel transit times is equal to the distribution of travel times within the micro-vasculature or fitting the empirical travel times distributions obtained by bolus experiments with a gamma function [44, 46]. Hence, the CTTH model provides an analytical description of the distribution of travel times within the micro-vascular networks, which can be of use in the context of blood flow imaging, but has important conceptual limitations. First, the correspondance between vessel transit times and network travel times is not guaranteed as it is not based on topological or mathematical foundations. Secondly, because of the lack of physical interpretations of the dynamics at stake in the micro-vascular networks, it is difficult to evaluate the errors induced by the empirical calibration of the model. In particular, the travel time distributions obtained experimentally by *in vivo* bolus experiments in rodents is masked in the long time regime (>5 s) by the recirculation of the contrast agents [44]. Nevertheless, this model highlights the impact of transport heterogeneities on brain metabolism with potentially detrimental consequences in the case of excessive heterogeneities, a process called malignant CTTH [20, 46]. The limitations of this model highlight the necessity of designing a unified theoretical framework unraveling the role of micro-vascular network structure in the emergence of heterogeneous blood flow and transport properties. Such a theoretical framework may help to improve post-processing of brain fMRI and PET and to make a step forward in the understanding of neurovascular brain pathologies.

Fortunately, the development of novel *ex vivo* [47–49] and *in vivo* [50–52] digitalization techniques of cortical micro-vascular networks in the 2000s opened new avenues for the study of blood flow and transport heterogeneities. These techniques allow notably to perform highly-resolved blood flow simulations in anatomically accurate micro-vascular networks. In this following, the essential concepts underlying such simulations are presented.

At the micro-vascular scale, blood flow properties drastically change in comparison to the ones of the macro-circulation and accurate simulations should account for it. First, micro-

circulation is no longer characterized by the periodic dynamics impulsed by the heart beat [53]. Secondly, at this scale, blood exhibits peculiar rheological properties. Blood is constituted by soft and deformable Red Blood Cells (RBCs), among other corpuscles, in suspension into plasma, a newtonian fluid exhibiting barely the same rheological properties than water. As a suspension, blood rheological properties are influenced by the size of the vessels in which it is flowing. This is particularly true in the micro-circulation where the diameter of vessels reaches the order of magnitude of the size of the RBCs. Hence, the blood non-newtonian properties give rise to three major effects:

- The Fåhræus effect (Fig 1.7). On one hand, RBCs are excluded from the regions close to the vessel walls resulting in the presence of a cell-free layer [54]. On the other hand, these regions are influenced by no-slip boundary condition at the vessel walls inducing a gradient between average blood flow and RBC flow velocities. This results in a non-linear relation between the tube hematocrit, defined as the volumic fraction of RBCs in vessels, and the discharge hematocrit, defined as the ratio of the RBC flow rate over the whole blood flow rate [55].

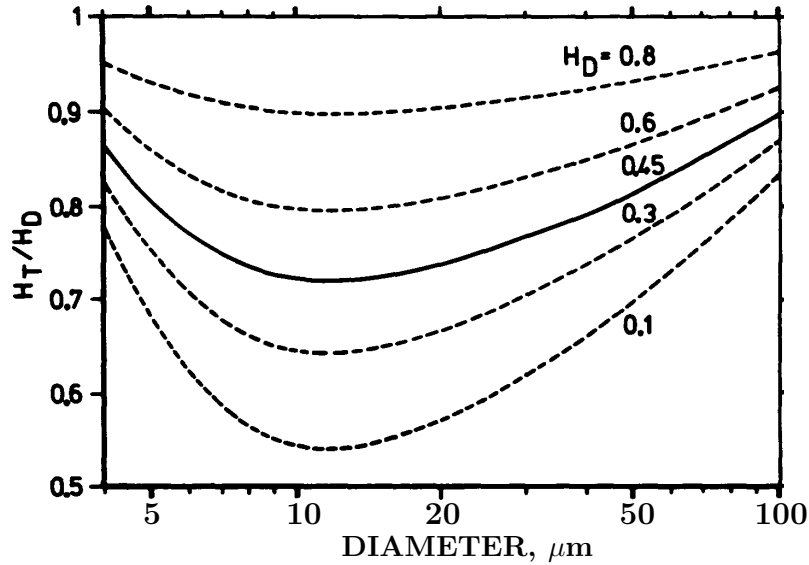


Figure 1.7: **Blood flow velocity gradients in vessels induce a non-linear relation between RBC fraction and RBC flow fraction (the Fåhræus effect).** Plot of the evolution of the ratio between tube H_T and discharge H_D hematocrits as a function of the vessel diameter for different values of H_D (adapted from [56]).

- The Fåhræus-Lindquist effect (Fig 1.8). As a colloidal suspension, blood is subject to jamming effects tending to increase its viscosity with RBC fraction (or tube hematocrit) [57]. Fortunately, the high deformability of RBCs and the presence of the lubricating cell-free layer close to the vessel walls counterbalance partly these jamming effects.

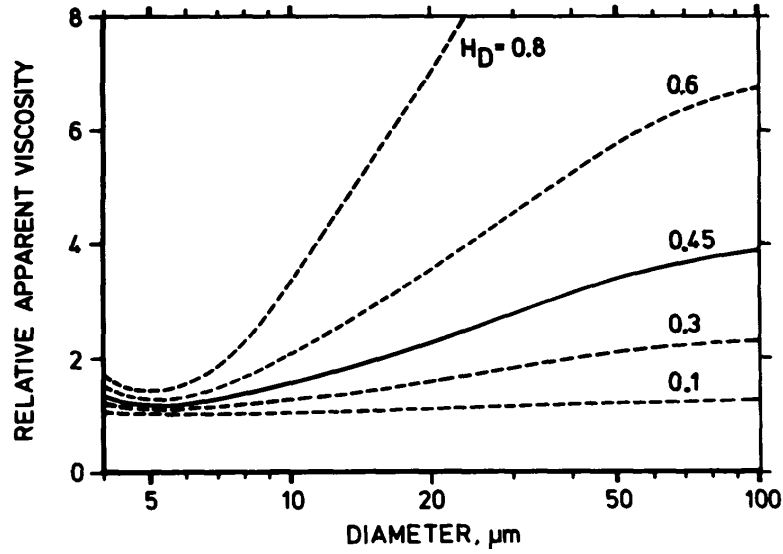


Figure 1.8: Blood viscosity is sensitive to RBC concentration and vessel diameter (the Fåhræus-Lindquist effect). Plot of the evolution of blood relative apparent viscosity with discharge hematocrit H_D and vessel diameter (extracted from [56])

- The phase separation effect (Fig 1.9). The repartition of RBCs at bifurcations does not necessarily follow the flow rate repartition. This effect tends to favor RBCs to enter downstream vessels with the largest flows and diameters [58].

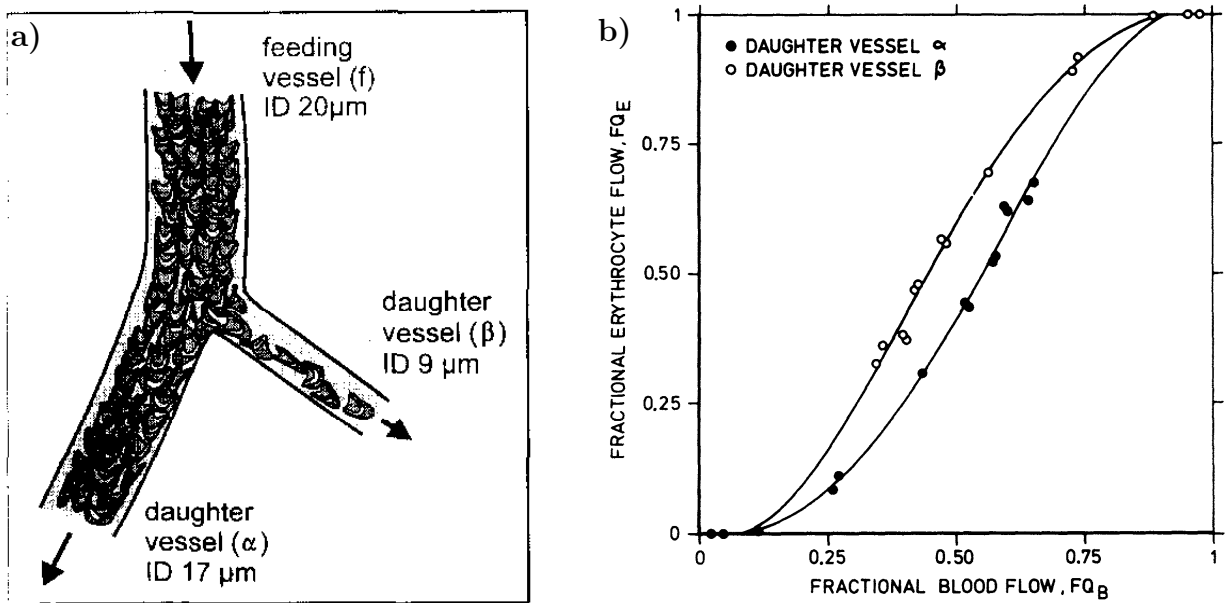


Figure 1.9: RBCs are distributed disproportionnally to blood flow repartition at bifurcations (the phase separation effect). a) Sketch of the RBC repartition between two vessels of different diameters at a bifurcation (extracted from [59]). b) Plot of the RBC flow fraction as a function of the blood flow fraction in vessels downstream to a bifurcation (extracted from [56]).

Linking the emergence of such rheological properties to individual and/or collective cell mechanics

and/or dynamics is still an active field of research and is in particular the subject of various direct numerical simulations [60]. Nevertheless, handling the whole complexity of RBC dynamics in large micro-vascular networks is very computationally expensive² [61–63]. That is why, since 1990, a numerical set up has been proposed in order to compute blood flow in the rat mesentery³ in a computationally effective way. This scheme accounts for the blood rheological properties and has been verified by comparison to experiments with good statistical agreement [56]. The method consists in considering blood as a single phase fluid with an apparent viscosity depending on its composition in RBCs and on the geometrical properties of the vessel through which blood is flowing. The model is calibrated thanks to empirical laws quantifying the three above effects. Hence, it is possible to adapt the classical Poiseuille law for single phase fluid [64] in order to compute the blood flow Q through a vessel ij accounting for the presence of RBCs in suspension (see e.g. [65]), resulting in the following system of equations:

$$\forall ij, \left\{ \begin{array}{l} Q_{ij} = \frac{\pi d_{ij}^4}{128 \mu_{ij} l_{ij}} \Delta P_{ij} \\ \sum_j Q_{ij} = 0 \end{array} \right. \quad (1.1)$$

where d_{ij} , μ_{ij} , l_{ij} and ΔP_{ij} are respectively the diameter, blood apparent viscosity, length and pressure drop associated to vessel ij and j denotes the ensemble of vertices connected to vertex i by vessels ij . As the RBC fraction depends on the flow values, due to phase separation effects, and given the retro-action of the RBC on local resistance of vessels *via* a modification of the viscosity, this system is solved iteratively. Because of the difficulty to access digitized accurate micro-vascular networks, the first applications of this numerical framework to brain micro-circulation were implemented two decades after its development [66–69]. The results of this type of simulations have notably led to the design of hybrid discrete-continuum models for blood flow organization justified by the topological properties of the micro-vascular networks [70, 71]. In these papers, the idea is to treat tree-like arterioles and venules on a discrete footing whereas space-filling homogeneous capillary bed is treated as a continuous medium by the use of volume-averaging techniques (see e.g. [72]).

In this thesis, based on numerical simulations following this single phase fluid approach [21, 73], we analyze the statistical properties of blood flow and transport into large mouse micro-vascular networks. Notably, we take advantage of this numerical setup to investigate the long time transport dynamics in the brain micro-vasculature, which is totally unknown for now. Furthermore, the impact of vessel occlusions on flow organization can be precisely analyzed thanks to a tunable complexity of micro-vascular networks. From this analysis, our goal is to provide for the first time a statistical physics framework relating blood flow and transport properties to the structure of the brain micro-vascular networks in their full complexity. As we shall see, similar questions have been investigated intensively in the field of porous and disordered media. Thus, in the next Section, we take a step back and seek inspiration from the theoretical frameworks developed in this context.

²For recall, the human cortex is filled with more than 10 billions of vessels and even more RBCs.

³The mesentery is a part of the abdomen much more accessible and structurally less complex than the brain microvasculature.

1.3 Statistical models for flow and transport in disordered media

The characterization of flow organization into porous media and its consequences on transport have been an intensive field of research over the past decades driven primarily by petroleum engineering and water resource research [74, 75]. More recently, the concepts and methods developed for geological porous media have started to be applied in biological systems [76]. In this short review, we focus on two major questions that have received a lot of interest in the past decades: How does the topological structure of the porous medium influence or determine the flow organization? What is the relation between the flow organization and the transport properties? A supplementary question, particularly relevant in the context of the morphogenesis of biological systems [77], can be added to the two previous ones: How does the flow influence in return the structure of the medium? These fundamental questions have driven the design of several theoretical frameworks along the years. In the context of this thesis, we focus on the two first questions presented above.

In this section, we thus present three theoretical frameworks which contributed to answer these questions: the Continuous Time Random Walk (CTRW) [78], the q-model [79] and the percolation theory [80]. They constitute a theoretical base upon which we develop our own blood flow and transport models as these frameworks are not sufficient by themselves to describe the blood flow properties in brain micro-vascular networks. The choice of these frameworks relied on their ability to provide relevant answers to some of the challenges raised by the study of flow and transport properties in brain micro-vascular networks. First, the CTRW framework links flow organization, including the flow organization in networks [81], to the associated transport properties [78]. Hence, it is an attractive framework to provide quantitative predictions of the transport of particles, e.g. nutrients or oxygen, within the micro-vasculature. Secondly, the q-model describes flow statistics in disordered porous media [82]. It thus provides a relevant framework to analyze in details the statistics of the random part of the blood flow organization induced by the structure of the capillary bed. Finally, the percolation theory has successfully demonstrated the relation between the modification of the topology of the medium, e.g. network connectivity, and its functional properties [80], e.g. network conductance. In that extent, the percolation theory is a relevant framework to study the impact of micro-vascular occlusions on cerebral blood flow. In the following, we introduce the basic elements of each of these three frameworks.

The Continuous Time Random Walk (CTRW) The CTRW is a stochastic process introduced in 1965 in its original lattice formulation to account for potentially largely distributed lag times between two successive hops of a particle [83]. This differs from classical Brownian motion for which hopping rate and hop length, defining the diffusion constant, are unique [84]. The CTRW formalism quantifies the impact of large distributions of lag times on the First Passage Time Distribution (FPTD), or BreakThrough Curve (BTC) in geophysicists vocabulary, or Survival Probability (SP) for instance [85–87]. Few years later, a hop length distribution has been further introduced giving rise to the modern CTRW formalism [88]. This formalism has been used for a wide range of applications like quantitative finance [89], spread of epidemics [90] or cell motion [91]. In particular, the CTRW framework has been successfully used in order to model anomalous transport in geological formations to account for the observed random heterogeneity of the velocity field that emerges from the disordered structure of geological porous media [92].

Formally the CTRW constitutive equation reads [88]:

$$R(s, t) = \sum_{s'} \int d\tau \Psi(s - s', t - \tau) R(s', \tau) \quad (1.2)$$

where $R(s, t)$ is the rate of arrival of particles at position s and time t and $\Psi(\Delta s, \Delta t)$ is the joint probability per unit of time density function to observe conjointly a spatial increment Δs and a time increment Δt . The CTRW process can be equivalently described in terms of a Generalized Master Equation [93] in order to include for example reactive processes [94].

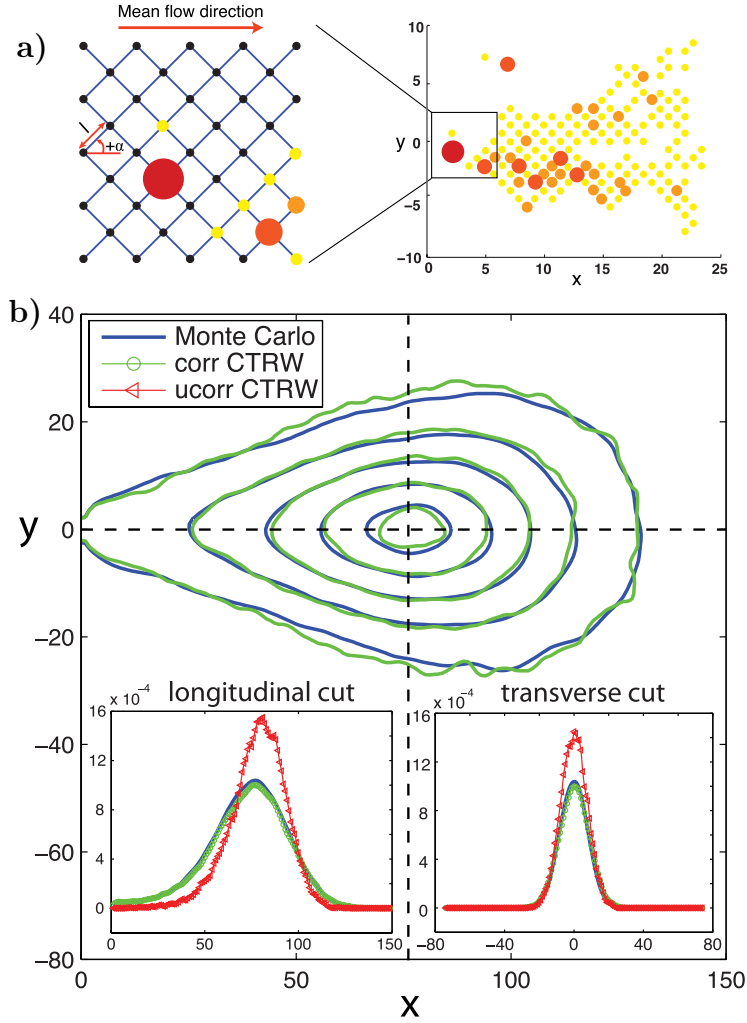


Figure 1.10: **The CTRW framework provides an accurate description of the anomalous transport dynamics in random lattices.** a) Spatial distribution of particles in a square lattice of random conductances (extracted from [81]). b) Contour plots (main panel) and longitudinal (left inset) and transverse (right inset) cuts of the average particle density at an arbitrary date during the transport obtained by direct Monte Carlo simulations, uncorrelated CTRW and correlated CTRW (extracted from [81]).

In flow-driven transport, the distribution of particle, or Lagrangian, time increments can be directly related to the Eulerian flow statistics in the medium through the following reasoning:

- Assuming ergodic transport, equidistant Lagrangian velocity statistics $p_s(v)$, can be expressed in terms of the Eulerian velocity distribution $p_e(v)$ through flux-weighting as [78]:

$$p_s(v) = \frac{vp_e(v)}{\langle v \rangle} \quad (1.3)$$

where $\langle v \rangle$ is the Eulerian average velocity.

- Hence, equidistant Lagrangian time increment distribution, $p_s(t)$, can be obtained by classical change of variable in probability density function, $p_s(t)dt = p_s(v)dv$, with $t = s/v$:

$$p_s(t) \sim \frac{p_s(v)}{v^2} \quad (1.4)$$

This iso-space formulation is particularly adapted in the context of modelling transport into random networks as we can assign to each edge of the network of unit topological length and its associated travel time (Fig. 1.10a). In more complex cases, this theoretical framework can account for potential correlations in the sampling of the time increments, or velocity, statistics [81, 95] (Fig. 1.10b) or the presence of a deterministic drift induced for example by non-local flow organization [96]. Based on the observation of the heterogeneities of transport dynamics in the brain micro-circulation, we intend to use the CTRW framework to provide a quantitative model linking the resulting dispersion of travel times to local flow properties.

The q-model The q-model is a statistical mechanics model originally developed to quantify the force fluctuations in random bead packs [97]. As it will be extensively studied in Chapter 3, we will provide here only the principal conceptual aspects of this model and its link with flow in porous media. In its mean field formulation, the q-model defines an analytically solvable framework based on only the two following requirements [79]:

- A local recursive equation based on the conservative weight propagation between successive bead layers: each bead transmits the totality of the weight it bears through random fractions destined to each bead on which it relies. Reciprocally, each bead bears the sum of the random contributions of the beads belonging to the above layer.
- The stability of the distribution of force fluctuations with depth.

The process of conservative propagation of forces in random bead packs is similar to the local description of flow organization in disordered porous media in which flow sums and divides randomly at pores (Fig. 1.11a). Hence, this model has been adapted to predict flow statistics in porous media of random conductances with success [82, 98]. Akin to random aggregation/fragmentation process [99–101], the emerging distribution of force fluctuations in random bead packs, and by analogy of flow in porous media, is found to decay exponentially at large values (Fig. 1.11b). This model emphasizes that pore size distribution is not the only driver of flow heterogeneities as assumed sometimes at the cost to consider local pressure drops constant accross the pore network [102]. In other words, there is a competition between flow heterogeneities controlled by the pore size distribution and flow heterogeneities controlled by flow disorder. The reconciliation of both visions into a unified theoretical framework is currently investigated within a collaboration that we have developed during my thesis with the team of Marco Dentz. In micro-vascular networks, the disordered structure and the homogeneity of the capillary bed motivates the use of

the q-model to study the heterogeneity of the flow statistics. In that extent, we intend to provide in this work a complete mapping of the flow organization in homogeneous random networks on the q-model.

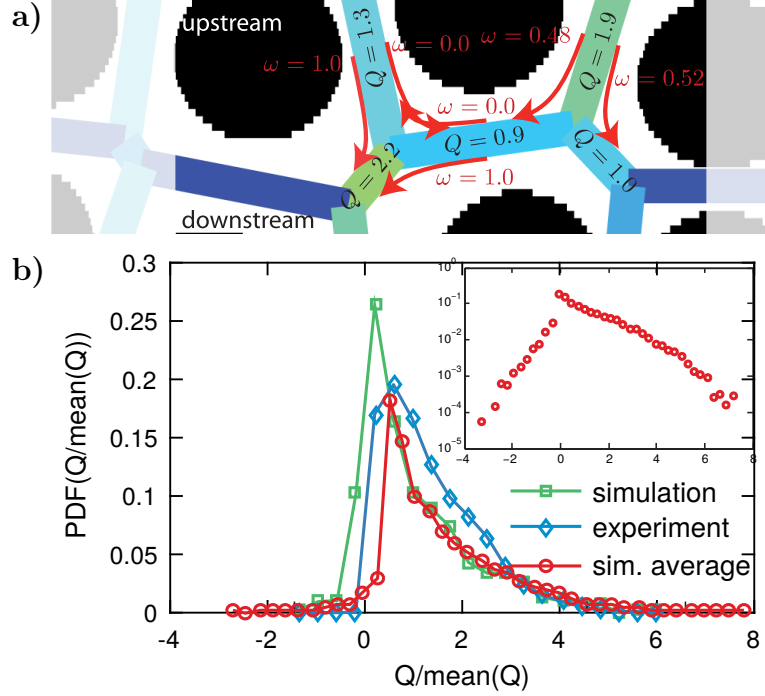


Figure 1.11: **Random additions and divisions of the flow at pores in disordered porous media induce an exponential distribution of the flow statistics at high values.** a) Snapshot of the local flow organization in a porous medium of random conductances (extracted from [82]). b) Flow distribution in disordered pore networks obtained by experiment (blue) and by simulations, with a single realization (green) and on average over several realizations (red). Main panel: linear scale. Inset: semi-log scale (extracted from [82]).

The percolation theory Percolation theory has been originally designed to model fluid flow through porous media and introduced in its original lattice formulation in 1957 [103]. Laying the foundations of the percolation theory, this work highlighted the crucial role of the pore network topology (e.g. dimension or graph connectivity) on flow properties. By the study of the impact of random removal of lattice links, this work demonstrated the existence of a critical fraction of remaining links below which the flow cannot establish: the percolation threshold. In 1971, an experiment emphasized the surprising behavior of conductance evolution with the removed fraction of bonds in a 2D square lattice in the shape of a two regime decay [104] (Fig. 1.12a). In the first regime, conductance decays linearly with the fraction of missing bonds before smoothening and finally reaching zero at the percolation threshold (Fig. 1.12b). The effective medium framework developed the same year [105] provided the first analytical answer to this linear decay. In particular, this framework linked with success the connectivity of 2D and 3D lattices to the slope of the linear regime [80]. In the latter study, the second regime is also shown to be a power law in the fraction of added bonds with a universal characteristic exponent. The emergence of such regime is associated to the growth of an “infinite”, or giant, component spanning the network. The study of the network topological properties, driving the flow properties, close to the percolation

threshold is tackled with approaches accounting for the emergence of the self-similar dynamics of cluster growth like Renormalization Group techniques [106]. With the emergence of real complex networks in our every day life, like transportation networks or the World Wide Web, the influence of distributed connectivity on the percolation process has been a trending topic along the years [107–110]. This resulted notably in the study of the impact of targeted attacks [111, 112] or optimal network dismantling [113, 114] on network robustness.

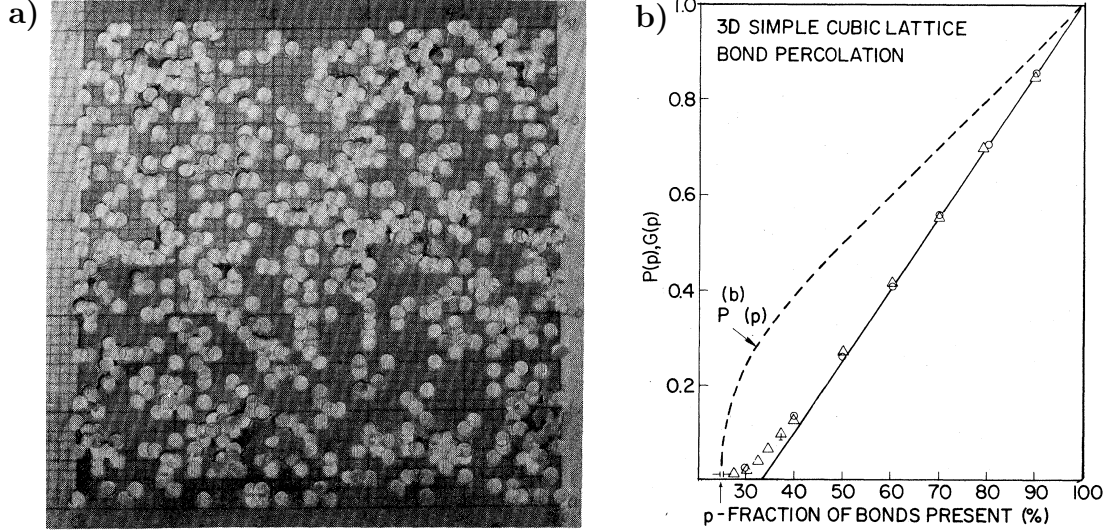


Figure 1.12: **Conductance decrease during the percolation process exhibits two regimes: a first linear decay at low values of removed bonds smoothening non-linearly in the vicinity of a critical value, the percolation threshold.** a) Historical experiment highlighting the two-regimes decay of the conductance: a conductive sheet perforated randomly. In this photo the fraction of removed bonds is 0.268 (extracted from [104]). b) Evolution of the conductance $G(p)$ (dashed line) and the percolation probability $P(p)$ (triangles and circles) as a function of the fraction of present bonds p in 3D cubic lattice obtained by direct simulations. Full line represents the prediction of the effective medium prediction (extracted from [80]).

In the context of this thesis, the topological structure of the micro-vasculature constrains the range of relevant results in the abundant literature about percolation. First, micro-vascular networks are not complex networks in the sense that they display a uniform 3-connectivity and then belong to the class of Random Regular Graphs (RRGs) [115]. Secondly, the dynamics close to the percolation threshold are not investigated because of their irrelevance in micro-vascular networks. On one hand, on a physical point of view, the establishment of the flow is not driven by the emergence of a giant component as micro-vascular inlets and outlets have a close topological proximity. This induces a trivially low percolation threshold. On the other hand, on a biological point of view, the fraction of occluded vessels rarely overcomes 20%. In this regime, cerebral blood flow decreases linearly in average [21] emphasizing that perturbative approaches should catch the impact of occlusions on blood flow. The question of flow perturbations far from the percolation threshold have been investigated previously notably in the context of the impact of failure in power grids [116]. In this context, the impact of changes in power grid topology is quantified through a term called the Line Outage Distribution Factor (LODF). More recently, this concept has been generalized to account for the type of processes developing in the network, e.g. oscillating interactions, flow propagation or disease spreading [117]. Hence, the generalization of this concept

allows to catch into a unified framework the response of the network to small perturbations independently of the type of interactions binding the nodes. In particular, this kind of approach has been used in the context of the study of the resilience of biological transport networks and in particular of the vasculature [118]. In agreement with the concepts developed in these last works, we focus in this thesis on the influence of punctual inlets and outlets, topological communities and vessel conductance variability in micro-vascular networks on cerebral blood flow modifications induced by micro-vascular occlusions.

1.4 Objectives and outline

Along this introductory chapter, we settled the scientific context of this thesis work. In the light of the presented literature, we have shown that numerous questions are still open. In particular, it is unclear how the peculiar structure of the brain micro-vascular networks [2, 7–9] influences or determines the flow organization and the emergence of the observed heterogeneous blood flow properties [22, 23, 43, 44]. Consequently, the lack of physical description of the blood flow organization within micro-vascular networks prevents from designing first principle micro-circulation transport models. This compromises the generality or the accuracy of former transport models [30–34, 38, 39, 44, 46]. Hence, the determination by such types of models of the role of the micro-circulation in the onset and/or the progression of neuro-degenerative diseases like Alzheimer’s is questionable although experiments attest that micro-circulation impairments do play an active role in such diseases [4, 11, 15–20]. In particular, these studies have highlighted cerebral blood flow decrease as a key process associated to cognitive decline. However, the mechanisms leading to such decrease and their consequences on brain metabolism are still poorly understood. Recently, micro-vascular occlusions have been shown to be a precursor of cognitive decline in Alzheimer’s mouse models [21]. These occlusions have been observed conjointly to a decrease of the cerebral blood flow in these rodents. Consequently, they could be a mechanism explaining such decrease and the triggering of the biological pathways leading to the onset of the disease. However, here again, this interpretation suffers a lack of quantification of the cerebral blood flow perturbations induced by micro-vascular occlusions.

As a consequence, the main objectives of this thesis can be summarized by the three following challenges:

1. Unraveling the interplay between the brain micro-vascular structure and the blood flow organization.
2. Modelling the transport properties emerging from this organization within a quantitative framework allowing to predict the evolution of concentrations of relevant chemical species with cerebral blood flow decrease.
3. Providing a theoretical framework explaining the perturbation of the cerebral blood flow induced by micro-vascular occlusions.

In order to report the outcomes of our investigations, this thesis manuscript is structured in three chapters:

- In Chapter 2, we present the results of a statistical analysis performed on highly-resolved blood flow simulations in anatomically accurate mouse brain micro-vascular networks. This analysis serves as a starting point for the modelling of transport properties in such networks

thanks to the Continuous Time Random Walk (CTRW) framework. We further present the results of the comparison of this model to the simulations of transport of passive and reactive particles.

- In Chapter 3, we focus on the interplay between the disordered structure of the capillary bed and the flow organization in the light of the q-model. In that extent, we firstly present the details of this model and their link with flow in disordered porous media. We then perform a statistical analysis of potential local flow correlations explaining the observed deviation of observations to mean-field predictions.
- In Chapter 4, we investigate the linear decrease of the cerebral blood flow due to micro-vascular occlusions within the percolation framework. Doing so, we lay the foundation of a theoretical approach accounting for the community structure and blood flow organization in micro-vascular networks. We further investigate the impact of multiple inlets and outlets and conductance heterogeneties on flow resilience. Finally, we highlight the large perturbations of blood flow organization induced by such occlusions.

Chapter 2

Blood flow organization and effective transport models

Describing and understanding the emergence of blood flow organization in brain micro-vascular networks is a key step in the design of predictive micro-circulation transport models. Such macroscopic models are central to a large range of applications, from clinical studies aimed at improving the diagnosis and/or staging of brain disease [38, 39] to fundamental studies on cerebral blood flow and metabolism or neuro-vascular coupling [11]. In particular, they could open new avenues to predict the decrease of the efficiency of oxygen or nutrients supply and the removal of metabolic wastes induced by blood flow impairments. In the context of Alzheimer’s disease, a decrease of the cerebral blood flow, or hypoperfusion, associated to a decrease of the metabolic activity [11, 15, 16, 21] and to an accumulation of metabolic wastes, e.g. amyloid [119], have been identified as markers of the disease.

In this chapter, our objective is to address the question of the transport mechanisms leading to the appearance and/or growth of regions with abnormal concentrations of oxygen or amyloid. To do so, based on a statistical analysis of highly-resolved blood flow simulations on anatomically accurate mouse brain micro-vascular networks, we first highlight the determinant role of micro-vascular structure in the emergence of blood flow organization. Such organization is found to induce anomalous transport properties in the micro-circulation. This results in a broad distribution of time spent by blood in the micro-circulation. We notably show that these transit time heterogeneities are the main driver of concentration heterogeneities in micro-vascular networks as intuited in [46]. Besides, in this thesis, we derive for the first time a transport model accounting for these large heterogeneities supported by physical mechanisms linking the micro-vascular structure and the flow organization. In agreement with our simulations, we notably highlight the role of such transit time heterogeneities in the early development of regions exceeding critical oxygen and amyloid concentrations under conditions of hypoperfusion. This could be an additional mechanism leading to a positive feedback responsible for the progression of Alzheimer’s disease.

2.1 Blood flow and transport statistics modelling

This section reproduces a manuscript under review in Nature Communications. In a first part, we focus on the interplay between micro-vascular structure and blood flow organization. Then, we show that this organization induces anomalous transport properties leading to a large dispersion of travel times within the brain micro-vasculature by the design of a novel micro-circulatory model

belonging to the class of Continuous Time Random Walks (CTRWs). Finally, we show that these properties are responsible for the early development of regions with abnormal concentrations of oxygen and amyloid with hypoperfusion. Hence, we unveil a new potential mechanism leading to the progression of Alzheimer's disease.

Network-driven anomalous transport is a fundamental component of brain microvascular dysfunction

Florian Goirand^{1,2}, Tanguy Le Borgne^{*2} and Sylvie Lorthois^{*1}

¹*Institut de Mecanique des Fluides de Toulouse, UMR 5502, CNRS, University of Toulouse, France*

²*University of Rennes, CNRS, UMR 6118, 35000 Rennes, France*

Abstract

Blood microcirculation supplies neurons with oxygen and nutrients, and contributes to clearing their neurotoxic waste, including amyloid- β , a metabolic waste product centrally involved in Alzheimer's Disease. The microvascular architecture combines tree-like arteriolar and venular structures with a dense capillary network, yielding highly heterogeneous blood flow and travel time distributions. Such heterogeneities likely control the appearance of critical regions, whether hypoxic or with abnormally high amyloid- β concentration, a signature of microvascular dysfunction. The quantification of such intravascular travel time distributions plays a central role for understanding, modeling and imaging the microvascular contributions to brain disease onset and progression. Yet current models, broadly used for interpreting in vivo measurements, rely on empirical functions whose link with the microvascular architecture is unknown. Here we use highly-resolved intracortical blood flow and transport simulations, validated from in vivo measurements, to establish the physical laws linking the microvascular architecture to the macroscopic transport properties that control oxygen supply and amyloid- β clearance. We show that the microvascular organization leads to the emergence of anomalous transport dynamics and hence to the occurrence of unexpectedly large blood travel times through the cortex. We develop a Continuous Time Random Walk theory capturing these dynamics and predicting that critical regions appear much earlier than anticipated by current models under mild hypoperfusion. These findings hence provide a new framework for measuring and modelling microvascular dysfunction in brain pathophysiology, as shown here in the context of Alzheimer's disease.

The brain microvascular network provides an efficient, highly integrated and dynamic infrastructure for the distribution of blood [1, 2, 3]: it supplies oxygen, nutrients and, if needed, drugs to all cells in the brain, and ensures

the removal of their metabolic waste [4, 5]. Since the brain lacks any substantial energy reserve, it also acts as a short-term regulation system, which responds quickly and locally to the metabolic needs of neurons [2, 6]. In ageing and disease, however, the progressive appearance of abnormal vessel architectures, includ-

* Corresponding authors: tanguy.le-borgne@univ-rennes1.fr and lorthois@imft.fr

ing reduced capillary diameters or stalling, and the decrease in regulation efficiency together reduce blood flow and the availability of oxygen [2, 7, 5, 8, 9, 10, 11]. This also alters the clearance of metabolic waste, including neurotoxic forms of amyloid- β centrally involved in the pathogenesis of Alzheimer’s Disease (AD) [4, 9, 10]. Thus, understanding the links between the microvascular architecture, reduced blood flow and impaired oxygen delivery and metabolic waste clearance is a key challenge to decipher the role of microvascular dysfunction in brain disease.

The microvascular architecture is structured by tree-like arterioles and venules that connect to a dense capillary network [12, 13, 3]. While this organization ensures a large surface of exchange between blood and the brain tissue, it also induces strong spatial heterogeneities of vessel flows and capillary transit times, leading to heterogeneous oxygenations [14, 15]. Even in normal conditions, some vessels with low blood flow rates approach the hypoxic threshold [16, 17]. These critical vessels may be particularly vulnerable to further pathological stress [17], consistent with the appearance of small hypoxic regions in the cortex of ageing and AD mice [18, 9]. Since reduced capillary flow also compromises metabolic waste clearance, critical vessels with abnormally high intravascular concentrations of amyloid- β may also be expected. Yet, it is unknown how such critical vessels may appear under normal conditions nor how they may progress in response to pathological stress, such as hypoperfusion [19, 10, 20].

In fact, the dynamics governing oxygen or amyloid- β distributions in such networks are fundamentally non-local: the solute concentration in a given vessel depends on the blood travel time from penetrating arterioles, where blood enters into the brain cortex, to this vessel, which integrates all blood velocities along the corresponding pathways. Furthermore, the distribution of blood flow is also non-local, i.e. driven by the whole vascular architecture. Because the impact of such non-local dynamics on relevant network-scale processes is difficult to resolve explicitly, the blood travel time distri-

bution through the microvascular network¹ has been represented by phenomenological models [23], including early indicator dilution analysis models [24, 25, 23, 21] and the recent Capillary Transit Time Heterogeneity (CTH) model [14]. These models rely on empirical blood travel time distributions, following mathematical functions chosen to match the experimentally observed distributions [26]. A key property emerging from CTH models is that increased transit time heterogeneities induce a decreased efficiency of oxygen supply [14]. Consistently, reduced transit time heterogeneity has been experimentally confirmed in the cortical layers with the highest levels of metabolic activity [27] or in response to neuronal activation [28] while increased transit time heterogeneity has been inferred, based on such models, from clinical imaging data in AD patients [29]. Besides these few examples, CTH models have been used to interpret a large amount of experimental data [30, 31, 32, 18, 15] thus helping to identify increased vascular heterogeneity as a key general mechanism of neuronal injury. A fundamental limitation of current phenomenological models is that they do not quantitatively relate the transport dynamics to the underlying network architecture and flow distributions. This makes it difficult to understand and predict how changes in vessel architecture may influence blood travel time heterogeneity and thus alter oxygen supply and metabolic waste clearance. Furthermore, in vivo measurements are limited to time scales smaller than the blood recirculation time (~ 5 s) [33], which limits the range available for the calibration of empirical models. Hence, their predictive power for the statistics of longer time scales, which likely control the appearance of vessels with critical oxygen or amyloid- β concentrations, is strongly dependent on the mathemati-

¹Blood transit times through microvascular networks have also been referred to as *traversal times* [21] or, simply, as *transit times*. To avoid any ambiguity with local transit times, i.e. the time for blood to flow through one single vessel, we use here the term *travel times*. The distribution of travel times is sometimes referred to as the impulse response function, as the *transfer function* of the system or as the *microvascular response function* [22].

cal functions chosen to parametrize travel time distributions [25, 24]. Yet, the physical mechanisms shaping these distributions and how they depend on the network structure [23] are poorly understood.

Theoretical analyses of transport in model random networks have shown that these systems can exhibit anomalous transport dynamics, i.e. characterized by slow power law decays of the large travel time probabilities [34]. The latter have been successfully described by Continuous Time Random Walk (CTRW) theories, providing analytical expressions of travel time distributions as a function of the microscale structures and flow distributions [35, 34, 36, 37]. Although microvascular networks fundamentally differ from such random networks, their complex structure potentially contains the fundamental ingredients for anomalous transport dynamics to develop. To explore this hypothesis, we use highly-resolved simulations of blood flow in such networks, validated from in vivo measurements, that provide access to the full statistics of blood flow and transport dynamics in realistic microvascular networks. We use these insights to uncover the scaling laws of blood flow distributions arising from the microvascular architecture and develop an effective transport model at the scale of the network that captures these properties. This provides analytical solutions for the blood travel time distributions inferred from the physics of transport in these networks. Our model predicts that the interplay between the spatial distribution of arterioles and venules and the mesh-like architecture of the capillary bed [12] leads to the emergence of anomalous transport dynamics. This implies that the occurrence probability of large blood travel times is significantly larger than predicted by current models. We couple this model to the kinetics of oxygen consumption and amyloid- β production in brain cells to show that these anomalous transport properties control the early development of critical vessels with low oxygen or large amyloid- β concentrations under hypoperfusion. These findings hence provide a new framework to measure, understand and model the onset and development of brain diseases, such as AD [38].

Results

Vessel flow rates and transport times follow broad distributions. Our analysis is based on highly-resolved simulations of blood flow in anatomic micro-vascular networks, validated by comparison with in vivo measurements (see Methods and SI Appendix A). We first present results obtained in a microvessel network ($\sim 15,000$ vessels) digitized from a 1mm^3 of the mouse cortex (see Fig. S1) and then compare the results to a different mouse microvessel network and to bio-mimetic networks (SI Appendix C and H). The dense capillary bed in the first network is homogeneous and space-filling [17, 39], with a narrow distribution of vessel diameters ($4.8 \pm 0.9 \mu\text{m}$). The network is fed and drained by ~ 15 arteriolar and ~ 30 venular trees (Fig. 1a, Fig. S1 and Supplementary Movie S1). Simulations integrate the non-linear blood rheology and red blood cell repartition at diverging vessel bifurcations (see Methods). The average flow rate is $\langle Q \rangle_0 = 4.10^{-2} \text{ nL/s}$. The probability density function (PDF) of blood flow in vessels shows a large spread across about seven decades around the average flow rate (Fig. 1b). This PDF exhibits two different regimes: it is uniform in the low flow range and decays as a power law with exponent -2 above a characteristic value $Q_c = 10^{-2} \text{ nL/s}$. The number of vessels in these regimes is approximately $P(Q < Q_c) = 60\%$ and $P(Q > Q_c) = 40\%$, with large flow rates developing preferentially in the neighborhood of arterioles and vessels (Fig. 1a and S1f, Supplementary Movie S2). The flow PDF is well approximated by a Cauchy distribution (Fig. 1b), consistent with the theoretical asymptotic behavior obtained in large Random Regular Graphs [40]

$$p_Q(Q) = \frac{2}{\pi Q_c} \frac{1}{1 + (Q/Q_c)^2}, \quad (1)$$

A direct consequence of the broad distribution of flow rates Q is the broad distribution of advective transit times in vessels (inset of Fig. 1b), which are defined as:

$$t = \frac{l\pi d^2}{4Q}, \quad (2)$$

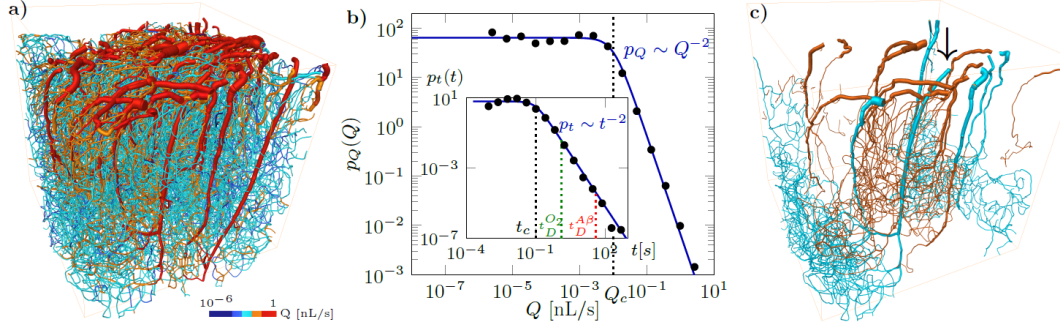


Figure 1: The blood flow organization in cortical microvessel networks induces broadly distributed flows and vessel transit times. **a)** Simulated blood flow map in a microvascular network feeding 1mm^3 of the mouse cortex (see Fig. S1a,b and Supplementary Movie S1). Vessel flow rates are represented with blue shades for $Q < Q_c$ and red shades for $Q > Q_c$ (see also Fig. S1c,d,f and Supplementary Movie S2). **b)** PDF of simulated flow rates (black dots) compared with the approximation of Eq. 1 (continuous blue line). The characteristic flow rate Q_c separating the uniform and power-law regimes is indicated as a dotted line. Inset: PDF of vessel transit times. The diffusion coefficients for oxygen and amyloid- β ($D_{O_2} = 2.10^{-9} \text{ m}^2.\text{s}^{-1}$ and $D_{A\beta} = 6.10^{-11} \text{ m}^2.\text{s}^{-1}$) yield diffusion times ($t_D^{O_2}$ and $t_D^{A\beta}$) indicated by the green and dashed lines, respectively. **c)** Example of trajectories visiting less than 30 vessels (orange) and more than 60 vessels (blue), originating from the arteriole shown by the arrow (see Fig. S2a-d and Supplementary Movies S3).

where l is the vessel length and d the vessel diameter. As the flow PDF, the vessel transit time PDF is characterized by two regimes separated by the characteristic time $t_c = \frac{\langle l \rangle_{cap} \pi \langle d \rangle_{cap}^2}{4Q_c} = 10^{-1} \text{ s}$, where $\langle l \rangle_{cap} = 50 \mu\text{m}$ and $\langle d \rangle_{cap} = 5 \mu\text{m}$ are taken as characteristic capillary length and diameter, respectively. Since the vessel length l and diameter d vary weakly compared to the flow rate Q , the transit time variability is mainly driven by the flow rate fluctuations. We thus estimate the PDF of vessel transit times from the PDF of flow rates as $p_t(t) = p_Q(Q) dQ/dt$, also yielding a Cauchy distribution

$$p_t(t) = \frac{2}{\pi t_c} \frac{1}{1 + (t/t_c)^2}, \quad (3)$$

in good agreement with the simulations (inset of Fig. 1b). The scaling $p_t(t) \sim t^{-2}$ for long times, $t > t_c$, is induced by the uniform flow PDF $p_Q(Q) \sim \text{cst}$ at low flow rates, $Q < Q_c$, leading to $p_t(t) \sim dQ/dt \sim t^{-2}$ (Eq. (2)). This scaling yields a non-negligible probability of extremely long vessel transit times, which may lead to the emergence of anomalous transport

properties at the network scale [34, 35].

This vessel transit time PDF $p_t(t)$ characterizes the vessel transport statistics in the absence of diffusion. Diffusion introduces a maximum cut-off time $t_D = \langle l \rangle^2 / D$ in the transit time PDF, corresponding to the diffusive transport time over a vessel length. For oxygen and amyloid- β , the two species considered here, the range of times $t_c < t < t_D$ over which the power law $p_t(t) \sim t^{-2}$ holds thus covers respectively one and three orders of magnitude (Fig. 1b, inset). Therefore, this power law regime affects significantly more amyloid- β clearance than oxygen supply.

Network trajectory lengths and travel times show anomalous transport statistics. In addition to the broad distribution of vessel transit times, solute transport at the scale of the microvascular network is also controlled by the distribution of trajectory lengths from arterioles to venules. Our particle tracking simulations (see Methods, Fig. 1c and 2a and Supplementary Movie S4) show that trajectories lengths L , expressed in number of visited vessels, vary from less than 10 to about 80

(Fig. 2b). The trajectory length PDF is characterized by a power law scaling $p_L(L) \sim L^{-2}$ between two characteristic lengths $L_0 = 12$ and $L_c = 50$. Above L_c , the PDF decays sharply as $p_L(L) \sim \exp(-L/L^*)$ with $L^* = 5$ (Fig. 2b):

$$\begin{cases} p_L(L) \sim L^{-2} & L_0 < L \leq L_c \\ p_L(L) \sim \exp(-L/L^*) & L > L_c \end{cases} \quad (4)$$

Averaging over multiple trajectories of equal length, we computed the evolution of the local average transit time along the trajectory, as a function of the number n of vessels visited since the inlet arteriole (Fig. 2b, inset). These average local transit times are of the order of 10^{-2} s close to the inlet arterioles, then increase, up to two orders of magnitudes for the longest trajectories, then decreases again in the vicinity of the outlet venules. The network travel time $\bar{\tau}^L$ thus increases with the trajectory length L following two different trends (Inset of Fig. 2c, SI Appendix D and Fig. S4a-b),

$$\begin{cases} \bar{\tau}^L(L) \approx \tau_1(L - L_0) + \mathcal{T}_0 & L_0 < L \leq L_c \\ \bar{\tau}^L(L) \approx \mathcal{T}_c \left(\frac{L}{L_c}\right)^4 & L > L_c \end{cases} \quad (5)$$

where $\mathcal{T}_0 = 0.2$ s, $\mathcal{T}_c = 1.8$ s, and $\tau_1 = 0.04$ s is on the order of the mean transit time over particle trajectories.

The broad distribution of vessel transit times, together with the distribution of trajectory lengths, leads to a broad range of travel times at the network scale $p_{\mathcal{T}}(\mathcal{T})$ (Fig. 2c). Without diffusion, simulated travel times vary over four orders of magnitudes. Accounting for the diffusive cut-off transit time (inset of Fig. 1b), the travel time distribution still covers over two orders of magnitude for oxygen and three orders of magnitude for amyloid- β (Fig. 2c).

Flow and transport properties emerge from the physics of dipole flows in networks. The statistical properties driving these transport dynamics can be understood as arising from different topological properties of the flow field, as schematized in Fig. 3. The measured scaling $p_Q(Q) \sim Q^{-2}$ is a characteristic of dipole flows [41] (see SI Appendix C, Fig. S3d).

In the present system, high flow rates are localized around arterioles and venules that act as multiple sources and sinks (Fig. 1a and S1, Supplementary Movie S1), driving the flow in the network. Hence, in the large flow range, $Q > Q_c$, the flow field behaves statistically as a superposition of dipoles. At low flow rates, $Q < Q_c$, the flow statistics differ from the continuous dipole model and become uniform, a signature of the network structure (see SI Appendix C, Fig. S3d). In random networks, the flow PDF is indeed theoretically expected to follow exponential distributions, driven by the random additions and divisions of flow at vertices [42]. In the low flow range, this asymptotically leads to a uniform distribution of flows. Here, the low-flow vessels are far from arterioles and venules. Therefore, their statistics are dominated by the random fluctuations induced by the network structure. Noteworthy, similar flow PDFs are observed for dipole flows on space-filling networks with architectures of increasing complexity, see Fig. S3b-d. Thus, the observed flow statistics are generic and arise from the interplay between a structured dipole-like topology for large flows and a random network topology for small flows.

The distribution of trajectory lengths (Fig. 2b), is also consistent with this dipole flow interpretation (see SI Appendix C, Fig. S3e). For dipole flows on a finite size network, the power law regime $p_L(L) \sim L^{-2}$ develops until a cut-off length, corresponding to the network size, which sets the maximum trajectory length. In the present system, the characteristic trajectory length L_c that sets the transition to the exponential cut-off (Eq. (4)) is the maximum length of trajectories that can travel directly from one arteriole to a neighboring venule [43] (Fig. 1c and S2a,b, Supplementary Movie S3 (orange trajectories)). These trajectories typically reach the bottom of the simulated domain and include on average 20 arteriolar steps, 20 venular steps and 10 capillary steps in between (see Fig. 3 and SI Appendix B, Fig. S2f). Longer trajectories connect more distant arterioles and venules via the deep capillary bed, where most vessels are in the low flow regime ($Q < Q_c$) (Fig. 1c, 3 and S2c,d, Supplementary

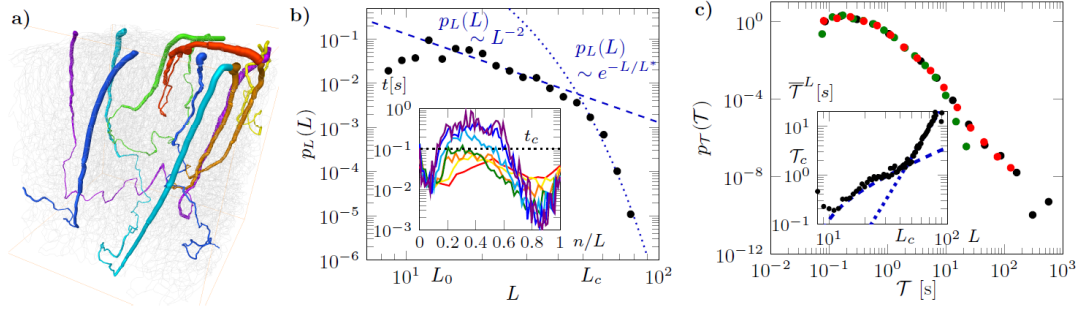


Figure 2: Trajectory lengths and travel times are broadly distributed at network scale. **a)** 3D view of typical particle trajectories (see also Supplementary Movie S4) with growing numbers of visited vessels (Red: $L = 20$; Yellow: $L = 30$; Orange: $L = 40$; Green: $L = 50$; Cyan: $L = 60$; Blue: $L = 70$; Violet: $L = 80$). **b)** Probability Density Function (PDF) of trajectory lengths. Inset: Local vessel transit times t averaged over all trajectories of same length L as a function of the number n of vessels visited since the inlet arteriole, normalized by L . Results for different trajectory lengths are shown with the same color conventions as in panel a). **c)** PDF of travel times through the network for purely advective (black dots), oxygen (green dots) and amyloid- β (red dots) transport. Inset: Average travel time \bar{T}^L as a function of trajectory length L (see also SI Appendix D and Fig. S4a-b). The linear and power law tendencies (Eq. (5)) are shown respectively as dashed and dotted blue lines. Note that the linear tendency does not appear as a straight line in log log because of the constant T_0 in Eq. (5) (See SI AppendixD).

Movie S3 (blue trajectories)).

The relationship between average travel times and trajectory lengths $\bar{T}^L(L)$ (Eq. (5)) shows a transition from a linear to a power law scaling (Inset of Fig. 2c and Fig. S4a,b). In the first linear regime, the number of visited capillaries remains approximately constant when the trajectory length increases (see SI Appendix B and Fig. S2f). This implies that the additional visited vessels belong to arterioles and venules. The linear scaling of $\bar{T}^L(L)$ indicates that the average transit time t in such vessels remains approximately constant when trajectories explore deeper sections of the network. As arterioles penetrate at depth, their flow rate decreases but so does their diameter and length, which may explain this finding. This may constitute an evolutionary advantage contributing to spatially uniformize the supply and clearance of solutes across the network while minimizing total dissipation and blood volume [44, 45, 46]. In the second regime, the power law scaling $\bar{T}^L(L) \sim L^4$ is characteristic of dipole flow in 3D systems (see SI Appendix C): in the deep network, blood flows from the pre-

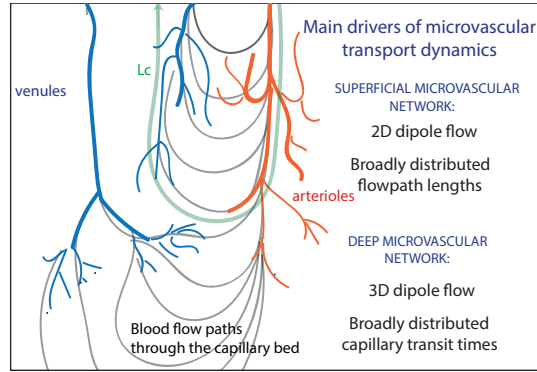


Figure 3: Schematic illustration of the blood flow organization in the cortical microcirculation inferred from the observed flow and transport properties. Arterioles and venules are represented in red and blue respectively. Blood flow paths through the capillary bed are represented as black lines. The characteristic trajectory length L_c is the maximum length of trajectories that can travel directly from one arteriole to a neighboring venule (green line).

capillary arterioles to the post-capillary venules through a complex 3D network of capillaries (Fig. 1c, 3 and S2c,d and Supplementary Movie S3 (blue trajectories)) where the number of visited capillaries increases steeply with the trajectory length (Fig. S2f).

Mean field transport dynamics are governed by dipolar trajectory length distributions. The distribution of trajectory lengths (Eq. (4)), coupled with the relationship between average travel time and trajectory length (Eq. (5)), provides a mean field transport model for the travel time PDF across the network (SI Appendix D). This mean field description, which neglects random fluctuations due to the network structure but captures the dipole-driven trajectory length distribution, is characterized by a transition from a power law to a stretched exponential behavior:

$$\begin{aligned}
 p_{\bar{\tau}}(\bar{\tau}) &\sim ((\bar{\tau} - \tau_0)/\tau_1 + L_0)^{-2} \\
 &\quad \text{for } \bar{\tau} < \tau_c \\
 p_{\bar{\tau}}(\bar{\tau}) &\sim \left(\frac{\bar{\tau}}{\tau_c}\right)^{-3/4} \exp\left(-\frac{L_c}{L^*} \left(\frac{\bar{\tau}}{\tau_c}\right)^{1/4}\right) \\
 &\quad \text{for } \bar{\tau} > \tau_c
 \end{aligned} \tag{6}$$

with $\tau_c = 1.8$ s (Eq. (5)). This model captures the travel time distribution over the first two orders of magnitude (Fig. 4a and SI Appendix D, Fig. S4c). We compare this prediction to that of a reference CTH model, that assumes a Gamma distribution of travel times, whose parameters are calibrated from in vivo data [14] (see SI Appendix G). Since experimentally measured travel time distributions are limited to times smaller than ~ 5 s due to blood recirculation [28, 33], this CTH model serves here as a reference to assess the effect of neglecting the experimentally inaccessible longest travel times. While it captures relatively well the shape of the travel time distribution in the low range, the reference CTH model significantly underestimates the probability of late times (Fig. 4a). Accounting for the trajectory length distribution via the mean field model allows capturing a significant part of this long

time dynamics. The mean field model, however, does not capture the power law behavior of the longest travel times, driven by vessels with transit times $t > t_c$ in the deep capillary network (Fig. 1c). Since the oxygen cut-off diffusion time $t_D^{O_2}$ is close to t_c (inset of Fig. 1b), this long time regime does not affect much oxygen transport, which is well represented by the mean field model (Fig. 4a).

Random flow fluctuations in the capillary network control large blood travel times. To obtain a full description of the transport dynamics, in particular for low diffusivity solutes such as amyloid- β , we seek an effective transport model that captures the heterogeneity of vessel transit times around the average behavior described above. Fluid elements transported along a given trajectory in the network move from one vessel to the next with a broadly varying time step (see SI Appendix E and F and Fig. S5a)). This closely corresponds to the conceptual framework of Continuous Time Random Walk (CTRW) [35, 37], which has been proved relevant as an effective representation of transport in random networks [34, 36]. However, as a consequence of the dipole structure of the flow at large scale, two characteristics of the transport dynamics differ from a conventional CTRW representation. First, the number of steps in a given trajectory is broadly distributed according to trajectory lengths (Eq. (4)). Secondly, the mean local transit time at the n^{th} step within a trajectory of length L depends on the trajectory length (Eq. (5), inset of Fig. 2b and SI Appendix D). Fluctuations of local transit times around these mean local transit times define a noise term that is independent on trajectory lengths and follows a power law scaling controlled by the flow distribution (see SI Appendix E). We therefore developed a CTRW framework capturing these two properties (see SI Appendix F).

This framework allows deriving an analytical solution for the travel time distribution $p_{\mathcal{T}}(\mathcal{T})$ in the network,

$$p_{\mathcal{T}}(\mathcal{T}) = p_{\mathcal{T}}^1(\mathcal{T}) + p_{\mathcal{T}}^2(\mathcal{T}), \tag{7}$$

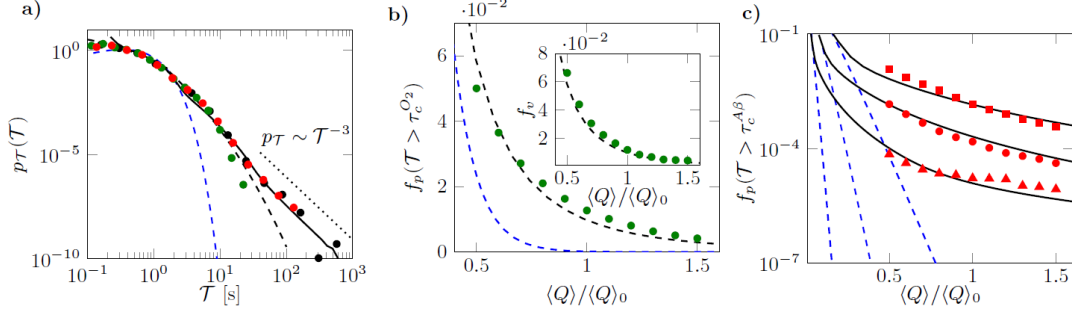


Figure 4: Long travel times, captured by our mechanistic model, drive the emergence of critical areas with impaired oxygen delivery and amyloid- β clearance under hypoperfusion.

a) CTRW model predictions (full black line) compared to purely advective, amyloid- β and oxygen transport simulations (black, red and green dots, respectively). The prediction of the mean-field transport model (Eq. 6) and of the reference CTH model (SI Appendix G) are shown as dashed black and blue lines, respectively. b) Fraction f_p of network travel times larger than $\tau_c^{O_2}$ for oxygen delivery as a function of average flow rate $\langle Q \rangle / \langle Q \rangle_0$. Simulations (green dots) are compared to the predictions of the mean field model (dashed black line) and of the reference CTH model (dashed blue line). The inset shows the fraction f_v of vessels in the network that are only reached by flow paths with travel times to these vessels larger than $\tau_c^{O_2}$, as a function of the flow rate. c) Fraction f_p of network travel times larger than $\tau_c^{A\beta} = 8$ s (squares), $\tau_c^{A\beta} = 16$ s (dots) and $\tau_c^{A\beta} = 40$ s (triangles), as a function of average flow rate for amyloid- β clearance. The predictions of the CTRW model (Eq. (7)) for each value of $\tau_c^{A\beta}$ are shown as continuous black lines. The predictions of the reference CTH model (see SI Appendix G) for each value of $\tau_c^{A\beta}$ are shown as a blue dashed lines.

where $p_T^1(\tau)$ and $p_T^2(\tau)$ are defined in Laplace space as,

$$\tilde{p}_T^1(s) = e^{-s\tau_0} \sum_{L=L_0+1}^{L_c} p_L(L) (\mathcal{P}(s\tau_1))^{L-L_0} \quad (8)$$

and

$$\tilde{p}_T^2(s) = e^{-s\tau_0} \mathcal{P}^{L_c-L_0}(s\tau_1) \sum_{L=L_c+1}^{\infty} p_L(L) \mathcal{P}^{L-L_c} \left(s \frac{\tau_c(L/L_c)^4 - \tau_c}{L - L_c} \right) \quad (9)$$

where s is the Laplace variable, $\mathcal{P}(s) = 2sK_2(2\sqrt{s})$ with K_2 the Bessel function of the second kind and $p_L(L)$ is given by Eq. (4).

This CTRW model is fully determined from the trajectory length PDF (Eq. (4)) and the relationship between average time and trajectory length (Eq. (5)). It provides an accurate prediction over a broad range of travel times with no fitting parameter (Fig. 4a). In particular, it captures the late time power law decay:

$$p_T(\tau) \sim \tau^{-3}. \quad (10)$$

The emergence of this power law is consistent with the CTRW theory that predicts stable power law distributions for noises characterized by power law exponents equal or smaller than 3 (see Fig. S5) [35, 37]. Hence, the late time transport behavior is characterized here by stable anomalous transport, driven by the broad distribution of flow rates in the network. As far as we know, no experimental data have been obtained to confirm this result in the brain microcirculation. However, injections of flow-limited tracers in the coronary network of isolated rabbit hearts, which avoids blood recirculation, yielded a power-law decay of the late time regime with exponent -3.21 ± 0.27 [47]. This suggests that, despite the variability of microvascular architecture among organs [48, 49], the combination of tree-like structures with a dense capillary network in their global organization is sufficient to drive this late time power law decay.

Simulation of three-dimensional oxygen distribution in microvascular networks.

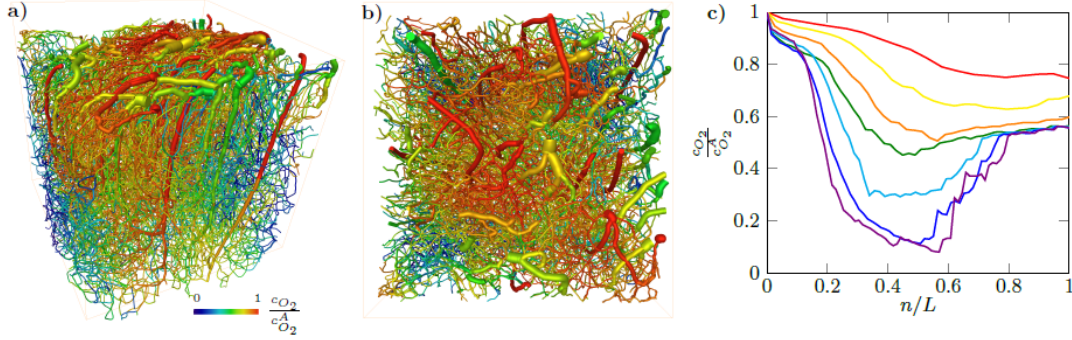


Figure 5: Simulated distribution of blood oxygen concentration relative to oxygen arteriolar concentration in the microvascular network represented in Fig. 1. See also Supplementary Movie S5. a) Side view. b) Top view. c) Evolution of the mean vessel oxygen concentration along trajectories of size L , concentrations are normalized by the arteriolar concentration $c_{O_2}^A$. Red: $L = 20$; Yellow: $L = 30$; Orange: $L = 40$; Green: $L = 50$; Cyan: $L = 60$; Blue: $L = 70$; Violet: $L = 80$.

Assuming that oxygen consumption in vessels follows first order kinetics [26] (see Methods and SI Appendix I), we use our particle tracking simulations to compute three-dimensional fields of oxygen concentration in vessels (Fig. 5a,b and Supplementary Movie S5). The characteristic reaction time of the first order kinetics $\tau_r^{O_2} = 1.5$ s is estimated by matching the simulated ratio between oxygen concentrations at venular outlets and those at arteriolar inlets to typical measured values (see Methods). The evolution of the oxygen concentration along trajectories, averaged over trajectories of equal length (Fig. 5c), is in qualitative agreement with previous experimental observations [17]. Oxygen decays close to the network inlets, as trajectories penetrate down in the cortex, then reaches a minimum in the capillary bed (except for the shortest trajectories $L = 20$), and increases again as blood flows up to the venular outlets (Fig. 5c). The minimum oxygen value along trajectories decreases with the trajectory length L , as longer trajectories penetrate deeper in the network. This directly results from the increase of blood travel time with increasing trajectory length (Eq. (5) and inset of Fig. 2c). The minimal oxygen concentration in the network, reached in the deep capillaries of the longest trajectories, is close to 1/12 of the inlet concentration, i.e. 10 mm Hg of oxygen partial pressure, assuming 120 mm Hg

at the inlets. This value is typically used to identify hypoxic brain regions in animal experiments [50, 51]. Hence, our results are consistent with the recent experimental observation that some vessels approach the hypoxic threshold in the cortex of normal mice [17]. The increase of oxygen towards the outlet venules is also consistent with in vivo observations showing an increase of oxygen concentrations with increasing venous diameters [17]. While its origins are debated [17], the two minimal ingredients included in our simulations, i.e. first order decay of oxygen with travel time and mixing at vessel intersections, are sufficient to capture this behavior. Hence, the travel time and trajectory length statistics explored here are key to explain the oxygen dynamics.

Anomalous transport drives the early appearance of hypoxic regions under conditions of hypoperfusion. Hypoperfusion, i.e. the decrease of the average blood flow, is a major pathological stress associated to many diseases [19], including early stages of AD [38, 20]. Schematically, it may be due to reduced perfusion pressure or increased cerebrovascular resistance, e.g. induced by capillary occlusions [8] or reduced vessel diameters [9] in AD. In the latter case, the total resistance of the capillary bed has been estimated to increase more than three-fold, leading to a $\sim 50\%$ blood flow reduction. This large hypoperfusion level significantly in-

creases tissue hypoxia [9] and is believed to favor amyloid- β accumulation in the brain [10], thus participating in disease progression. However, whether lower levels of hypoperfusion (5 to 30%), such as induced by capillary occlusions [8], may be involved in disease onset is debated [10]. In this context, we use our modeling framework to quantify the appearance of hypoxic regions, focusing on the occurrence probability of trajectories with travel times above the critical travel time $f_p(\mathcal{T} > \tau_c^{O_2})$, which corresponds to the hypoxic threshold. Using the first order kinetic model (SI Appendix I, equation S28), we estimate this critical travel time to be $\tau_c^{O_2} = \log(12)\tau_r^{O_2} = 3.7$ s. The probability of exceeding $\tau_c^{O_2}$ along a given flow pathway is derived from our transport model as $f_p(\mathcal{T} > \tau_c) = \int_{\tau_c}^{\infty} d\mathcal{T} p_{\mathcal{T}}^{(Q)}(\mathcal{T})$, where $p_{\mathcal{T}}^{(Q)}(\mathcal{T})$ is the predicted network travel time distribution for any flow rate $\langle Q \rangle$. The latter is derived from the travel time distribution in normal conditions as $p_{\mathcal{T}}^{(Q)}(\mathcal{T}) = p_{\mathcal{T}}^{(Q)_0}(\mathcal{T}\langle Q \rangle_0 / \langle Q \rangle)$, where, $\langle Q \rangle_0$ is the blood flow in normal conditions, deduced from the above simulations, for which all parameters, including the perfusion pressure, correspond to physiological data (see Methods and SI Appendix A). In other words, changing the average flow rate $\langle Q \rangle$ is equivalent to rescaling the critical time as $\tau_c \langle Q \rangle / \langle Q \rangle_0$. This also holds true when the flow rate change is induced by capillary occlusions as the shape of the travel time PDFs is similar, not only for different sets of mouse microvascular networks, but also when up to 10% of capillaries are occluded (see SI Appendix H and Fig. S6).

Under normal perfusion, the fraction of travel times larger than $\tau_c^{O_2}$ is equal to $f_p(\mathcal{T} > \tau_c^{O_2}) = 1.3\%$ (Fig. 4b). This fraction increases nonlinearly as the average flow decreases, e.g. by a factor 4 when $\langle Q \rangle$ decreases by a factor 2, an evolution accurately captured by the mean field model (Eq. (6)). As discussed above, oxygen transport is mostly controlled by the dipole-driven transport regime and its travel time distribution is relatively well represented by the mean field transport model (Fig. 4a). We thus approximate $p_{\mathcal{T}}^{(Q)_0}$ by the mean-field travel time distribution (Eq. (6)), which provides an accurate prediction of the simulated fraction of

critical travel times for all flow rates (Fig. 4b). Since the latter integrates the broad distribution of trajectory lengths, it predicts a significantly larger occurrence probability $f_p(\mathcal{T} > \tau_c^{O_2})$ than the reference CTH model (Fig. 4b), which is two orders of magnitude below the simulated probabilities under baseline perfusion. Noteworthy, the fractions of trajectories $f_p(\mathcal{T} > \mathcal{T}')$ measured at the outlet are very close to the fractions of critical vessels $f_v(\mathcal{T} > \mathcal{T}')$ within the network, i.e. vessels that are only visited by fluid elements taking a time larger than \mathcal{T}' to reach them from the inlet arterioles (SI Appendix B, Fig. S2e). Hence, the travel time statistics at the outlet venules offer a surrogate for the transport statistics within the network. As a result, the mean field model also provides a good prediction for the probability of occurrence of hypoxic vessels within the network (inset of Fig. 4b). When hypoperfusion is induced by capillary occlusions, these hypoxic vessels may likely add up to the occluded vessels, thus enhancing their impact at early stages of AD [8].

The weak diffusivity of amyloid- β amplifies the impact of anomalous transport.

We use a similar modelling method as for oxygen to relate the blood travel time statistics to amyloid- β concentrations (see Methods and SI Appendix J). Owing to its low diffusivity, amyloid- β is highly sensitive to random flow fluctuations in the capillary network as discussed above (Fig. 2a). Therefore we approximate $p_{\mathcal{T}}^{(Q)_0}$ by the CTRW model (Eqs. (7-9)). The metabolism and neurotoxicity of amyloid- β involve multiple soluble and insoluble isoforms and is still poorly understood [52, 53, 54]. To account for this uncertainty, we consider a range of critical times $\tau_c^{A\beta} = 8, 16$ or 40 s. This leads respectively to a three-, five- or tenfold arterio-venous increase of the total intravascular amyloid concentration (see Methods and SI Appendix J), which is much larger than the measured physiological increase of about 20% [55], thus yielding different degrees of compromised clearance. As expected, the probabilities of occurrence of trajectories with travel times above these critical times $f_p(\mathcal{T} > \tau_c^{A\beta})$ vary significantly with τ_c (Fig. 4c). While

the CTH model predicts an exponential evolution of the fraction of critical travel times $f_p(\mathcal{T} > \tau_c^{A\beta})$ with $\langle Q \rangle$ (linear in semi-log in Fig. 4c), the CTRW model captures the clearly non-exponential trend observed from the simulations. This is a signature of the power law scalings of travel time distributions, driven by anomalous transport. Hence, the reference CTH model underestimates the fractions of travel times with inefficient amyloid- β clearance by several orders of magnitude, while the CTRW model accurately predicts the probability of these critical travel times for all $\langle Q \rangle$ and τ_c .

Discussion

By reducing the complexity of the transport problem in anatomically realistic networks while keeping the essential physics of transport emerging from the network architecture, our analysis reveals the physical mechanisms by which the microvascular architecture shapes the blood travel time distribution. This is a major fundamental open question in microvascular physiology and a bottleneck for accurate quantification of hemodynamic parameters from brain imaging data in a broad range of applications, from clinical studies aimed at improving the diagnosis and/or staging of brain disease to fundamental studies on cerebral blood flow and metabolism, neuro-vascular coupling, cerebral autoregulation and/or blood-brain barrier function in health and disease [23].

We have demonstrated that the blood travel time distributions are driven by two fundamental mechanisms constitutive of anomalous transport dynamics [35]: broadly distributed blood trajectory length and broadly distributed capillary transit times. As schematized in Fig. 3, the former are determined by dipolar flow patterns resulting from the localized connections with upstream and downstream surface vessels, while the latter are driven by random-like fluctuations within the capillary network. For high diffusivity species, such as oxygen, travel time distributions are cut-off by diffusive transport, a third fundamen-

tal mechanism which dampens the random-like fluctuations. These fundamental insights yield the first physics-based analytical solutions for transport at the scale of cortical microvascular networks, accurately predicting the statistical distributions of travel times of different solutes, including oxygen (Eq. (6)) and amyloid- β (Eqs. (7-9)).

This offers an alternative to current effective models of transport at the scale of microvascular networks. Such models either consider simplified networks as combinations of parallel elements (e.g. [56]), overlooking the link between the transport dynamics and the underlying microvascular architecture, or use empirical functions (e.g. [14]). The latter are calibrated from in vivo measurements, which, due to blood recirculation, are limited to travel times of 5s. Extrapolation to larger time scales is constrained by the underlying parametrization chosen for the distribution of travel time, most often gamma distributions [14, 26, 57]. The resulting exponential decay underestimates the probability of large travel times that follow a slow power law decay induced by the anomalous transport dynamics uncovered here. Such models predict that a significant level of hypoperfusion, where blood flow is reduced by $\sim 20\%$ compared to normal perfusion, should be reached for hypoxic vessels to appear. Even in normal conditions, we found that a small proportion ($\sim 1.2\%$) of hypoxic vessels develop in the microvascular network. This finding is consistent with experimental measurements [16, 17]. Furthermore, accounting for anomalous transport leads to a regular non-linear increase of the proportion of hypoxic vessels with decreased flow. The impact of anomalous transport is stronger for amyloid- β , which has a smaller diffusion coefficient. Hence, the probabilities of occurrence of critical vessels with inefficient metabolic waste clearance is orders of magnitude larger than predicted by current empirical models under normal condition and their increase under hypoperfusion occurs much earlier than anticipated by these models.

Overall, these findings underpin the physical mechanisms by which moderate levels of hypoperfusion yield a non-linear expansion of hypoxic

regions and lead to increased accumulation of amyloid- β in the brain tissue. Crucially, hypoxia and amyloid- β accumulation are two key ingredients of the amyloid cascade, the positive feedback loop linking hypoperfusion and amyloid-related pathways of AD (see e.g. Fig. 3 in [10]). Combined with the recent discovery that, at early stages of AD, each single capillary occlusion has a similar, and cumulative, impact on blood flow, without any threshold effect [8], this suggests that capillary occlusions, even in small proportions, may trigger this positive feedback loop. Current numerical simulations [8] that neglect it, as well as any other compensatory effects, e.g. variations of the cerebral perfusion pressure, tend to underestimate the magnitude of hypoperfusion compared to experiments in animal models of AD. Hence, we speculate that pathological stresses induced by the amyloid cascade, e.g. pericyte activation and resulting capillary constrictions, have an outsized impact in disease progression. Our results suggest that such cascading events may be initiated by spatial heterogeneities of blood flow. In particular, as larger travel times are expected for trajectories feeding the sub-cortical regions, this may explain their specific vulnerability [58, 59], as highlighted by the appearance of white matter hyper-intensities in clinical imaging, in both cerebrovascular disease and AD [60, 29]. Besides shedding new light on the impact of capillary occlusions at early stages of AD, and more generally on the role of hypoperfusion in AD onset and progression, these findings contribute to explain the considerable overlap between vascular and neurodegenerative factors in the pathogenesis of brain disease [2, 7].

These results will also contribute to improving the quantification of physiological parameters from brain perfusion or functional imaging data, whether acquired by optical imaging, computed tomography or magnetic resonance. Such quantification generally relies on the choice of mathematical functions to represent the distribution of intravascular travel times below the scale of imaging resolution. Our findings hence establish the physical grounds for defining these travel time functions and relate

them to the microvascular architecture. This may help to account for vascular alterations, which are currently overlooked when interpreting human clinical imaging data in patient populations [61], contributing to bridge the gap with knowledge acquired from animal experiments.

The analysis of transport dynamics in highly-resolved simulations of blood flow in anatomically realistic microvascular networks is complementary to in vivo experiments in that it provides access to the full flow and transport statistics, opening a new window to decipher the underlying non-local physics. With the fast progress of numerical simulations and imaging capacities, the presented framework may be further improved. For example, larger simulations domains, possibly up to whole mice brain (see e.g. [62]) may be considered, as well as passive or active vessel diameter variations resulting from changes in blood flow, brain autoregulation and/or neurovascular coupling [23, 2, 6]. The diphasic nature of blood or more realistic reactive intravascular transport dynamics (see e.g. [63]), simplified here as first order kinetics and neglecting the oxygen binding cooperativity to hemoglobin, could also be considered in the future, as well as transport and metabolic processes within the brain tissue (see e.g. [54, 26, 64]).

Our theoretical framework hence opens new perspectives for the development of predictive, physics-based, transport models at the scale of brain microvascular networks that account for the complexity of microvascular architectures. The resulting scaling laws are generic to a large variety of networks, from simplified ones to accurate anatomical representations, with or without capillary occlusions. This suggests the uncovered anomalous transport mechanisms are general, even if the parameter values and pre-factors of scaling laws may be slightly dependent on the specific assumptions in our blood flow computational scheme. Interestingly, the predicted late time power law decay of travel time probabilities, with exponent -3 , has also been observed with a similar exponent in the coronary microcirculation [47]. This suggests that, despite the variability of microvascu-

lar architecture among organs [48, 49], blood is ultimately transported in a capillary network, where velocity fluctuations likely follow similar distributions as described here. Hence, this provides a new hypothesis for this scaling, previously interpreted as arising from an underlying fractal organization of blood flow [23, 65].

Methods

Brain microvascular networks. We use a large postmortem dataset ($\sim 15,000$ vessel segments in a $\sim 1 \text{ mm}^3$ region) from the mouse vibrissa primary sensory (vS1) cortex obtained by [66, 3] (see SI Appendix A and Supplementary Movie S1), previously used for simulation studies by [43, 67, 68, 8, 63]. Details on the procedures used for correcting the vessels diameters to match the in vivo distributions and for classifying vessels into arterioles, capillaries and venules are given in the Supplementary Material from [8]. For comparison, we use a second dataset from the same cortical region, obtained from another mouse [66, 3], as well as dense, space-filling networks of increasing complexity, including randomly-generated networks, which reproduce well the spatial and functional statistics of the mouse capillary bed [39] (SI Appendix C and H).

Simulation of blood flow and Lagrangian transport. Blood flow is modeled using a nonlinear network approach [69, 8], with prescribed boundary conditions (see SI Appendix A for details on methods and validation procedures). This yields the pressure P at each vertex and the flow rate Q and haematocrit H in each vessel. We then simulate the transport of $5 \cdot 10^7$ passive Lagrangian particles, injected from arteriolar inlets with a probability proportional to their flow rate. We advect these particles at local vessel velocity ($v = \langle Q \rangle / \langle Q \rangle_0 Q / \pi r^2$), where $\langle Q \rangle / \langle Q \rangle_0$ represents the global variation of cerebral blood flow compared to physiological baseline conditions. We distribute them in downstream vessels using flux-weighted fractions, i.e. with a probability proportional to the

local flow rate (SI Appendix B). For each particle trajectory, we computed the corresponding travel time τ and trajectory length L , i.e. the total number of visited vessels, as well as the Lagrangian transit time series (Fig. S5a, SI Appendix E). Diffusion may be taken into account by replacing, in these time series, the local (advective) transit time t by the local diffusion time ($t_D = l^2/D$) if $t_D < t$.

First order kinetics models of oxygen supply and amyloid- β clearance In order to evaluate the characteristic times associated to oxygen supply and amyloid- β clearance, we assume that they can both be described by the following first order kinetics models (see e.g. [14, 70] and SI Appendix I and J):

$$\frac{\partial c_{O_2}}{\partial t} = -k_{O_2} c_{O_2} \quad (11)$$

and

$$\begin{aligned} \frac{d(c_{A_\beta})}{dt} &= \frac{d(c_{A_\beta} - c_{A_\beta}^T)}{dt} \\ &= -k_{A_\beta} (c_{A_\beta} - c_{A_\beta}^T) \end{aligned} \quad (12)$$

where $k_{O_2}^{-1} = \tau_r^{O_2}$ and $k_{A_\beta}^{-1} = \tau_{A_\beta}$ are respectively the characteristic times for oxygen consumption in the brain tissue and for amyloid- β clearance.

Coupling these kinetics with the travel time distribution $p(\mathcal{T})$, we obtain the ratio between oxygen concentration at the outlet (venules), $c_{O_2}^V$, and at the inlet (arterioles), $c_{O_2}^A$,

$$c_{O_2}^V / c_{O_2}^A = \int_0^\infty d\mathcal{T} \exp(-k_{O_2} \mathcal{T}) p_{\mathcal{T}}(\mathcal{T}) \quad (13)$$

In the same way, we obtain the ratio between the amyloid- β concentration at the outlet (venules), $c_{A_\beta}^V$, and its tissue concentration, $c_{A_\beta}^T$,

$$\begin{aligned} c_{A_\beta}^V / c_{A_\beta}^T &= 1 - \int_0^\infty d\mathcal{T} \left\{ \left(1 - \frac{c_{A_\beta}^A}{c_{A_\beta}^T} \right) \right. \\ &\quad \left. \exp(-k_{A_\beta} \mathcal{T}) p_{\mathcal{T}}(\mathcal{T}) \right\} \end{aligned} \quad (14)$$

Using the measured travel time distribution for oxygen (Green dots in Fig. 2c), we match Eq. (13) to the typical resting oxygen extraction fraction of $\approx 30\%$ [14], which gives $c_{O_2}^V/c_{O_2}^A \approx 0.7$ [14], yielding $\tau_r^{O_2} = k_{O_2}^{-1} = 1.5$ s. Interestingly, this time is of same order as the decay time measured in single cell in vitro measurements of RBC oxygen desaturation dynamics [71], equal to 800 ms. Similarly, using typical amyloid- β concentration values (see e.g. [72, 54]) and an arterio-venous increase of 20% [55] yields $\tau_r^{A\beta} = k_{A\beta}^{-1} = 97$ s. This estimated time is of same order as can be deduced by abluminal-to-luminal permeability measurements in an in vitro blood-brain barrier model (hCMEC/D3 endothelial monolayers) [73], which yielded a permeability $P \simeq 18 \cdot 10^{-5}$ cm/min. Assuming an endothelial thickness of $\sim 1\mu\text{m}$, this leads to a characteristic time of 33 s. By contrast, previous estimates based on a compartmental model yielded $\tau_r^{A\beta} = 3000$ s [70], i.e. two orders of magnitudes above the in vitro results. Hence, despite the simplified reaction kinetics considered here, capturing the full range of travel times appears to be a key element for modelling reactive processes in the cortex.

Supplementary movies

- Supplementary Movie S1 shows a rotating view of the 1mm^3 mouse brain sample used to model the brain blood flow transport properties, corresponding to the snapshots of Fig. S1a-b. Arterioles are displayed in red, venules in blue and capillary vessels in green.
- Supplementary Movie S2 shows a rotating view of the flow rate distribution, highlighting the two flow regimes, corresponding to the snapshots of Fig. 1a and Fig. S1f. Vessel flow rates are represented with blue shades for $Q < Q_c$ and red shades for $Q > Q_c$.
- Supplementary Movie S3 shows a rotating view of all trajectories with $L \leq 30$ (orange) and $L \geq 60$ (blue) originating from the arteriole highlighted by an arrow in

Fig. 1c, corresponding to the snapshot of Fig. 1c.

- Supplementary Movie S4 shows a rotating view of typical particle trajectories with different trajectory lengths (numbers of visited vessels) (Red: $L = 20$; Yellow: $L = 30$; Orange: $L = 40$; Green: $L = 50$; Cyan: $L = 60$; Blue: $L = 70$; Violet: $L = 80$) corresponding to the snapshot of Fig. 2a.
- Supplementary Movie S5 shows a rotating view of the oxygen concentration field, corresponding to the snapshots of Fig. 5a-b.

References

- [1] Duvernoy, H. M., Delon, S., and Vannson, J. “Cortical blood vessels of the human brain”. In: *Brain research bulletin* 7.5 (1981), pp. 519–579.
- [2] Iadecola, C. “Neurovascular regulation in the normal brain and in Alzheimer’s disease”. In: *Nature Reviews Neuroscience* 5.5 (2004), pp. 347–360.
- [3] Blinder, P., Tsai, P. S., Kaufhold, J. P., Knutsen, P. M., Suhl, H., and Kleinfeld, D. “The cortical angiome: an interconnected vascular network with noncolumnar patterns of blood flow”. In: *Nature Neuroscience* 16.7 (2013), pp. 889–897.
- [4] Tarasoff-Conway, J. M., Carare, R. O., Osorio, R. S., Glodzik, L., Butler, T., Fieremans, E., Axel, L., Rusinek, H., Nicholson, C., Zlokovic, B. V., et al. “Clearance systems in the brain—implications for Alzheimer disease”. In: *Nature reviews neurology* 11.8 (2015), p. 457.
- [5] Kisler, K., Nelson, A. R., Montagne, A., and Zlokovic, B. V. “Cerebral blood flow regulation and neurovascular dysfunction in Alzheimer disease”. In: *Nature Reviews Neuroscience* 18.7 (2017), pp. 419–434.

- [6] Attwell, D., Buchan, A. M., Charpak, S., Lauritzen, M., MacVicar, B. A., and Newman, E. A. "Glial and neuronal control of brain blood flow". In: *Nature* 468.7321 (2010), pp. 232–243.
- [7] Zlokovic, B. V. "Neurovascular pathways to neurodegeneration in Alzheimer's disease and other disorders". In: *Nature Reviews Neuroscience* 12.12 (2011), pp. 723–738.
- [8] Cruz-Hernández, J. C., Bracko, O., Kersbergen, C. J., Muse, V., Haft-Javaherian, M., Berg, M., Park, L., Vinarsik, L. K., Ivasyk, I., Rivera, D. A., et al. "Neutrophil adhesion in brain capillaries reduces cortical blood flow and impairs memory function in Alzheimer's disease mouse models". In: *Nature Neuroscience* 22.3 (2019), pp. 413–420.
- [9] Nortley, R., Korte, N., Izquierdo, P., Hirunpattarasilp, C., Mishra, A., Jaunmuktane, Z., Kyrargyri, V., Pfeiffer, T., Khennouf, L., Madry, C., Gong, H., Richard-Loendt, A., Huang, W., Saito, T., Saido, T. C., Brandner, S., Sethi, H., and Attwell, D. "Amyloid beta oligomers constrict human capillaries in Alzheimer's disease via signaling to pericytes". In: *Science* (2019), eaav9518.
- [10] Korte, N., Nortley, R., and Attwell, D. "Cerebral blood flow decrease as an early pathological mechanism in Alzheimer's disease". In: *Acta Neuropathologica* (2020).
- [11] Cortes-Canteli, M. and Iadecola, C. "Alzheimer's disease and vascular aging". In: *Journal of the American College of Cardiology* 75.8 (2020), pp. 942–951.
- [12] Lorthois, S. and Cassot, F. "Fractal analysis of vascular networks: insights from morphogenesis". In: *Journal of theoretical biology* 262.4 (2010), pp. 614–633.
- [13] Hirsch, S., Reichold, J., Schneider, M., Szekeley, G., and Weber, B. "Topology and hemodynamics of the cortical cerebrovascular system". In: *Journal of Cerebral Blood Flow & Metabolism* 32.6 (2012), pp. 952–967.
- [14] Jespersen, S. N. and Østergaard, L. "The roles of cerebral blood flow, capillary transit time heterogeneity, and oxygen tension in brain oxygenation and metabolism". In: *Journal of Cerebral Blood Flow & Metabolism* 32.2 (2012), pp. 264–277.
- [15] Erdener, Ş. E. and Dalkara, T. "Small vessels are a big problem in neurodegeneration and neuroprotection". In: *Frontiers in neurology* 10 (2019), p. 889.
- [16] Parpaleix, A., Houssen, Y. G., and Charpak, S. "Imaging local neuronal activity by monitoring PO₂ transients in capillaries". In: *Nature medicine* 19.2 (2013), pp. 241–246.
- [17] Sakadžić, S., Mandeville, E. T., Gagnon, L., Musacchia, J. J., Yaseen, M. A., Yucel, M. A., Lefebvre, J., Lesage, F., Dale, A. M., Eikermann-Haerter, K., et al. "Large arteriolar component of oxygen delivery implies a safe margin of oxygen supply to cerebral tissue". In: *Nature Communications* 5 (2014), p. 5734.
- [18] Moeini, M., Lu, X., Avti, P. K., Damseh, R., Bélanger, S., Picard, F., Boas, D., Kakkar, A., and Lesage, F. "Compromised microvascular oxygen delivery increases brain tissue vulnerability with age". In: *Scientific Reports* 8.1 (2018), p. 8219.
- [19] Dong, S. "Cerebral hypoperfusion and other shared brain pathologies in ischemic stroke and Alzheimer's disease". In: *Translational Stroke Research* (2011), p. 13.
- [20] Bracko, O., Cruz Hernandez, J. C., Park, L., Nishimura, N., and Schaffer, C. B. "Causes and consequences of baseline cerebral blood flow reductions in Alzheimer's disease". In: *Journal of Cerebral Blood Flow & Metabolism* (Jan. 2021), p. 0271678X2098238.

- [21] Lipowsky, H. H., McKay, C. B., and Seki, J. "Transit time distributions of blood flow in the microcirculation". In: *Microvascular Mechanics*. Ed. by J.-S. Lee and T. C. Skalak. 1st ed. New York, NY: Springer New York, 1989, pp. 13–27.
- [22] Osch, M. J. van, Vonken, E.-j. P., Wu, O., Viergever, M. A., Grond, J. van der, and Bakker, C. J. "Model of the human vasculature for studying the influence of contrast injection speed on cerebral perfusion MRI". In: *Magnetic Resonance in Medicine* 50.3 (2003), pp. 614–622.
- [23] Zierler, K. "Indicator dilution methods for measuring blood flow, volume, and other properties of biological systems: a brief history and memoir". In: *Annals of Biomedical Engineering* 28.8 (2000), pp. 836–848.
- [24] Lassen, N. A., Henriksen, O., and Sejrsen, P. "Indicator methods for measurement of organ and tissue blood flow". In: *Comprehensive Physiology*. Ed. by R. Terjung. Hoboken, NJ, USA: John Wiley & Sons, Inc., 2011, cp020302.
- [25] Lassen, N. A. and Perl, W. *Tracer kinetic methods in medical physiology*. Raven Press, 1979.
- [26] Angleys, H., Østergaard, L., and Jespersen, S. N. "The effects of capillary transit time heterogeneity (CTH) on brain oxygenation". In: *Journal of Cerebral Blood Flow & Metabolism* 35.5 (2015), pp. 806–817.
- [27] Li, B., Esipova, T. V., Sencan, I., Kili, K., Fu, B., Desjardins, M., Moeini, M., Kura, S., Yaseen, M. A., Lesage, F., Østergaard, L., Devor, A., Boas, D. A., Vinogradov, S. A., and Sakadžić, S. "More homogeneous capillary flow and oxygenation in deeper cortical layers correlate with increased oxygen extraction". In: *eLife* 8 (2019), e42299.
- [28] Gutierrez-Jimenez, E., Cai, C., Mikkelsen, I. K., Rasmussen, P. M., Angleys, H., Merrild, M., Mouridsen, K., Jespersen, S. N., Lee, J., Iversen, N. K., Sakadžić, S., and Østergaard, L. "Effect of electrical forepaw stimulation on capillary transit-time heterogeneity (CTH)". In: *Journal of Cerebral Blood Flow & Metabolism* 36.12 (2016), pp. 2072–2086.
- [29] Eskildsen, S. F., Gyldensted, L., Nagenthiraja, K., Nielsen, R. B., Hansen, M. B., Dalby, R. B., Frandsen, J., Rodell, A., Gyldensted, C., Jespersen, S. N., Lund, T. E., Mouridsen, K., Brøndgaard, H., and Østergaard, L. "Increased cortical capillary transit time heterogeneity in Alzheimer's disease: a DSC MRI perfusion study". In: *Neurobiology of Aging* 50 (2017), pp. 107–118.
- [30] Østergaard, L., Aamand, R., Gutierrez-Jimenez, E., Ho, Y.-C. L., Blicher, J. U., Madsen, S. M., Nagenthiraja, K., Dalby, R. B., Drasbek, K. R., Mueller, A., Brøndgaard, H., Mouridsen, K., Jespersen, S. N., Jensen, M. S., and West, M. J. "The capillary dysfunction hypothesis of Alzheimer's disease". In: *Neurobiology of Aging* 34.4 (Apr. 2013), pp. 1018–1031.
- [31] Mundiyanapurath, S., Ringleb, P. A., Diatschuk, S., Hansen, M. B., Mouridsen, K., Østergaard, L., Wick, W., Bendszus, M., and Radbruch, A. "Capillary transit time heterogeneity is associated with modified Rankin scale score at discharge in patients with bilateral high grade internal carotid artery stenosis". In: *PloS one* 11.6 (2016), e0158148.
- [32] Gutiérrez-Jiménez, E., Angleys, H., Rasmussen, P. M., West, M. J., Catalini, L., Iversen, N. K., Jensen, M. S., Frische, S., and Østergaard, L. "Disturbances in the control of capillary flow in an aged APP^{swe}/PS1 Δ E9 model of Alzheimer's disease". In: *Neurobiology of aging* 62 (2018), pp. 82–94.
- [33] Merkle, C. W. and Srinivasan, V. J. "Laminar microvascular transit time distribution in the mouse somatosensory cortex revealed by Dynamic Contrast Optical Coherence Tomography". In: *NeuroImage* 125 (2016), pp. 350–362.

- [34] Kang, P. K., Dentz, M., Le Borgne, T., and Juanes, R. “Spatial Markov model of anomalous transport through random lattice networks”. In: *Physical Review Letters* 107.18 (2011), p. 180602.
- [35] Metzler, R. and Klafter, J. “The random walk’s guide to anomalous diffusion: a fractional dynamics approach”. In: *Physics reports* 339.1 (2000), pp. 1–77.
- [36] De Anna, P., Le Borgne, T., Dentz, M., Tartakovsky, A. M., Bolster, D., and Davy, P. “Flow intermittency, dispersion, and correlated continuous time random walks in porous media”. In: *Physical Review Letters* 110.18 (2013), p. 184502.
- [37] Dentz, M., Kang, P. K., Comolli, A., Le Borgne, T., and Lester, D. R. “Continuous time random walks for the evolution of Lagrangian velocities”. In: *Physical Review Fluids* 1.7 (2016), p. 074004.
- [38] Iturria-Medina, Y., Sotero, R. C., Tousseint, P. J., Mateos-Pérez, J. M., Evans, A. C., and Neuroimaging, T. A. D. “Early role of vascular dysregulation on late-onset Alzheimer’s disease based on multifactorial data-driven analysis”. In: *Nature Communications* 7 (2016), p. 11934.
- [39] Smith, A. F., Doyeux, V., Berg, M., Peyrounette, M., Haft-Javaherian, M., Larue, A.-E., Slater, J. H., Lauwers, F. d. r., Blinder, P., Tsai, P., Kleinfeld, D., Schaffer, C. B., Nishimura, N., Davit, Y., and Lorthois, S. “Brain capillary networks across species: a few simple organizational requirements are sufficient to reproduce both structure and function”. In: *Frontiers in Physiology* 10 (2019), p. 233.
- [40] Goirand, F., Georgeot, B., Giraud, O., and Lorthois, S. “Network community structure and resilience to localized damage: application to brain microcirculation”. In: *preprint arXiv:2103.08587, submitted to BrainMultiPhysics* (Mar. 2021). arXiv: 2103.08587.
- [41] Kurowski, P., Ippolito, I., Hulin, J., Koplik, J., and Hinch, E. “Anomalous dispersion in a dipole flow geometry”. In: *Physics of Fluids* 6.1 (1994), pp. 108–117.
- [42] Alim, K., Parsa, S., Weitz, D. A., and Brenner, M. P. “Local pore size correlations determine flow distributions in porous media”. In: *Physical Review Letters* 119.14 (2017), p. 144501.
- [43] Schmid, F., Tsai, P. S., Kleinfeld, D., Jenny, P., and Weber, B. “Depth dependent flow and pressure characteristics in cortical microvascular networks”. In: *PLOS Computational Biology* 13.2 (2017). Ed. by J. J. Saucerman, e1005392.
- [44] Murray, C. “The physiological principle of minimum work I. The vascular system and the cost of blood volume”. In: *Proceedings of the National Academy of Sciences* 12 (1926), pp. 207–214.
- [45] Durand, M. “Architecture of optimal transport networks”. In: *Physical Review E* 73.1 (2006), p. 016116.
- [46] Meigel, F. J. and Alim, K. “Flow rate of transport network controls uniform metabolite supply to tissue”. In: *Journal of The Royal Society Interface* 15.142 (2018), p. 20180075.
- [47] Bassingthwaighite, J. B. and Beard, D. A. “Fractal ^{15}O -labeled water washout from the heart”. In: *Circulation Research* 77.3 ().
- [48] Augustin, H. G. and Koh, G. Y. “Organotypic vasculature: From descriptive heterogeneity to functional pathophysiology”. In: *Science* 357.6353 (Aug. 2017), eaal2379.
- [49] Waters, S. L., Alastruey, J., Beard, D. A., Bovendeerd, P. H., Davies, P. F., Jayaraman, G., Jensen, O. E., Lee, J., Parker, K. H., Popel, A. S., Secomb, T. W., Siebes, M., Sherwin, S. J., Shipley, R. J., Smith, N. P., and Vosse, F. N. van de. “Theoretical models for coronary vascular biomechanics: Progress and challenges”. In: *Progress in Biophysics and*

- Molecular Biology* 104.1-3 (Jan. 2011), pp. 49–76.
- [50] Nishimura, N., Schaffer, C. B., Friedman, B., Tsai, P. S., Lyden, P. D., and Kleinfeld, D. “Targeted insult to subsurface cortical blood vessels using ultrashort laser pulses: three models of stroke.” In: *Nature Methods* 3 (2006), pp. 99–108.
 - [51] Shih, A. Y., Blinder, P., Tsai, P. S., Friedman, B., Stanley, G., Lyden, P. D., and Kleinfeld, D. “The smallest stroke: occlusion of one penetrating vessel leads to infarction and a cognitive deficit”. In: *Nature Neuroscience* 16.1 (2012), pp. 55–63.
 - [52] Dahlgren, K. N., Manelli, A. M., Stine, W. B., Baker, L. K., Krafft, G. A., and LaDu, M. J. “Oligomeric and fibrillar species of amyloid beta peptides differentially affect neuronal viability”. In: *Journal of Biological Chemistry* 277.35 (2002), pp. 32046–32053.
 - [53] Blennow, K., Hampel, H., Weiner, M., and Zetterberg, H. “Cerebrospinal fluid and plasma biomarkers in Alzheimer disease”. In: *Nature Reviews Neurology* 6.3 (2010), pp. 131–144.
 - [54] Potter, R., Patterson, B. W., Elbert, D. L., Ovod, V., Kasten, T., Sigurdson, W., Mawuenyega, K., Blazey, T., Goate, A., Chott, R., Yarasheski, K. E., Holtzman, D. M., Morris, J. C., Benzinger, T. L. S., and Bateman, R. J. “Increased in Vivo Amyloid 42 Production, Exchange, and Loss in Presenilin Mutation Carriers”. In: *Science Translational Medicine* 5.189 (2013), 189ra77–189ra77.
 - [55] Xiang, Y., Bu, X.-L., Liu, Y.-H., Zhu, C., Shen, L.-L., Jiao, S.-S., Zhu, X.-Y., Giunta, B., Tan, J., Song, W.-H., Zhou, H.-D., Zhou, X.-F., and Wang, Y.-J. “Physiological amyloid beta clearance in the periphery and its therapeutic potential for Alzheimer’s disease”. In: *Acta Neuropathologica* 130.4 (2015), pp. 487–499.
 - [56] King, R. B., Raymond, G. M., and Bassingthwaite, J. B. “Modeling blood flow heterogeneity”. In: *Annals of biomedical engineering* 24.3 (1996), pp. 352–372.
 - [57] Park, C. S. and Payne, S. J. “A generalized mathematical framework for estimating the residue function for arbitrary vascular networks”. In: *Interface focus* 3.2 (2013), p. 20120078.
 - [58] Li, B., Ohtomo, R., Thunemann, M., Adams, S. R., Yang, J., Fu, B., Yaseen, M. A., Ran, C., Polimeni, J. R., Boas, D. A., et al. “Two-photon microscopic imaging of capillary red blood cell flux in mouse brain reveals vulnerability of cerebral white matter to hypoperfusion”. In: *Journal of Cerebral Blood Flow & Metabolism* 40.3 (2020), pp. 501–512.
 - [59] Hartung, G., Badr, S., Moeini, M., Lesage, F., Kleinfeld, D., Alaraj, A., and Linninger, A. “Voxelized simulation of cerebral oxygen perfusion elucidates hypoxia in aged mouse cortex”. In: *PLOS Computational Biology* 17.1 (2021). Ed. by R. M. Merks, e1008584.
 - [60] Gorelick, P. B., Scuteri, A., Black, S. E., DeCarli, C., Greenberg, S. M., Iadecola, C., Launer, L. J., Laurent, S., Lopez, O. L., Nyenhuis, D., Petersen, R. C., Schneider, J. A., Tzourio, C., Arnett, D. K., Bennett, D. A., Chui, H. C., Higashida, R. T., Lindquist, R., Nilsson, P. M., Roman, G. C., Sellke, F. W., Seshadri, S., and on behalf of the American Heart Association Stroke Council, Council on Epidemiology and Prevention, Council on Cardiovascular Nursing, Council on Cardiovascular Radiology and Intervention, and Council on Cardiovascular Surgery and Anesthesia. “Vascular contributions to cognitive impairment and dementia: a statement for healthcare professionals from the American Heart Association/American Stroke Association”. In: *Stroke* 42.9 (2011), pp. 2672–2713.
 - [61] D’Esposito, M., Deouell, L. Y., and Gazdary, A. “Alterations in the BOLD fMRI

- signal with ageing and disease: a challenge for neuroimaging". In: *Nature Reviews Neuroscience* 4.11 (Nov. 2003), pp. 863–872.
- [62] Kirst, C., Skriabine, S., Vieites-Prado, A., Topilko, T., Bertin, P., Gerschenfeld, G., Verny, F., Topilko, P., Michalski, N., Tessier-Lavigne, M., and Renier, N. "Mapping the fine-scale organization and plasticity of the brain vasculature". In: *Cell* (2020), S0092867420301094.
- [63] Berg, M., Davit, Y., Quintard, M., and Lorthois, S. "Modelling solute transport in the brain microcirculation: is it really well mixed inside the blood vessels?" In: *Journal of Fluid Mechanics* 884 (2020).
- [64] Holter, K. E., Kehlet, B., Devor, A., Sejnowski, T. J., Dale, A. M., Omholt, S. W., Ottersen, O. P., Nagelhus, E. A., Mardal, K.-A., and Pettersen, K. H. "Interstitial solute transport in 3D reconstructed neuropil occurs by diffusion rather than bulk flow". In: *Proceedings of the National Academy of Sciences* 114.37 (2017), pp. 9894–9899.
- [65] Beard, D. A. and Bassingthwaite, J. B. "The fractal nature of myocardial blood flow emerges from a whole-organ model of arterial network". In: *Journal of vascular research* 37.4 (2000), pp. 282–296.
- [66] Tsai, P. S., Kaufhold, J. P., Blinder, P., Friedman, B., Drew, P. J., Karten, H. J., Lyden, P. D., and Kleinfeld, D. "Correlations of neuronal and microvascular densities in murine cortex revealed by direct counting and colocalization of nuclei and vessels". In: *Journal of Neuroscience* 29.46 (2009), pp. 14553–14570.
- [67] Gould, I. G., Tsai, P., Kleinfeld, D., and Linninger, A. "The capillary bed offers the largest hemodynamic resistance to the cortical blood supply". In: *Journal of Cerebral Blood Flow & Metabolism* (2016), p. 0271678X16671146.
- [68] Sweeney, P. W., Walker-Samuel, S., and Shipley, R. J. "Insights into cerebral haemodynamics and oxygenation utilising in vivo mural cell imaging and mathematical modelling". In: *Scientific Reports* 8.1 (2018).
- [69] Pries, A. R., Secomb, T. W., Gaehtgens, P., and Gross, J. "Blood flow in microvascular networks. Experiments and simulation." In: *Circulation Research* 67.4 (1990), pp. 826–834.
- [70] Shibata, M., Yamada, S., Kumar, S. R., Calero, M., Bading, J., Frangione, B., Holtzman, D. M., Miller, C. A., Strickland, D. K., Ghiso, J., and Zlokovic, B. V. "Clearance of Alzheimer's amyloid beta1-40 peptide from brain by LDL receptor related protein 1 at the blood-brain barrier". In: *Journal of Clinical Investigation* 106.12 (2000), pp. 1489–1499.
- [71] Di Caprio, G., Stokes, C., Higgins, J. M., and Schonbrun, E. "Single cell measurement of red blood cell oxygen affinity". In: *Proceedings of the National Academy of Sciences* 112.32 (2015), pp. 9984–9989.
- [72] Roberts, K. F., Elbert, D. L., Kasten, T. P., Patterson, B. W., Sigurdson, W. C., Connors, R. E., Ovod, V., Munsell, L. Y., Mawuenyega, K. G., Miller-Thomas, M. M., Moran, C. J., Cross, D. T., Derdeyn, C. P., and Bateman, R. J. "Amyloid efflux from the central nervous system into the plasma: Brain Efflux of Amyloid". In: *Annals of Neurology* 76.6 (2014), pp. 837–844.
- [73] Swaminathan, S. K., Ahlschwede, K. M., Sarma, V., Curran, G. L., Omtri, R. S., Decklever, T., Lowe, V. J., Poduslo, J. F., and Kandimalla, K. K. "Insulin differentially affects the distribution kinetics of amyloid beta 40 and 42 in plasma and brain". In: *Journal of Cerebral Blood Flow & Metabolism* 38.5 (2018), pp. 904–918.

Acknowledgments

Research reported in this publication was supported by the European Research Council under ERC grant agreements 615102 (Brain-MicroFlow) and 648377 (ReactiveFronts) and by the NIH (awards R21CA214299 and 1RF1NS110054). We gratefully acknowledge P. Blinder, P. Tsai and D. Kleinfeld for sharing anatomical networks, N. Nishimura for critically reading a previous version of this manuscript and M. Berg who developed the network flow solver.

Disclaimer

The funders had no role in the study design, data collection and analysis, decision to publish, or preparation of the manuscript.

Author contributions

All authors contributed equally to the conceptual aspects of this work and to manuscript writing. F.G. developed the numerical methods and analyzed the data. T.L.B and S.L. designed the research, jointly supervised the work and contributed to data analysis and interpretation.

Supplementary Information for "Network-driven anomalous transport is a fundamental component of brain microvascular dysfunction"

Florian Goirand, Tanguy Le Borgne and Sylvie Lorthois

April 1, 2021

A. Blood flow simulations in intracortical networks

We describe the vasculature as a network of interconnected tubes where arterioles and venules respectively act as inlets and outlets for blood flow (see Fig. **S1a-b** and Supplementary Movie S1). We compute the stationary flow rate distribution using a nonlinear network approach described in Pries et al. [1], Lorthois et al. [2] and Cruz-Hernández et al. [3]. This approach, where blood is considered as a homogeneous fluid and red blood cells are treated as a volume fraction (haematocrit), accounts for the complex rheological properties of blood flow in microcirculation through two in vivo empirical laws. The first one describes the average dissipation at vessel scale through an apparent viscosity which depends on the tube diameter and haematocrit, so that a linear relationship between the flow rate and the pressure drop can be written in each vessel [4, 5]:

$$Q_{ij} = \frac{\pi d_{ij}^4}{128\mu_{ij}l_{ij}} \Delta_{ij}P \quad (\text{S1})$$

where Q_{ij} , d_{ij} , l_{ij} , $\Delta_{ij}P$ and μ_{ij} are respectively the flow rate, the mean diameter, the length, the pressure difference and the apparent viscosity associated to vessel ij . The distribution of haematocrit in the network and phase-separation effects are captured by the second empirical law [6] that links haematocrit and flow rate ratios at diverging bifurcations.

This problem is nonlinear and is solved iteratively (see e.g. [2, 7, 5]) with the following boundary conditions: imposed physiological pressures at network inlets (one-connected arteriolar vertices located at the top-surface) and outlets (one-connected venular vertices located at the top-surface), where $P_A = 10640$ Pa and $P_V = 2660$ Pa, respectively, imposed haematocrit at network inlets ($H=0.4$), and no-flow at the bottom of the sample. Pseudo-periodic boundary conditions are used at network side faces as described in [3], with the additional constraint that, to connect two vertices located on opposite side faces, their projections on a parallel plane are closer than $80 \mu m$.

This yields the pressure, the flow rate and the haematocrit within the network, without any free parameter. The obtained flow distribution are displayed in Fig. **S1c-d**. Moreover, in Fig. **S1f**, we present the top view of Fig.1 of the main manuscript, showing the flow distribution with a discontinuous scale, highlighting the different flow regimes. The above flow distributions have been validated by comparison to in vivo measurements in mouse (see Supplementary Figure 15g-h in Cruz-Hernández et al. [3]). In addition, the range of simulated velocities at different depths

in the cortical microvessel network is consistent with experimental measurements (Fig. S1e). This supports the choice of the no-flow boundary condition at the bottom of the sample, which is the most uncertain one due to the lack of highly resolved in vivo flow data in the deep cortical layers.

For a given network architecture, the above linear system behaves linearly as a function of the perfusion pressure ($P_A - P_B$). The apparent viscosity in each vessel is indeed independent on the flow rate and, similarly, the parametrization of phase separation only depends on the flow ratio between the daughter branches. Thus, hypoperfusion resulting from a decreased perfusion pressure yields flow distributions which can be linearly deduced from the above simulations, for which all parameters, including the perfusion pressure, correspond to physiological data. When a small proportion of capillary vessels is occluded, which slightly modifies the network architecture, all velocities remain, at first order, proportional to the mean flow rate.

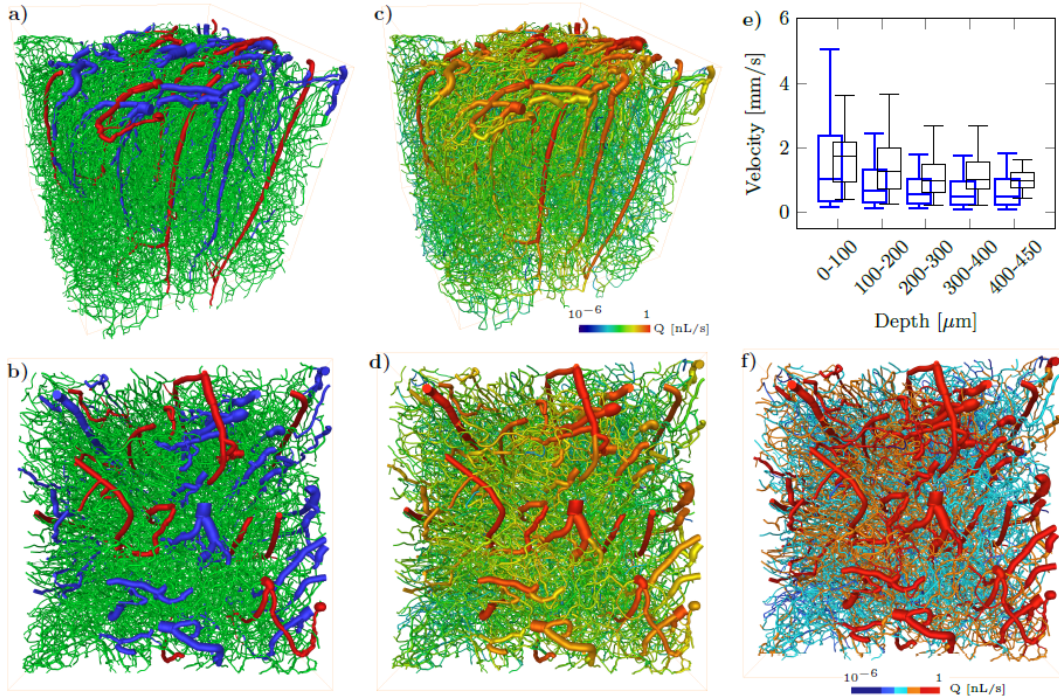


Figure S1: 3D rendering of the microvascular network, showing vessel types and flow distributions. a-b) Snapshot of the 1mm^3 mouse brain sample used to model the brain blood flow transport properties, side and top view (see Supplementary Movie S1), respectively. Arterioles are displayed in red, venules in blue and capillary vessels in green. Network inlets are defined as arteriolar vertices located at the top surface (pial surface) and connected only to a single other vertex, as apparent in b). Similarly, network outlets are defined as venular vertices located at the top surface and connected only to a single other vertex. c-d) Flow rate distribution using a continuous logarithmic color scale, side and top view respectively. e) Comparison of simulated capillary blood velocity statistics with capillary red blood cell velocity statistics measured experimentally at different cortical depths within 100 micron-thick slices. Blue: simulated average blood velocity ($4Q/\pi d^2$) from the present study; Black: experimental red-blood cell velocity data extracted from [8]. f) Same as panel d using a discontinuous color scale as in Fig. 1a of the main manuscript with blue shades for $Q < Q_c$ and red shades for $Q > Q_c$.

B. Network exploration by Lagrangian trajectories and derived quantities

Blood transport is solved by particle tracking (see Materials and Methods, Fig.2a and corresponding Supplementary Movie S2). Examples of Lagrangian trajectories originating from a given arteriole (highlighted by arrows in the figure) are displayed in Fig. S2a-d. Note that, because of the pseudo-periodic boundary conditions, these trajectories, can cross a side of the domain and connect to venules on the opposite side.

The proportion of vessels where intravascular diffusive transport dominates over advective transport (i.e. $Pe < 1$) for oxygen and amyloid- β in physiological conditions is estimated based on the vessel Péclet number $Pe = t/\tau_D$, where t is the local transit time and τ_D the diffusion time of the considered specie ($D_{O_2} = 2.10^{-9} \text{ m}^2.\text{s}^{-1}$ and $D_{A\beta} = 6.10^{-11} \text{ m}^2.\text{s}^{-1}$ [9]). For oxygen and amyloid- β in physiological conditions, it is respectively equal to 9% and 2%. Diffusion is taken into account in the Lagrangian statistics by replacing, for these vessels, the local (advective) transit time t by the local diffusion time ($t_D = l^2/D$).

The travel time distribution $p_{\mathcal{T}}(\mathcal{T})$ is computed from the Probability Density Function (PDF) of particle travel times from any inlet arteriole to any outlet venule. The fraction of travel times superior to a given threshold time \mathcal{T}' is thus $f_p(\mathcal{T} > \mathcal{T}') = \int_{\mathcal{T}'}^{\infty} d\mathcal{T} p_{\mathcal{T}}(\mathcal{T})$. To evaluate how different pathways contribute to the transport dynamics within the network, we also quantified the fraction of vessels irrigated by trajectories of different travel times. We thus defined the fraction $f_v(\mathcal{T} > \mathcal{T}')$ of vessels in the network only visited by particles with travel times larger than \mathcal{T}' . The two fractions f_p and f_v are approximately equal, as shown in Fig. S2e from oxygen transport simulations, indicating that the statistics of travel times measured at the outlet are representative of the travel time statistics within the network.

To understand how particles of different lengths explore the different vessels (arterioles, venules, capillaries), we computed the average number of visited capillaries \bar{n}_c as a function of trajectory length L (Fig. S2f). The number of visited capillaries initially increases until $L \approx 20$ and then reaches a plateau at $\bar{n}_c \approx 10$. Above L_c , the number of visited capillaries increases again linearly. Therefore below L_c , trajectories increase their lengths by visiting more arterioles and venules, as they penetrate deeper into the network (see Fig. S2a-b and schematic of Fig.3 in the main manuscript). Above L_c , the steep increase of the number of visited capillaries with trajectory length reflects the exploration of the deep capillary bed by longer blood flow paths (see Fig. S2c-d and schematic of Fig.3 in the main manuscript).

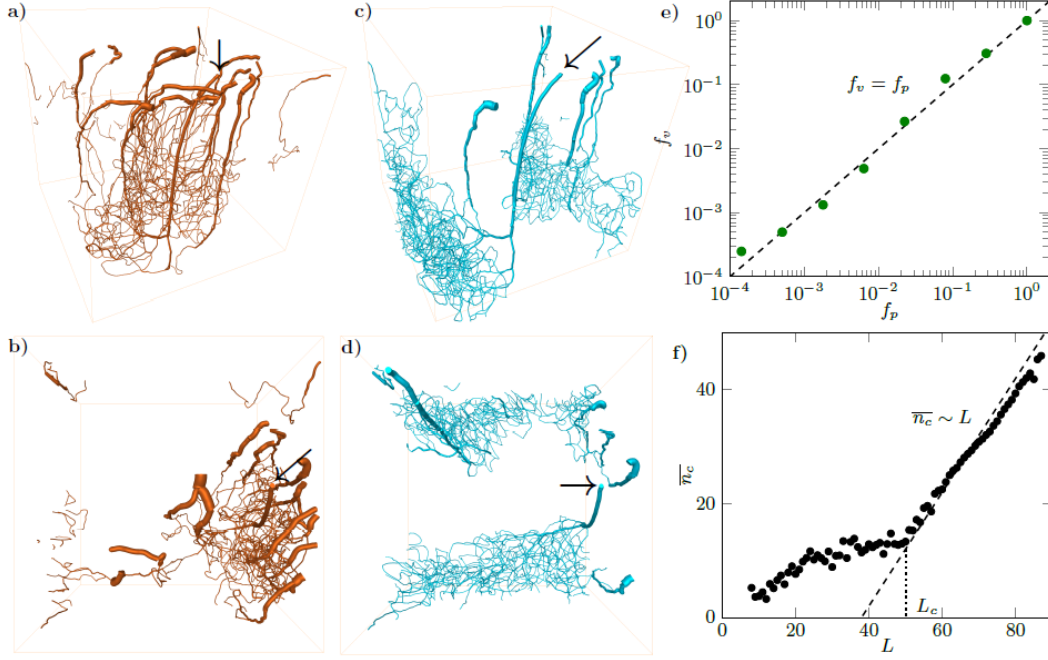


Figure S2: Exploration of the network by Lagrangian trajectories a-b) Snapshots showing all particle trajectories originating from a single arteriole (highlighted by the arrow), with length smaller than $L = 30$, respectively side and top view and **c-d)** with length than $L = 70$. Note that, because of the pseudo-periodic boundary conditions, trajectories originating from a given arteriole, can cross a side of the domain and connect to venules on the opposite side. Trajectories are the same as in Fig. 1 of the main manuscript. **e)** Fraction $f_v(\mathcal{T} > \mathcal{T}')$ of vessels only visited by particles with travel times from the inlet to the vessel larger than \mathcal{T}' as a function of the fraction $f_p(\mathcal{T} > \mathcal{T}')$ of network travel times larger than \mathcal{T}' . The dashed line represents $f_p = f_v$. **f)** Evolution of the average number of capillaries \bar{n}_c within trajectories as a function of trajectory length L . The dashed line highlights the linear tendency $\bar{n}_c \sim L$.

C. Dipole flows on networks

To investigate the similarities and differences between the results obtained in intracortical networks and the results obtained in simpler networks, we compared the flow and transport statistics of different systems. We considered i) the classical solution of dipole flow in a 2D finite size continuous homogeneous medium [10] (Fig. S3a), ii) a dipole flow in a 2D square lattice with homogeneous conductances (Fig. S3b), and iii) a superposition of multiple dipole flows in a 3D random space-filling network with homogeneous conductances constructed following the method of Smith et al. [11] to reproduce the topological and functional properties of intracortical capillary networks (Fig. S3c).

We first recall basic theoretical results derived by Kurowski et al. (1994)[10] for a dipole flow created by a source and sink separated by a distance a in a homogeneous layer of thickness d limited by a circular impervious boundary of radius R . Taking the center of the line joining the source and sink as the reference point ($r = 0$), the velocity field can be expressed in polar

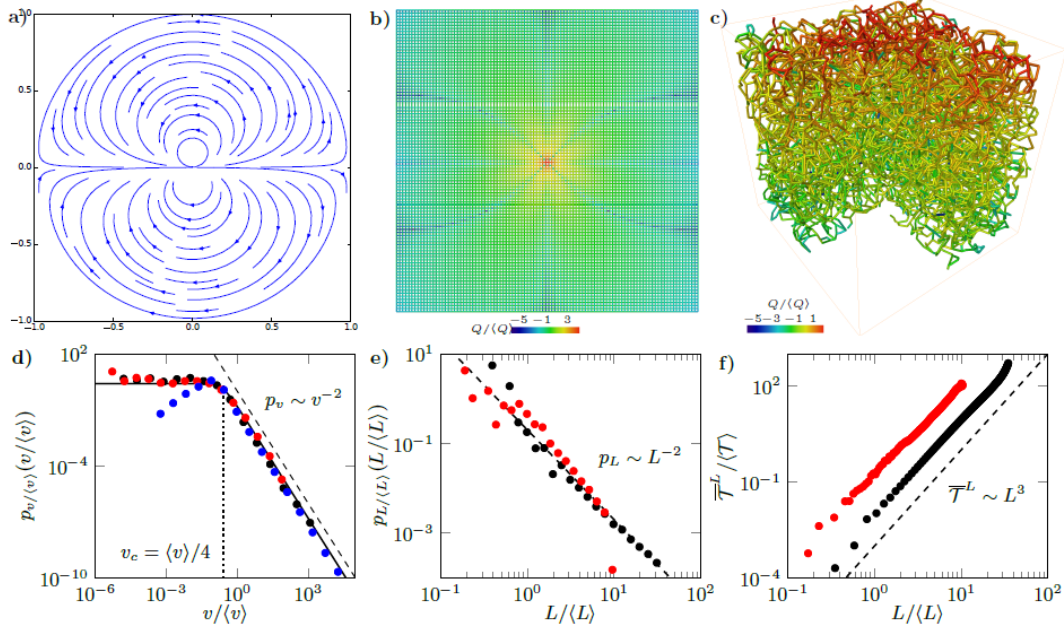


Figure S3: Blood flow and trajectory statistics in dipole flows of increasing complexity. **a)** Streamlines for a single dipole flow in a 2D finite size continuous medium plotted using the solution of Kurowski et al. [10]. **b)** Flow distribution for a single dipole flow in a 2D square lattice with homogeneous conductances obtained by numerical simulation. The color scale represents the logarithm of $Q/\langle Q \rangle$. **c)** Flow distribution generated by a random distribution of inlet and outlet points on the upper surface of a synthetic 3D space-filling disordered network. The color scale represents the logarithm of $Q/\langle Q \rangle$. A quarter of the volume has been removed to enable visualization of the central part of the network. **d)** Velocity PDFs for the dipole flow in a finite continuous medium (blue), the dipole flow in a square lattice (black) and multiple dipole flows in a 3D random network (red), **e)** PDFs of trajectory lengths for the dipole flow in a square lattice (black) and multiple dipole flows in a 3D random network (red), and **f)** relationship between average travel time and trajectory length for the dipole flow in a square lattice (black) and multiple dipole flows in a 3D random network (red).

coordinates as:

$$\begin{cases} v_r = \frac{q_0 a}{2\pi d} \cos \theta \left(\frac{1}{r^2} - \frac{1}{R^2} \right) \\ v_\theta = \frac{q_0 a}{2\pi d} \sin \theta \left(\frac{1}{r^2} + \frac{1}{R^2} \right) \end{cases} \quad (\text{S2})$$

where r is the distance from the center and q_0 is the inlet and outlet flow rate. The velocity magnitude $v = \sqrt{v_r^2 + v_\theta^2}$ is,

$$v = \frac{q_0 a}{2\pi d} \sqrt{\cos^2 \theta \left(\frac{1}{r^2} - \frac{1}{R^2} \right)^2 + \sin^2 \theta \left(\frac{1}{r^2} + \frac{1}{R^2} \right)^2} \quad (\text{S3})$$

For $r \ll R$, the velocity magnitude thus evolves as,

$$v(r) \underset{r \ll R}{\sim} \frac{q_0}{r^2}. \quad (\text{S4})$$

which leads through the change of variable $p_v(v)dv = p_r(r)rdr$ to the velocity PDF,

$$p_v(v) \sim q_0 v^{-2} \quad (\text{S5})$$

This scaling is verified in Fig. S3d for $v > v_c$, with the characteristic velocity $v_c = \langle v \rangle / 4$. Below v_c , the PDF evolves as $p_v \sim v$. The large velocity scaling $p_v(v) \sim v^{-2}$ is also recovered for the dipole flow in a square lattice (Fig. S3b). However, the low velocity regime is replaced by a uniform distribution, as observed in our biological network. As discussed in the main manuscript, this confirms that the uniform distribution at low flows is related to the network structure.

Far from the dipole, the streamlines may be approximated as circles of radius r and length $L = 2\pi r$ [10]. The travel time derived by integration of the velocity along r given by Eq. (S4) is thus,

$$\bar{\tau} = \int_0^L \frac{dr}{v(r)} \sim L^3 \quad (\text{S6})$$

This is verified in Fig. S3f for a single dipole flow in a 2D square network (Fig. S3b). Kurowski et al. (1994) have further shown that the resulting travel time PDF for a single dipole in a homogeneous 2D medium is [10],

$$p_{\mathcal{T}}(\mathcal{T}) \sim \mathcal{T}^{-4/3} \exp(-\mathcal{T}/\mathcal{T}_c) \quad (\text{S7})$$

where $\mathcal{T}_c = R^3/q_0$. Through the change of variable $p_L(L)dL = p_{\mathcal{T}}(\mathcal{T})d\mathcal{T}$ this leads to,

$$p_L(L) \sim L^{-2}, \quad (\text{S8})$$

which is verified in Fig. S3e for a single dipole flow on a homogeneous 2D network.

We have investigated the statistical measurements described above for flow in 3D random space-filling network with homogeneous conductances (Fig. S3c), which are representative of the capillary bed structure [11]. Sixteen inlet points and 16 outlet points were randomly distributed at the surface of a random cubic network of $\sim 25^3$ vessels. Boundary conditions are imposed pressure on inlets and outlets and no flow on all other vessels at the boundary. The statistics of velocities and trajectory lengths, as well as the average travel time dependency with the trajectory length, appear to all follow the same statistics as the 2D network (Fig. S3d-f). This suggests that although the system is three-dimensional, the streamline patterns behave statistically as 2D dipoles. This behavior results from the multiple dipolar injection and extraction at the surface of the network, which constrains the streamlines to extend mostly vertically in the network, therefore being topologically equivalent to 2D dipoles.

In 3D systems with embedded dipoles far from each other, the velocity is expected to decay as $v(r) \sim r^{-3}$, leading from Eq. (S6) to the mean travel time:

$$\bar{\tau} \sim L^4. \quad (\text{S9})$$

This scaling is observed for large trajectory lengths in our microvascular network simulations (see inset of Fig. 2c in the main document and Fig. S4b). We interpret this transition to 3D dipole flows as resulting from the decrease in density of arterioles and venules in the depth of the cortex [12]. At their capillary ends, deep arterioles and venules are further from each other compared to their typical separation distance at the surface and the streamline patterns are therefore less constrained laterally and can develop large trajectories in the capillary bed (see schematic of Fig. 3 in the main manuscript), following the characteristic scaling of 3D dipoles.

As discussed above, many characteristics of dipole flow in continuous systems are recovered in the periodic lattices and random networks considered above. A notable difference concerns the

flow distribution in the low flow range: the flow rate PDF for both periodic and random networks exhibits a plateau at low values, a signature of the network structure which is consistent with the findings of Alim et al. [13]. The latter suggest that flow distributions in random networks follow exponential PDFs, leading to the plateau at small flows. This uniform distribution of flow at low values, also observed in our biological networks, is at the origin of the broad distribution of vessel transit time discussed in the main manuscript. Thus, in the large flow rate and short trajectory length regime, microvascular networks are analogous to dipole flows in that they follow the scalings of Eq. (S5) and Eq. (S8) (see Fig. 1b and Fig. 2b in the main manuscript). However, the relationship between travel times and trajectory lengths (see Inset of Fig. 2c in the main text) is different from that expected for simple dipole flow (Eq. (S6)). The later exhibits a linear tendency for $L < L_c$ and then a power law with exponent 4, similar to Eq. (S9). We understand this difference as follows.

Trajectory lengths smaller than L_c , i.e in the first linear regime, correspond to trajectories with direct connections occurring at different depths between neighboring arterioles and venules [14], see schematic of Fig.3 and Fig. S2a,b, where most venules connected to the injection arteriole lie in a cylindrical region of radius $\sim 700 \mu m$ around it. Depending on the trajectory length L , these connections occur at different depths, but the pressure drop throughout the capillary bed is approximately constant. In fact, because they have larger diameters, pressure drops within arterioles and venules are small compared to pressure drops throughout the capillary network. Consistently, the number of visited capillaries in these trajectories depends weakly on the trajectory length (Fig. S2f). This implies that the average capillary transit time in these trajectories is the same for any $L < L_c$. Hence, as the trajectory length increases, the additional visited vessels belong to arterioles and venules for $L < L_c$. As discussed in the main manuscript, the linear scaling of $\bar{\tau}^L(L)$ indicates that the average transit time t in such vessels remains approximately constant as trajectories explore deeper sections of the network.

Trajectories of lengths larger than L_c correspond to connections between arterioles and more distant venules (Fig.3 and Fig. S2c,d), and include a number of capillaries linearly growing with the trajectory length (Fig. S2f). As explained above, in the deep part of the cortex, blood trajectories are driven by the 3D dipolar nature of the flow in between these distant arteriole and venules. Therefore, they follow the average time-length scaling expected for 3D dipole flows (Eq. S9).

D. Mean field transport model

The mean field transport model $p_{\bar{\tau}}(\bar{\tau})$ is derived by associating to each trajectory of length L a mean travel time, i.e. averaged over all trajectories of same length. This is equivalent to removing the noise induced by flow fluctuations linked to the random network structure. The mean field model is obtained analytically from the average travel time $\bar{\tau}^L$ for a given trajectory length L and the trajectory length PDF $p_L(L)$ using the change of variable $p_{\bar{\tau}}(\bar{\tau})d\bar{\tau} = p_L(L)dL$. The average travel time is characterized by a transition from a linear to power law behavior, driven by the flow organization respectively in the superficial and deep microvascular network (Eq. (5) in the main manuscript and Appendix C),

$$\begin{cases} \bar{\tau}^L(L) \approx \tau_1(L - L_0) + \tau_0 & L_0 < L \leq L_c \\ \bar{\tau}^L(L) \approx \tau_c \left(\frac{L}{L_c} \right)^4 & L > L_c \end{cases} \quad (S10)$$

These trends are shown in linear and loglog plots in Fig. S4a-b (same as inset of Fig.2c in the main manuscript). The trajectory length PDF (Eq. (4) and Fig.2b of the main manuscript) is

$$\begin{cases} p_L(L) \sim L^{-2} & L_0 < L \leq L_c \\ p_L(L) \sim \exp(-L/L^*) & L > L_c \end{cases} \quad (\text{S11})$$

The mean field travel time PDF is $p_{\bar{\mathcal{T}}} = p_L(L(\bar{\mathcal{T}})) \frac{dL}{d\bar{\mathcal{T}}}$, leading to a transition from a power law to a stretched exponential:

$$\begin{cases} p_{\bar{\mathcal{T}}}(\bar{\mathcal{T}}) \sim ((\bar{\mathcal{T}} - \mathcal{T}_0)/\tau_1 + L_0)^{-2}, & \text{for } \bar{\mathcal{T}} < \mathcal{T}_c \\ p_{\bar{\mathcal{T}}}(\bar{\mathcal{T}}) \sim \left(\frac{\bar{\mathcal{T}}}{\mathcal{T}_c}\right)^{-3/4} \exp\left(-\frac{L_c}{L^*} \left(\frac{\bar{\mathcal{T}}}{\mathcal{T}_c}\right)^{1/4}\right), & \text{for } \bar{\mathcal{T}} > \mathcal{T}_c \end{cases} \quad (\text{S12})$$

We compare this analytical prediction to the numerical estimation of the mean field travel time PDF $p_{\bar{\mathcal{T}}}(\bar{\mathcal{T}})$, obtained by computing $\bar{\mathcal{T}}^L$ for each trajectory length and calculating its PDF for all trajectory lengths (Fig. S4c). The mean field travel time PDF is identical to the full travel time PDF up to a time of about $\mathcal{T} = 10$ s. Above this time, the full travel time PDF deviates to follow the power law trend $p_{\mathcal{T}} \sim \mathcal{T}^{-3}$, resulting from the noise component (see Appendix E and F). The analytical prediction of Eq. (S12) is in good agreement with the computed mean field PDF over the full range of times (Fig. S4c).

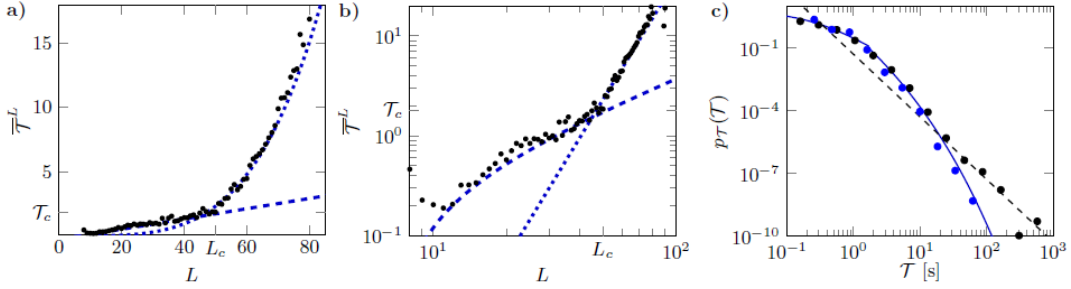


Figure S4: Characteristics and predictive power of the mean field model. Average travel time $\bar{\mathcal{T}}^L$ as a function of trajectory length L in **a)** linear scale **b)** loglog scale (same as inset of Fig.2c in the main manuscript). The linear and power law tendencies (Eq. (S10)) are shown respectively as dashed and dotted blue lines. The transition travel time and trajectory lengths between these two tendencies are indicated as \mathcal{T}_c and L_c . **c)** Full travel time PDF (black dots) compared to the numerical mean field travel time PDF (blue dots). The theoretical mean field model is shown as a blue line. The late time power law tendency $p_{\mathcal{T}} \sim \mathcal{T}^{-3}$ characteristic of noise-driven anomalous transport in the late time regime is shown as a black dashed line.

E. Noise in vessel transit time induced by random network fluctuations

The series of local transit times along a given trajectory exhibit large erratic fluctuations around the series of average transit times (Fig. S5a). To analyze these fluctuations, induced by the randomness of the network, we define a noise term ξ by normalizing the vessel transit time t_j at the j^{th} step by its mean value $\overline{t_j^L}$, where $\overline{\cdot}^L$ denotes the average over trajectories of size L ,

$$\xi = \frac{t_j}{\overline{t_j^L}}. \quad (\text{S13})$$

The statistics of these fluctuations p_ξ are found to be independent on the trajectory length (Fig. S5b). Large fluctuations of ξ , which control long times, follow a power law $p_\xi(\xi) \sim \xi^{-3}$. This trend is consistent with the Lagrangian transit times distribution, which follows the same power law scaling (Fig. S5c). This power law behavior is linked to the Eulerian vessel transit time distribution, which follows $p_t^e(t) \sim t^{-2}$ at large times (Eq. 3 in the main manuscript). Indeed, the Lagrangian transit times statistics $p_t^\ell(t)$, that is the statistics of vessel transit times sampled by particle trajectories, are weighted by the local flow rate $Q \sim 1/t$ [15], leading to

$$p_t^\ell(t) \sim p_t^e(t)/t \sim t^{-3}. \quad (\text{S14})$$

As discussed in the main manuscript, this power law scaling for long transit times is induced by the uniform distribution of low flow rates (see Fig.1b in the main manuscript). Such uniform distributions are characteristic of flow in random networks (Fig.S3d), which follow exponential distributions and therefore are constant at low values [13]. Assuming an exponential model of flow rate fluctuations induced by random network connections, we obtain, after change of variable and weighting by flow, the following noise PDF for fluctuations of vessel transit times,

$$p_\xi(\xi) = \frac{\exp(-1/\xi)}{\xi^3}, \quad (\text{S15})$$

which is in good agreement with measured noise in the large fluctuation range, i.e. for $\xi \geq 1$ (Fig. S5b).

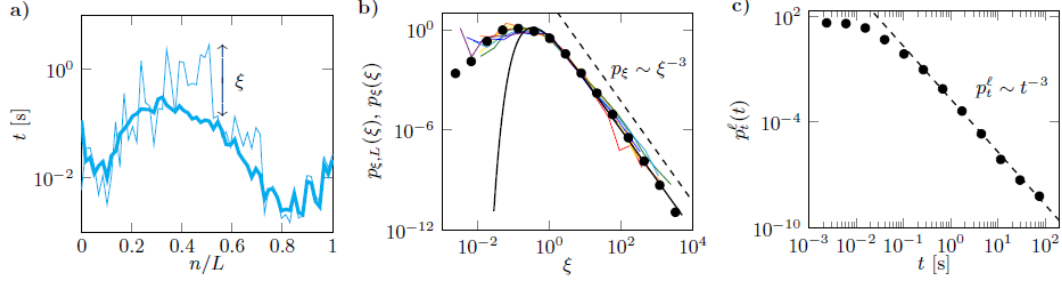


Figure S5: Statistics of Lagrangian capillary transit times. **a)** Series of local and averaged transit times for trajectories of equal lengths ($L = 60$), as a function of the number n of vessels visited since the inlet arteriole. The thick line shows the average trend (as in the inset of Fig. 2b in the main manuscript) and the thin line shows an example of transit time series along one trajectory. The noise ξ is defined as the ratio of the local to the average transit time at a given position n/L (Eq. (S13)). **b)** Noise probability density functions. Colored lines show the noise PDF $p_{\xi,L}(\xi)$ for different trajectory lengths $L = \{20, 30, 40, 50, 60, 70, 80\}$ with the color convention from Fig. 2 of the main manuscript. The black dots show the noise PDF averaged over all trajectory lengths $p_{\xi}(\xi)$. The black line represents the analytical approximation of Eq. (S15) for large noise values. The dashed line shows the power law trend for large fluctuations. **c)** Lagrangian transit time PDFs (black dots). The dashed line shows the power law trend (Eq. (S14)).

F. Analytical derivation of the Continuous Time Random Walk model

In complement to the mean field transport model that captures the effect of dipole-driven trajectory lengths distributions, we derived a stochastic transport model integrating in addition the effect of network-driven transit time fluctuations. Fluid elements move to one vessel to the next with a broadly varying transit time, which corresponds closely to the Continuous Time Random Walk representation [16, 17, 18]. In this framework, the travel time \mathcal{T}_j after $j - 1$ vessels evolves as:

$$\mathcal{T}_{j+1} = \mathcal{T}_j + t_j \quad (\text{S16})$$

with t_j the time increments at vessel j . From Eq. (S13) we take $t_j = \xi_j \bar{t}_j^L$, where ξ_j is a random noise with distribution $p_{\xi}(\xi)$. From the mean field model (Eq. (S10)) we have $\bar{t}_j^L = \tau_1$ for $L < L_c$ and $\bar{t}_j^L = \frac{\mathcal{T}_c(L/L_c)^4 - \mathcal{T}_c}{L - L_c}$ for $L > L_c$, leading to,

$$\begin{cases} t_j = \xi_j \tau_1 & L_0 \leq j < L_c \\ t_j = \xi_j \frac{\mathcal{T}_c(L/L_c)^4 - \mathcal{T}_c}{L - L_c} & L_c \leq j < L \end{cases} \quad (\text{S17})$$

The temporal increment in the CTRW model (Eq. (S16)) hence integrates the mean field field travel time distribution driven by the dipole flow patterns through \bar{t}_j^L and the network fluctuations quantified by the noise term ξ_j . Because we focus on the impact of long travel times, we do not consider trajectories smaller than L_0 , which is the smallest trajectory length in the mean field model (Fig. S4a). Therefore, the CTRW model is initialized at $\mathcal{T}_{L_0} = \mathcal{T}_0$.

The total network travel time is,

$$\mathcal{T} = \mathcal{T}_0 + \sum_{j=L_0}^{L-1} t_j \quad (\text{S18})$$

Since the time increments t_j are independent, the travel time PDF is,

$$p_{\mathcal{T}}(\mathcal{T}) = \sum_{L=L_0+1}^{\infty} p_L(L) \int_0^{\infty} dt_{L_0} \dots \int_0^{\infty} dt_{L-1} p_{t,L_0}(t_{L_0}) \dots p_{t,L-1}(t_{L-1}) \delta \left(\mathcal{T}_0 + \sum_{j=L_0}^{L-1} t_j - \mathcal{T} \right) \quad (\text{S19})$$

Since the trajectory distribution $p_L(L)$ and the relation between mean travel time and length follow different regimes above and below L_c , we decompose Eq. (S19) as a sum of two contributions:

$$p_{\mathcal{T}}(\mathcal{T}) = p_{\mathcal{T}}^1(\mathcal{T}) + p_{\mathcal{T}}^2(\mathcal{T}) \quad (\text{S20})$$

where

$$p_{\mathcal{T}}^1(\mathcal{T}) = \sum_{L=L_0+1}^{L_c} p_L(L) \int_0^{\infty} d\xi_{L_0} \dots \int_0^{\infty} d\xi_{L-1} p(\xi_{L_0}) \dots p(\xi_{L-1}) \delta \left(\mathcal{T}_0 + \tau_1 \sum_{j=L_0}^{L-1} \xi_j - \mathcal{T} \right), \quad (\text{S21})$$

$$p_{\mathcal{T}}^2(\mathcal{T}) = \sum_{L=L_c+1}^{\infty} p_L(L) \int_0^{\infty} d\xi_{L_0} \dots \int_0^{\infty} d\xi_{L-1} p(\xi_{L_0}) \dots p(\xi_{L-1}) \delta \left(\mathcal{T}_0 + \tau_1 \sum_{j=L_0}^{L-1} \xi_j + \frac{\mathcal{T}_c(L/L_c)^4 - \mathcal{T}_c}{L - L_c} \sum_{j=L_c}^{L-1} \xi_j - \mathcal{T} \right). \quad (\text{S22})$$

Eq. (S21) and Eq. (S22) can be expressed in Laplace space respectively as,

$$\tilde{p}_{\mathcal{T}}^1(s) = e^{-s\mathcal{T}_0} \sum_{L=L_0+1}^{L_c} p_L(L) \mathcal{P}^{L-L_0}(s\tau_1) \quad (\text{S23})$$

and

$$\tilde{p}_{\mathcal{T}}^2(s) = e^{-s\mathcal{T}_0} \mathcal{P}^{L_c-L_0}(s\tau_1) \sum_{L=L_c+1}^{\infty} p_L(L) \mathcal{P}^{L-L_c} \left(s \frac{\mathcal{T}_c(L/L_c)^4 - \mathcal{T}_c}{L - L_c} \right) \quad (\text{S24})$$

where $\mathcal{P} = \mathcal{L}\{p_{\xi}(\xi)\}$ is the Laplace transform of $p_{\xi}(\xi)$. For the noise PDF $p_{\xi}(\xi)$ we take the analytical expression of Eq. (S15), which provides a good approximation for large fluctuations $\xi \geq 1$ (Fig. S5). Its Laplace transform is $\mathcal{P}(s) = 2sK_2(2\sqrt{s})$ with s the Laplace variable and K_2 is a modified Bessel function of the second kind.

The CTRW model (Eq. (S20)), solved by numerical Laplace inversion of Eq. (S23) and Eq. (S24), provides an accurate prediction of the advective travel time PDF for $\mathcal{T} > \mathcal{T}_0$ (Fig. 4a in the main manuscript) with no fitting parameter. This model is thus fully determined from the trajectory length PDF (Eq. (S11)) and the relationship between average time and trajectory length (Eq. (S10)). Model predictions are also consistent with the travel time distributions of oxygen and amyloid- β up to a cut off time driven by diffusion.

G. Reference CTH model

To investigate the effect of the long network travel times, which cannot be accessed by in vivo measurements, we compare our model prediction to that of a reference CTH model calibrated from experimental data [19]. The latter assumes that the travel time PDF follows a Gamma distribution,

$$p_{\mathcal{T}}(\mathcal{T}) = \frac{\mathcal{T}^{n-1}}{\Gamma(n)\theta^n} e^{-\mathcal{T}/\theta} \quad (\text{S25})$$

where the parameters n and θ are related to the travel time mean and variance as $\overline{\mathcal{T}} = n\theta$ and $\sigma_{\mathcal{T}}^2 = n\theta^2$, respectively. Jespersen et al. [19] have compiled a series of experimental data obtained in various physiological conditions and shown that these moments follow the approximate relationship $\sigma_{\mathcal{T}} \approx 0.7\overline{\mathcal{T}}$ (see symbols in Figure 4 of Jespersen et al. [19]). Using this relationship and the average travel time in our simulations, $\overline{\mathcal{T}} = 0.66$ s, we estimate the parameters of the reference model to be $n = 2$ and $\theta = 0.32$ for the considered microvascular network. Since experimentally measured travel time distributions are limited to times smaller than ~ 5 s due to blood recirculation [20, 21], this empirical model serves here as a reference to assess the effect of neglecting the experimentally inaccessible longest travel times.

H. Robustness of flow and transport properties across anatomical networks

We have previously shown [11] that the size of a representative elementary volume (REV) for the capillary bed is ($\sim 400 \times 400 \times 400 \mu m^3$). Thus, the microvessel network (Fig. S1.a) used in the present simulations contains more than 10 representative elementary volumes (REV) for the capillary bed. Moreover, for this network, the ratio between the number of penetrating arterioles and of ascending venules, which gives insight on the large-scale structures superimposed to the capillary bed, corresponds to the average ratio in the cortex. Thus, we expect to obtain statistically robust results.

In this section, we check this and further test the generality of our results using two different micro-vascular networks: the same network as shown in Fig. S1.a, but with 10 % randomly stalled capillaries, and another network extracted from the same region of the mouse brain previously obtained by Tsai et al. [22] and Blinder et al. [23]. The flow statistics are found to be very similar in all networks and consistent with our stochastic model (Fig. S6.a). As a consequence, our transport model is in good agreement with the travel time distributions in all networks (Fig. S6.b).

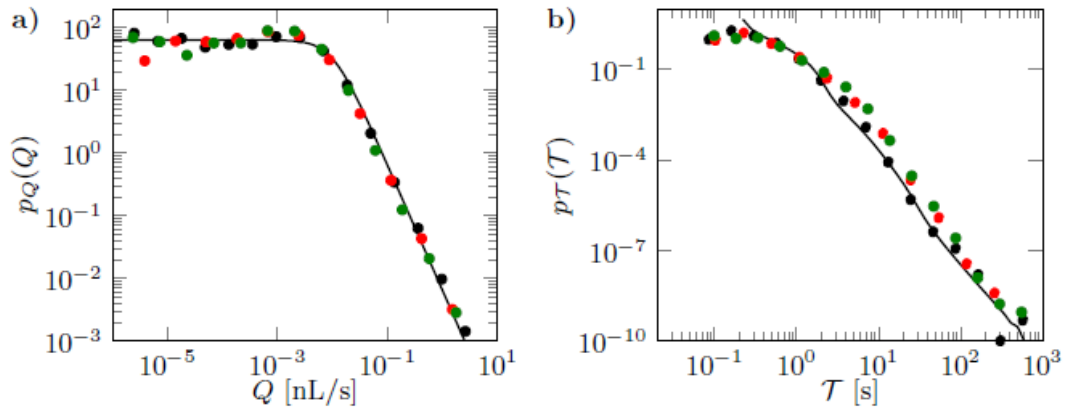


Figure S6: Statistics of flow and transport in a stalled micro-vascular network and in a different sample network. a) Flow rate PDFs. b) Travel time PDFs. Black dots represent the results from the network presented in Fig. S1. Red dots represent the results for this same network with 10% of stalled capillaries. Green dots represent the results for another network drawn from the same region of the mouse brain. The continuous lines in sub-figure a) and b) represent respectively our flow PDF (Eq. (1) in the main text) and transport models (Eq. (7) in the main text).

I. Reactive transport of oxygen

To investigate the impact of the travel time distribution on oxygen transport within the brain cortex, we use a simplified Lagrangian model of transport in vessels coupled to diffusive mass transfer and consumption in the brain tissue. We consider a transported element of fluid carrying an oxygen concentration c_{O_2} . Diffusive mass transfer from the vessel to the tissue is modeled by a first-order exchange kinetics,

$$\frac{\partial c_{O_2}}{\partial t} = -k(c_{O_2} - c_{O_2}^T) \quad (S26)$$

where $c_{O_2}^T$ is the local averaged concentration in the brain tissue next to the vessel and k^{-1} is the characteristic diffusion time across the vessel walls. The oxygen concentration in the tissue $c_{O_2}^T$ evolves through consumption and diffusive mass transfer with the vessel as,

$$\frac{\partial c_{O_2}^T}{\partial t} = -k_{O_2} c_{O_2}^T + k(c_{O_2} - c_{O_2}^T) \quad (S27)$$

where k_{O_2} is the first order kinetic constant for oxygen consumption in the brain tissue. Since the characteristic diffusion time across the vessel walls, $\frac{e^2}{D_{O_2}} \sim 5 \times 10^{-4} s$ (taking $e \sim 1 \mu m$ for capillary vessels [24]), is small, we assume that $k \gg k_{O_2}$, so that oxygen in the tissue is locally in equilibrium with oxygen in blood ($c_{O_2}^T \simeq c_{O_2}$). This yields:

$$\frac{\partial c_{O_2}}{\partial t} = -k_{O_2} c_{O_2}, \quad (S28)$$

a first order equation similar as the one used by [19]. Solving for this equation yields:

$$c_{O_2}(T) = c_{O_2}(0) \exp(-k_{O_2} T) \quad (S29)$$

where T is the local travel time from the inlet along a given trajectory and $c_{O_2}(0) = c_{O_2}^A$ is the oxygen concentration at the arterial inlets. Because the kinetics are linear, the oxygen concentration carried by each fluid element can be resolved independently and then added to reconstruct the oxygen distribution in the network. In other words, the average concentration in a given vessel is deduced as the average of local concentrations of all trajectories flowing through this vessel, yielding the oxygen concentration field throughout the network for a given kinetic constant k_{O_2} (Fig. 5a,b in the main manuscript).

J. Amyloid- β clearance

We model amyloid- β clearance using similar assumptions as for oxygen. Due to tissue production, the tissue amyloid- β concentration, $c_{A\beta}^T$, is much higher than the blood amyloid- β concentration, $c_{A\beta}^A$ (see e.g. [25] where $c_{A\beta}^A=264$ pg/ml and [26] where $c_{A\beta}^T=8150$ pg/ml, as measured by the same immunoprecipitation/mass spectrometry technique). Thus, we assume that $c_{A\beta}^T$ is approximately constant because of tissue production. Taking a linear mass transfer between the tissue and the vessels [27], we obtain,

$$\frac{d(c_{A\beta})}{dt} = \frac{d(c_{A\beta} - c_{A\beta}^T)}{dt} = -k_{A\beta}(c_{A\beta} - c_{A\beta}^T) \quad (\text{S30})$$

where $k_{A\beta}^{-1}$ is the characteristic time for amyloid- β clearance. Solving this equation leads to:

$$c_{A\beta}(t) - c_{A\beta}^T = (c_{A\beta}(0) - c_{A\beta}^T) \exp(-k_{A\beta}t) \quad (\text{S31})$$

where $c_{A\beta}(0) = c_{A\beta}^A$ is the amyloid- β concentration at the arterial inlets.

Thus, for each trajectory with travel time \mathcal{T} , the ratio between the venous outlet concentration $c_{A\beta}^v$ and tissue concentration is given by,

$$c_{A\beta}^v/c_{A\beta}^T = 1 - (1 - \frac{c_{A\beta}^A}{c_{A\beta}^T}) \exp(-k_{A\beta}\mathcal{T}) \quad (\text{S32})$$

This simplifies to

$$c_{A\beta}^v/c_{A\beta}^T = 1 - \exp(-k_{A\beta}\mathcal{T}) \quad (\text{S33})$$

when the travel time is much larger than $\frac{c_{A\beta}^A}{c_{A\beta}^T} k_{A\beta}^{-1}$. As for the oxygen model, we couple this first order model of amyloid production in tissues with the typical measured arterio-venous increase of 20% [28], and obtain $\tau_r^{A\beta} = k_{A\beta}^{-1} = 97$ s. Inserting the critical times $\tau_c^{A\beta} = 8, 16$ or 40 s in Eq. (S32) yields respectively a three-, five- or tenfold arterio-venous increase of the total intravascular amyloid concentration.

References

- [1] A. R. Pries, T. W. Secomb, P. Gaehtgens, and J. Gross. “Blood flow in microvascular networks. Experiments and simulation.” In: *Circulation research* 67.4 (1990), pp. 826–834.
- [2] S. Lorthois, F. Cassot, and F. Lauwers. “Simulation study of brain blood flow regulation by intra-cortical arterioles in an anatomically accurate large human vascular network. Part II: Flow variations induced by global or localized modifications of arteriolar diameters”. In: *Neuroimage* 54.4 (2011), pp. 2840–2853.
- [3] J. C. Cruz-Hernández, O. Bracko, C. J. Kersbergen, V. Muse, M. Haft-Javaherian, M. Berg, L. Park, L. K. Vinarsik, I. Ivasyk, D. A. Rivera, et al. “Neutrophil adhesion in brain capillaries reduces cortical blood flow and impairs memory function in Alzheimer’s disease mouse models”. In: *Nature neuroscience* 22.3 (2019), pp. 413–420.
- [4] A. R. Pries, T. W. Secomb, T. Gessner, M. B. Sperandio, J. F. Gross, and P. Gaehtgens. “Resistance to blood flow in microvessels in vivo”. In: *Circulation Research* 75 (1994), pp. 904–914.
- [5] S. Lorthois. “Blood suspension in a network”. In: *Dynamics of Blood Cell Suspensions in Microflows*. Ed. by A. Viallat and M. Abkarian. 1st ed. Boca Raton: CRC Press, 2019, pp. 257–286.
- [6] A. R. Pries, B. Reglin, and T. W. Secomb. “Structural response of microcirculatory networks to changes in demand: information transfer by shear stress”. In: *American Journal of Physiology - Heart and Circulatory Physiology* 284.6 (2003), H2204–H2212.
- [7] B. C. Fry, J. Lee, N. P. Smith, and T. W. Secomb. “Estimation of Blood Flow Rates in Large Microvascular Networks”. In: *Microcirculation* 19 (2012), pp. 530–538.
- [8] E. Gutiérrez-Jiménez, C. Cai, I. K. Mikkelsen, P. M. Rasmussen, H. Angleys, M. Merrild, K. Mouridsen, S. N. Jespersen, J. Lee, N. K. Iversen, et al. “Effect of electrical forepaw stimulation on capillary transit-time heterogeneity (CTH)”. In: *Journal of Cerebral Blood Flow & Metabolism* 36.12 (2016), pp. 2072–2086.
- [9] K. E. Holter, B. Kehlet, A. Devor, T. J. Sejnowski, A. M. Dale, S. W. Omholt, O. P. Ottersen, E. A. Nagelhus, K.-A. Mardal, and K. H. Pettersen. “Interstitial solute transport in 3D reconstructed neuropil occurs by diffusion rather than bulk flow”. In: *Proceedings of the National Academy of Sciences* 114.37 (2017), pp. 9894–9899.
- [10] P. Kurowski, I. Ippolito, J. Hulin, J. Koplik, and E. Hinch. “Anomalous dispersion in a dipole flow geometry”. In: *Physics of Fluids* 6.1 (1994), pp. 108–117.
- [11] A. F. Smith, V. Doyeux, M. Berg, M. Peyrounette, M. Haft-Javaherian, A.-E. Larue, J. H. Slater, F. Lauwers, P. Blinder, P. Tsai, D. Kleinfeld, C. B. Schaffer, N. Nishimura, Y. Davit, and S. Lorthois. “Brain capillary networks across species: a few simple organizational requirements are sufficient to reproduce both structure and function”. In: *Frontiers in Physiology* 10 (2019), p. 233.
- [12] H. M. Duvernoy, S. Delon, and J. Vannson. “Cortical blood vessels of the human brain”. In: *Brain research bulletin* 7.5 (1981), pp. 519–579.
- [13] K. Alim, S. Parsa, D. A. Weitz, and M. P. Brenner. “Local pore size correlations determine flow distributions in porous media”. In: *Physical Review Letters* 119.14 (2017), p. 144501.
- [14] F. Schmid, P. S. Tsai, D. Kleinfeld, P. Jenny, and B. Weber. “Depth-dependent flow and pressure characteristics in cortical microvascular networks”. In: *PLoS computational biology* 13.2 (2017), e1005392.

- [15] M. Dentz, P. K. Kang, A. Comolli, T. Le Borgne, and D. R. Lester. “Continuous time random walks for the evolution of Lagrangian velocities”. In: *Physical Review Fluids* 1.7 (2016), p. 074004.
- [16] R. Metzler and J. Klafter. “The random walk’s guide to anomalous diffusion: a fractional dynamics approach”. In: *Physics reports* 339.1 (2000), pp. 1–77.
- [17] P. K. Kang, M. Dentz, T. Le Borgne, and R. Juanes. “Spatial Markov model of anomalous transport through random lattice networks”. In: *Physical review letters* 107.18 (2011), p. 180602.
- [18] P. De Anna, T. Le Borgne, M. Dentz, A. M. Tartakovsky, D. Bolster, and P. Davy. “Flow intermittency, dispersion, and correlated continuous time random walks in porous media”. In: *Physical Review Letters* 110.18 (2013), p. 184502.
- [19] S. N. Jespersen and L. Østergaard. “The roles of cerebral blood flow, capillary transit time heterogeneity, and oxygen tension in brain oxygenation and metabolism”. In: *Journal of Cerebral Blood Flow & Metabolism* 32.2 (2012), pp. 264–277.
- [20] E. Gutiérrez-Jiménez, C. Cai, I. K. Mikkelsen, P. M. Rasmussen, H. Angleys, M. Merrild, K. Mouridsen, S. N. Jespersen, J. Lee, N. K. Iversen, S. Sakadžić, and L. Østergaard. “Effect of electrical forepaw stimulation on capillary transit-time heterogeneity (CTH)”. In: *Journal of Cerebral Blood Flow & Metabolism* 36.12 (2016), pp. 2072–2086.
- [21] C. W. Merkle and V. J. Srinivasan. “Laminar microvascular transit time distribution in the mouse somatosensory cortex revealed by Dynamic Contrast Optical Coherence Tomography”. In: *NeuroImage* 125 (2016), pp. 350–362.
- [22] P. S. Tsai, J. P. Kaufhold, P. Blinder, B. Friedman, P. J. Drew, H. J. Karten, P. D. Lyden, and D. Kleinfeld. “Correlations of Neuronal and Microvascular Densities in Murine Cortex Revealed by Direct Counting and Colocalization of Nuclei and Vessels”. In: *Journal of Neuroscience* 29.46 (2009), pp. 14553–14570.
- [23] P. Blinder, P. S. Tsai, J. P. Kaufhold, P. M. Knutsen, H. Suhl, and D. Kleinfeld. “The cortical angiome: an interconnected vascular network with noncolumnar patterns of blood flow”. In: *Nature Neuroscience* 16.7 (2013), pp. 889–897.
- [24] N. Kutuzov, H. Flyvbjerg, and M. Lauritzen. “Contributions of the glycocalyx, endothelium, and extravascular compartment to the blood-brain barrier”. In: *Proceedings of the National Academy of Sciences* 115.40 (2018), E9429–E9438.
- [25] K. F. Roberts, D. L. Elbert, T. P. Kasten, B. W. Patterson, W. C. Sigurdson, R. E. Connors, V. Ovod, L. Y. Munsell, K. G. Mawuenyega, M. M. Miller-Thomas, C. J. Moran, D. T. Cross, C. P. Derdeyn, and R. J. Bateman. “Amyloid- β efflux from the central nervous system into the plasma: Brain Efflux of Amyloid- β ”. In: *Annals of Neurology* 76.6 (2014), pp. 837–844.
- [26] R. Potter, B. W. Patterson, D. L. Elbert, V. Ovod, T. Kasten, W. Sigurdson, K. Mawuenyega, T. Blazey, A. Goate, R. Chott, K. E. Yarasheski, D. M. Holtzman, J. C. Morris, T. L. S. Benzinger, and R. J. Bateman. “Increased in Vivo Amyloid- β Production, Exchange, and Loss in Presenilin Mutation Carriers”. In: *Science Translational Medicine* 5.189 (2013), 189ra77–189ra77.
- [27] M. Shibata, S. Yamada, S. R. Kumar, M. Calero, J. Bading, B. Frangione, D. M. Holtzman, C. A. Miller, D. K. Strickland, J. Ghiso, and B. V. Zlokovic. “Clearance of Alzheimer’s amyloid- β 1-40 peptide from brain by LDL receptor-related protein-1 at the blood-brain barrier”. In: *Journal of Clinical Investigation* 106.12 (2000), pp. 1489–1499.

- [28] Y. Xiang, X.-L. Bu, Y.-H. Liu, C. Zhu, L.-L. Shen, S.-S. Jiao, X.-Y. Zhu, B. Giunta, J. Tan, W.-H. Song, H.-D. Zhou, X.-F. Zhou, and Y.-J. Wang. “Physiological amyloid-beta clearance in the periphery and its therapeutic potential for Alzheimer’s disease”. In: *Acta Neuropathologica* 130.4 (2015), pp. 487–499.

2.2 Conclusion and perspectives

In this chapter, we have shown that the brain micro-vascular structure induces a blood flow organization akin to dipole flow on random networks. Such an organization notably induces broad blood flow distributions in the shape of Cauchy distributions. Both the dipole and disordered contributions to flow organization are found to induce anomalous transport properties at the scale of the network. These anomalous transport properties are driven by broadly distributed trajectory lengths of Lagrangian particles within the micro-vasculature and broadly distributed vessel transit times, respectively. This results in the emergence of a large dispersion of Lagrangian particle travel times within the micro-vascular networks on about four decades. The long time asymptotic regime of travel time distribution shows notably a stable power law decay with characteristic scaling exponent -3 . Designing a novel semi-analytical model for micro-circulatory transport, we have been able to capture the transport dynamics in brain micro-vascular networks at coarse-grained scale using a Continuous Time Random Walk approach. In agreement with our simulations, this model notably predicts the evolution of the size of areas with critical concentrations in amyloid and oxygen under hypoperfusion. These results offer a novel quantitative approach for predicting the impact of cerebral blood flow decrease on amyloid accumulation in Alzheimer's disease. Moreover, we have demonstrated that such an accumulation is simultaneous to the increase of the size of regions with a critically low oxygen concentration. This novel approach emphasizes the underestimation of transport heterogeneities by former micro-circulation models and, consequently, the underestimation of the impact of such heterogeneities on brain metabolism in healthy and unhealthy brain micro-vascular networks [20, 44, 46]. In that extent, our transport model supports the idea of an early triggering of a positive feedback loop linking the decrease of the cerebral blood flow to amyloid accumulation and to a decrease of metabolic activity in brain. However, in the light of this work, several questions remain open and will necessitate further investigations.

The first question is undoubtedly the impact of considering larger micro-vascular networks. In this work, we have studied the blood flow organization and transport properties in a 1 mm^3 volume of cortex. This change in network size is not expected to impact the observed scaling laws as we have shown that they derive directly from the network structure. However it could impact some of the model parameters. Indeed, we expect a depth increase to modify the parameters affected by boundary effects, namely Q_c , L_c and potentially L^* . Conversely, larger lateral extension would have only little impact on the transport properties because of the screening of further arterioles and venules by neighbouring ones. Then, it would be essential for the improvement of model accuracy to confront our actual parametrization to statistics obtained on larger micro-vascular network data sets.

The second question that arises is the question of the consistency of our description in the case of drastic changes in the conductance homogeneity of the capillary bed. We have shown in this chapter that occlusions of the micro-vascular networks do not significantly impact the scaling laws describing blood flow and transport properties. This stability of the description relies on the fact that even if some vessels are missing, the rest of micro-vasculature remains unchanged. However, in the case of Alzheimer's disease, an other component of cerebral blood flow decrease which has not been taken into account here is the shrinkage of capillary vessels [11, 14–17, 20]. Conversely, during brain activation, capillary vessels dilate but it is unclear if they all dilate the same way, or dilate at all, in brain tissue volumes corresponding to this study [11, 14]. Then, the question of capillary heterogeneity potentially induced by the two above mechanisms should be addressed as well experimentally as theoretically. We expect that an increase of the heterogeneity

of the capillary diameters should induce an increase of the vessel fraction in the low flow regime, modifying the observed scaling laws, specially the plateau in the flow distribution and consequently the asymptotic scaling of the travel time distribution.

The third question concerns the accuracy of the reaction models that we have used to compute the evolution of the regions with critical concentrations of amyloid and oxygen. Indeed, the metabolic bio-chemical reactions leading to amyloid production and to oxygen consumption are more complex than the ones we have used in this chapter (see e.g. [120] for amyloid). In the particular case of oxygen for instance, on one hand, we have considered an equilibrium between tissue and vessel oxygen concentrations and, on the other hand, we have disregarded the kinetics of desorption of oxygen from the Red Blood Cells (RBCs), which is well known to be non-linear [121]. The desorption of oxygen is potentially an important feature in its supply to brain tissues as RBCs act like tanks releasing oxygen all along their journey within the micro-vasculature. Neglecting desorption kinetics and assuming equilibrium of concentrations between blood and tissue can consequently lead to inaccurate predictions of the distribution of oxygen within the micro-vasculature. Then, an improvement of our transport model would be to couple transport to appropriate reaction kinetics in order to accurately predict the supply of oxygen or amyloid across the micro-vasculature. This can be done both numerically and theoretically, thanks to the CTRW framework. Hence, it could be interesting to compare simulations and model predictions to highly-resolved experimental measures of intra-vascular oxygen and amyloid concentrations for instance. Some measures of this type already exist for oxygen [10] but not for amyloid. The ultimate goal would be to introduce brain metabolic kinetics in the reactive transport model. Doing this, we could avoid the assumption of fixed chemical specie concentrations in brain tissues allowing to access to a higher level of generality.

Finally, the question of the spatial distribution of the chemical specie concentrations is still open with at least two potential implications. On one hand, brain tissues integrates the contributions of few neighbouring vessels. The local tissue concentration is then a local spatial average of the micro-vascular concentrations. As a consequence, it could be useful to study concentration spatial correlations in order to perform accurate averages. This will allow to have a better evaluation of the impact of micro-vascular critically low concentrations on surrounding tissues. On the other hand, occlusions or vessel shrinkage, as key features of Alzheimer's disease, can induce important local flow fluctuations (see notably Chapter 4 for occlusions) and consequently can also lead to large fluctuations of the uptake of chemical species. Within the CTRW approach that we have developed in this chapter, we do not have any information on the spatial locations of the concentrations. Then, we can only access to the impact of first order perturbations of the flow, i.e. the global reduction of the blood flow. Introducing a spatial dependency can allow to access to the local modifications of the chemical specie concentrations induced by micro-vascular occlusions. Practically, it is possible to introduce a spatial dependency within the CTRW framework thanks to a geometrical characterization of micro-vascular networks. Doing this, we would access to a better picture of chemical specie concentrations in brain tissues and of their modification by micro-vascular occlusions. This would allow to progress in understanding the link between micro-vascular occlusions and cognitive decline in particular in the context of Alzheimer's disease.

Chapter 3

Random network flow statistics model

In the previous chapter, we have shown that the cerebral blood flow organization at the micro-vascular level is statistically similar to a flow structured by dipolar injections on a random network. This organization is associated to a flow rate distribution exhibiting two regimes separated by a characteristic flow value, Q_c . Below Q_c , the flow rate distribution is uniform whereas, above Q_c , the flow rate distribution exhibits a large power law tail. Hence, Q_c delimits the domains of predominance of dipole and random flows. In other words, network randomness perturbs the structured dipole flow organization until the signature of the dipole flow vanishes due to finite size effects. The low flow regime is spatially located in the disordered part of the micro-vasculature: the capillary bed. As the dipole structure has been extensively studied in the previous chapter, we focus here on characterizing the statistics of the random flow emerging from the topology-driven disorder in the capillary bed.

3.1 Preliminary observation

Predicting flow statistics from the properties of a porous medium is a central question of porous media physics. Hence, an important part of the literature, which historically mainly concerns geological porous media, focuses on the impact of pore size heterogeneity on flow properties [82, 98, 102]. The focus on pore size heterogeneity makes sense for geological porous media as they display large pore size variability but it appears to be less relevant for biological porous media where the biological feedbacks impose much more regularity on the pore sizes [122], and this is particularly true for capillary networks. In this system, flow variability does not arise from pore size heterogeneity but from the random connection of capillaries. We call here such type of flows topology-driven random flows.

As discussed in the previous chapter, one of the key properties that emerges from topology-driven random flows is the uniform distribution of flow at low values. This was observed in [98] in porous medium of moderate pore size heterogeneity. In this article, this plateau has been shown to be part of a stretched exponential distribution. This result has been derived from the observation of a Gaussian distribution of velocities induced by the moderate level of pore size heterogeneities. In topology-driven flows, the velocity distribution is similar to the flow distribution because of low variability of pore sizes. Hence, the explanation of the emergence of such plateau in topology-driven flows should be found elsewhere. More recently, an adaptation of a statistical mechanics model, the q-model, has been proposed in [82] to predict the high flow regime of the flow distribution in porous media of highly heterogeneous conductances. The latter

study provides an analytical description of the flow distribution at high values in the shape of an exponential distribution. Conceptually, the q-model is based on the idea that the statistics of a conservative quantity submitted to consecutive random additions and divisions converge during this process towards a stable distribution under certain conditions. The use of this model in the context of flows in random porous media is motivated by the local divisions and sums of the flow at the pore intersections. The question of the link between the pore size distribution and the emerging power law distribution of flows at low values in porous media of highly heterogeneous conductances is still open. This issue is currently the subject of a collaboration that we have developed with Marco Dentz but this lies beyond the scope of this chapter. Here, as stated above, we focus on designing a statistical framework able to predict accurately the flow distribution in topology-driven random flows which are relevant in micro-vascular networks.

To do so, we first analyze the flow statistics obtained for a 3D bio-mimetic capillary bed (~ 15.000 edges) for which a uniform pressure boundary condition is imposed at the top and at the bottom in order to focus on avoiding any deterministic large scale structuration of the flow. This network is obtained from a raw network, product of a 3D Voronoi tessalation of the space, designed to satisfy the topological and geometrical properties of capillary networks. Hence, this so-constructed bio-mimetic capillary bed presents on a topological point of view, for instance, the same 3-connectivity and loop distribution and, on a geometrical point of view, the same distributions of diameter and length of vessels than real capillary beds [8]. This results in a disordered regular network with connectivity 3 and roughly homogeneous conductances within which an almost stratified pressure field settles with the prescribed boundary conditions (Fig. 3.1).

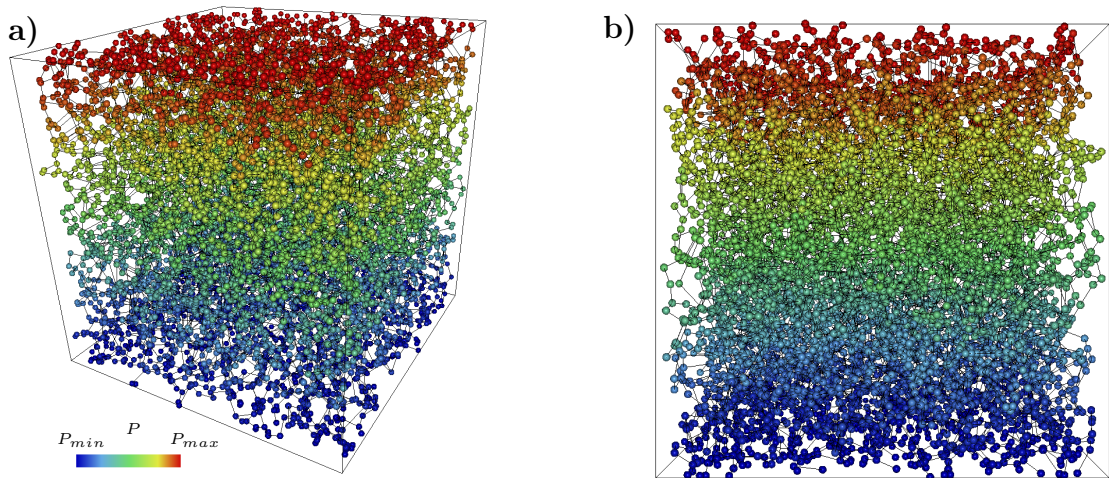


Figure 3.1: **Uniform pressure boundary condition imposed at the top and at the bottom results in an approached stratification of the pressure field at the network scale. a-b)** Snapshots of the pressure field in a bio-mimetic capillary network with linear color scale.

The apparent structured organization of the pressure field hides the high level of flow disorder which results from it (Fig. 3.2a). As expected from the results of Chapter 2, the flow rate distribution associated to network edges, p_Q , exhibits a large plateau at low values (Fig. 3.2b). This plateau is ended by a sharp cut-off in the vicinity of the mean value. Strikingly, even if the flow rate distribution is close to an exponential, it shows less probability to obtain both small and large values than expected by this classical solution for flow statistics in random porous media. Our objective in this chapter is to explain the narrowing of the flow distribution compared to the

q-model classical solutions.

In this chapter, we first present key elements of the q-model in its original mean-field formulation. Then, we discuss the use of this model in the context of the prediction of flow statistics in random porous media. Finally, we discuss the limitations of the mean-field formulation of the q-model for the considered system due to the presence of local anti-correlations in the flow. We show that these anti-correlations are induced by the limitations of homogeneous networks to dissipate the whole local pressure drops associated to the largest flows predicted by the mean-field formulation of the q-model. Along this chapter, as there is no relevance in considering absolute values, quantities might be rescaled by their corresponding mean value and shorthanded with tilde sat on top.

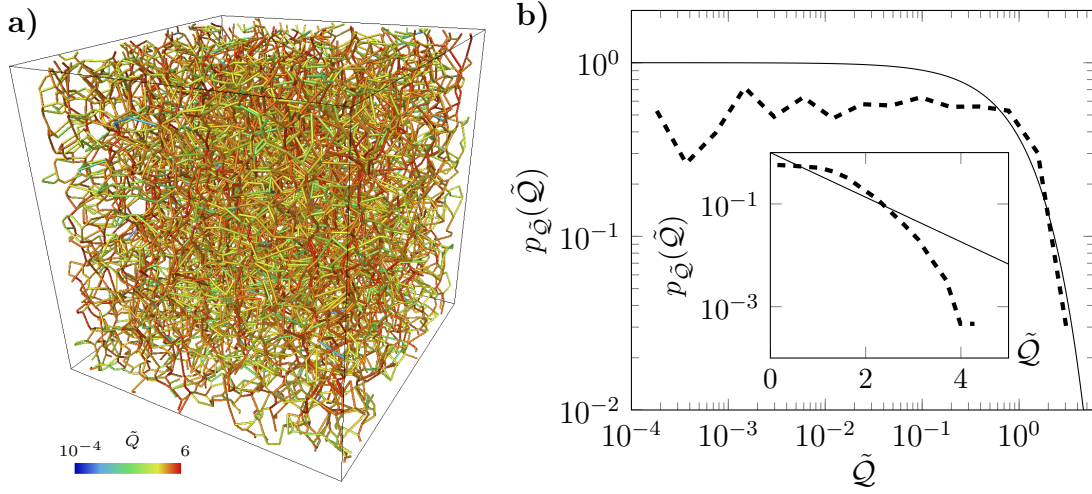


Figure 3.2: **Exponential-like flow distribution emerges from network disorder.** **a)** Snapshot of the flow distribution in a bio-mimetic micro-vascular network with logarithmic color scale. **b)** Associated probability Density Function of flow rates (dashed line) and exponential distribution (full line). Main panel: log-log scale. Inset: semi-log scale.

3.2 The mean-field q-model: theory and simulations

The q-model was primarily designed in its mean-field formulation to quantify the force fluctuations in random bead packs through an analytically solvable framework [79, 97]. Furthermore, the generality of its constitutive elements makes it a particularly versatile model with a wide range of potential applications. We first recall these constitutive elements in the context of force fluctuations in bead packs. We will then detail its formulation in the context of flow in porous media.

Let a disordered pack of unit mass beads. This pack can be subdivided into an extensive number of superimposed bead layers (Fig. 3.3 shows an exemple of a such decomposition in layers). Each bead in the D layer bears a random fraction of the weight of the beads located in the above layers. This weight fraction is transfered to a given bead by the N beads located above and with which it is in contact. Hence, considering that each bead supports its own weight in addition to the weight transfered by the above beads, the total weight supported by the i bead in the D layer,

$w_i(D)$, can be expressed as:

$$w_i(D) = \sum_{j=1}^N q_{ij} w_j(D-1) + 1 \quad (3.1)$$

where the q_{ij} 's are random variables belonging to $[0; 1]$ and distributed according to a *pdf* η . They represent the fraction of weight supported by the j bead transferred to i . In order to get rid of the drift of the weight distribution with D induced by the internal mass of each bead, the normalized weight is defined as $v_i(D) = w_i(D)/D$.

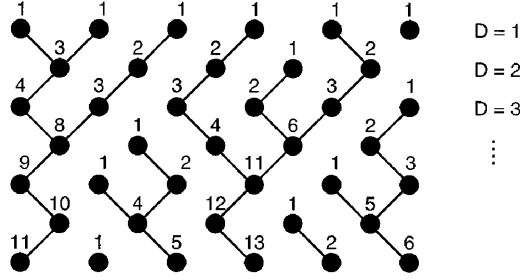


Figure 3.3: **Random bead packs can be decomposed into superimposed bead layers.** Sketch of weight transmission into a random bead packs in the particular case for which a bead transfers the weight to only one bead located in the below layer. Layers are indexed by D . The numbers above each bead highlight its overall supported weight, $w_i(D)$ (extracted from [79]).

At each node, the supported weight in a given layer is the sum of the product of the v and q random variable realizations in the previous layer. Thanks to the observed stability of the weight distribution and ignoring weight correlations within layers, it is possible to write a recursive mean-field equation on the distribution of the normalized weights on nodes. Hence, the *pdf* of v can be expressed in terms of a N -convolution product of the vq *pdf*, which gives at large D :

$$P(v) = \prod_{j=1}^N \int_0^1 dq_j \eta(q_j) \int_0^\infty dv_j P(v_j) \delta \left(\sum_{j=1}^N v_j q_j - v \right) \quad (3.2)$$

The parametrization of the η distribution is a critical step in the analytical treatment of Eq. (3.2) as this distribution encodes the characteristics of the weight propagation. In this section, we focus on the case of uniformly distributed weight fractions: all q 's random variables sample uniformly the interval $[0, 1]$. We will see in the next sections that the uniform distribution suits well the characteristics of flow fraction propagation in micro-vascular networks. We stress here that the weight fractions are not totally independent as they relate through the constraint $\sum_i^N q_i = 1$ (more precisely, we can consider $N-1$ independent variables and the N^{th} conditioned by $q_N = 1 - \sum_i^{N-1} q_i$ if $\sum_i^{N-1} q_i \leq 1$). With those prescriptions, the η distribution is found not to be uniform for general N (see [79] for the demonstration and Fig. 3.4 for plots of η for some values of N):

$$\eta(q) = (N-1)(1-q)^{N-2} \quad (3.3)$$

With this parametrization of the η distribution, Eq. (3.2) is analytically tractable. Going into Laplace space, in which convolution products turn to classical products, this becomes:

$$\tilde{P}(s) = \left[\int_0^1 dq \eta(q) \tilde{P}(sq) \right]^N \quad (3.4)$$

where \tilde{P} is the Laplace transform of P .

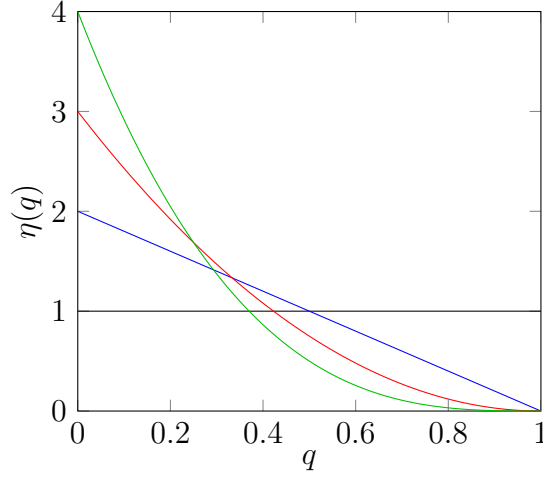


Figure 3.4: **Conservation equation implies a N -dependency in the distribution of propagated weight fractions.** Distribution of weight fractions $\eta(q)$ for $N = 2$ (black), 3 (blue), 4 (red) and 5 (green).

We first present the computation of P in the case of $N = 2$. In addition to be the simplest case and consequently gives an idea of the way to handle the general case, it corresponds closely to the topology of the flow organization in micro-vascular networks that we will discuss in more details in the following section. In the $N = 2$ case, $\eta(q) = 1$ and Eq. (3.2) then becomes:

$$\tilde{P}(s) = \left[\int_0^1 dq \tilde{P}(sq) \right]^2 \quad (3.5)$$

Introducing the Laplace transform of the distribution of transfered weights, $\tilde{V} = \tilde{P}^{1/2}$, and performing a change of variable $u = sq$, the precedent equation becomes:

$$s\tilde{V}(s) = \int_0^s du \tilde{V}^2(u) \quad (3.6)$$

Differentiating with respect to s :

$$s \frac{d\tilde{V}(s)}{ds} + \tilde{V}(s) = \tilde{V}^2(s) \quad (3.7)$$

This differential equation has for solution $\tilde{V}(s) = 1/(1-Cs)$ and consequently $\tilde{P}(s) = 1/(1-Cs)^2$. By definition of the mean rescaled weight, which is equal to the mass of a bead, $\int_0^\infty dv v P(v) = d\tilde{P}(s)/ds|_{s=0} = 1$, the constant C is found equal to $-1/2$. Inverting the Laplace transformation, the distribution of weights supported by the beads is:

$$P(v) = 4ve^{-2v} \quad (3.8)$$

and the distribution of weights transfered between layers is:

$$V(v) = 2e^{-2v} \quad (3.9)$$

Trivially, we recover the expected result that the mean weight supported by beads differs by a factor $N = 2$ to the mean weight transferred between layers.

The overall approach presented above can be generalized for arbitrary values of N introducing this time $\tilde{V} = \tilde{P}^{1/N}$ and considering the general form of the η distribution of Eq. (3.3). Furthermore, the generalized version of Eq. (3.6) should be differentiated $N - 1$ times. We will not present the details of the computation in the general case as it is particularly cumbersome but to only recall its results. Hence, the weight distribution supported by beads in the general case is a gamma distribution:

$$P(v) = \frac{N^N}{(N-1)!} v^{N-1} e^{-Nv} \quad (3.10)$$

and the distribution of propagated weights an exponential distribution:

$$V(v) = N e^{-Nv} \quad (3.11)$$

In the following, we present a simple simulation scheme capturing the essence of the q-model. The interest of these simulations is to allow to investigate the effects of the model constitutive elements and in particular the η distribution. Considering a pool of $N_p = 5.000$ particles of unit mass, we iteratively perform successive random fragmentations and dissociations of these particles. As long as the number of fragmented particles is equal to the number of particles that have to be aggregated the distribution of particle mass converges toward a stable distribution. Furthermore, by construction of the algorithm, the process is purely without memory and the particle shuffle ideal, which suit perfectly to the mean-field framework.

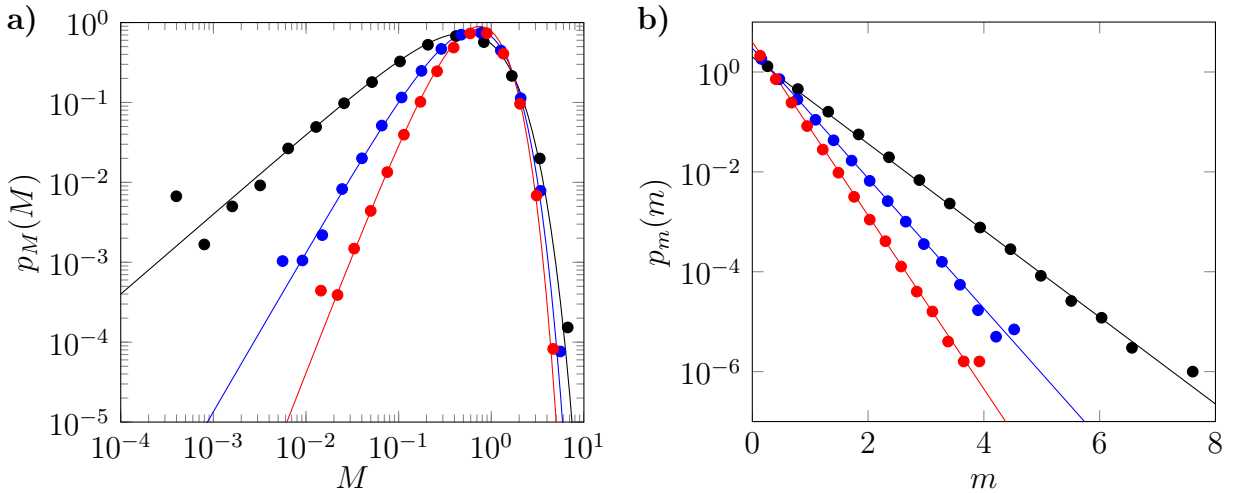


Figure 3.5: **Mass distributions of particles emerging from the symmetrical random aggregation/fragmentation process are well predicted by the mean-field q-model.** **a)** Mass distribution of aggregated particles (dots) and associated q-model mean-field predictions (full lines) of Eq. (3.10). **b)** Mass distribution of fragmented particles (dots) and associated q-model mean-field predictions (full lines) of Eq. (3.11). For both panels, simulations are performed with $N = 2$ (black), $N = 3$ (blue) and $N = 4$ (red).

This aggregation/fragmentation process is described by a mass conservation equation:

$$M_i(D) = \sum_{j=1}^N q_{ij} M_{ij}(D-1), \quad (3.12)$$

where $M_i(D)$ is the mass of the i^{th} particle at the D^{th} iteration of the process and q_{ij} the mass fraction coming from the fragmentation of the j^{th} particle in the precedent iteration, and a local recursive equation on the mass distribution, denoted p_M :

$$p_M(M) = \prod_{j=1}^N \int_0^1 dq_j \eta(q_j) \int_0^\infty dM_j p_M(M_j) \delta \left(\sum_{j=1}^N M_j q_j - M \right) \quad (3.13)$$

It is clear from the similar structure of, on one hand, Eq. (3.1) and Eq. (3.12) and, on the other hand, Eq. (3.2) and Eq. (3.13) that the two processes are conceptually equivalent in the large D limit. In Fig. 3.5, introducing the mass distribution of fragmented particles, p_m , we verify the agreement between the results of simulations performed for varying N with mass fractions uniformly distributed and the predictions of the q-model for p_M (Eq. (3.10)) and p_m (Eq. (3.11)).

In this section, we have recalled the principal theoretical aspects of the mean-field formulation of the q-model. We have further introduced a simple numerical scheme capturing the essence of this model. Together, these theoretical and numerical tools are key elements necessary to the analysis and the prediction of the flow statistics into disordered porous media as discussed in the following.

3.3 q-model and flow organization

In the previous section, through the introduction of the symmetric random aggregation/fragmentation process, we have shown that the q-model framework was relevant to model other physical processes that force fluctuations into random bead packs. This correspondance in the analytical treatment of those two processes is the result of the generality of the model constitutive elements, i.e. a conservation equation (Eq. (3.1)) and a local recursive relation on the *pdf*, made possible by its stability (Eq. (3.2)). In this section, we discuss how these concepts apply in the context of flow into disordered porous media. In the following, we review the limitations of this analogy in the particular case of our 3-connected biomimetic microvascular network.

Flows into disordered porous media are similar to the symmetric aggregation/fragmentation process presented in the previous section. However, they differ from the force fluctuations into random bead packs by the absence of of source term due to the addition of individual bead mass in the conservation equation. This conceptual difference induces two consequences. First, layer (or more appropriated here, depth) dependency becomes irrelevant and the large D limit useless. As a consequence, we discard it in the following. Secondly, associated to the hypothesis of stability of the flow distribution, this constrains the topological configurations of the flow as explained in the following. If the flow distribution is stable, it notably conserves its mean and the total amount of flow passing from one layer to an other should be exactly conserved. Furthermore, if the total and mean flows are conserved, this implies that the number of edges should be conserved with the depth. The conservation of the higher moments of the *pdf* imposes, as for them, that only a small variety of local topological configurations can emerge in order to satisfy, at least statistically, the stability hypothesis. In other words, even if local topological trees may emerge from the spatial organization of the flow, its statistically representative configurations turn out to be antisymmetrical (Fig. 3.6).

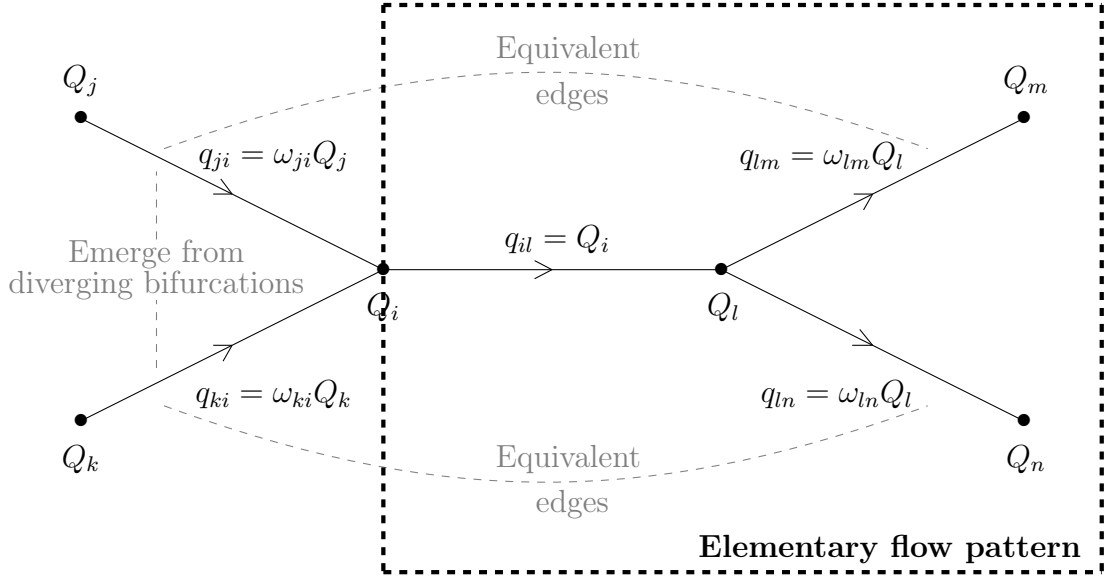


Figure 3.6: **Conservation of the flow and stability of the flow distribution constrains flow local topological configuration.** Sketch of the statistically representative flow configuration in 3-connected random networks.

Contrary to force distribution in random bead packs where the weight propagation is less relevant than the weight supported by each bead in itself, in flow through porous media, the flow rate *pdf* at nodes is *a priori* less important as they have marginal impact on large scale transport properties, and even more within pore network modelling frameworks. Consequently, the flow rate *pdf* is commonly measured within pore throats, i.e. on the edges of the equivalent pore network.

In the context of flow in random networks, Eq. (3.1) now reads:

$$Q_i = \sum_{j=1}^N q_{ij} \quad (3.14)$$

where the Q_i is the flow at node i and $q_{ij} = \omega_{ij}Q_j$ is the fraction of flow coming from node j to i , or in another words the flow associated to the edge ij and Eq. (3.2) becomes:

$$p_Q(Q) = \prod_{j=1}^N \int_0^1 d\omega_j \eta_\omega(\omega_j) \int_0^\infty dQ_j p_Q(Q_j) \delta \left(\sum_{j=1}^N \omega_j Q_j - Q \right) \quad (3.15)$$

Assuming an η_ω distribution according to Eq. (3.3), the flow rate *pdf* on nodes behaves like:

$$p_Q(Q) = \frac{N^N}{(N-1)!} Q^{N-1} e^{-NQ} \quad (3.16)$$

and the flow rate *pdf* on edges is expected to behave like:

$$p_q(q) = N e^{-Nq} \quad (3.17)$$

for which $\langle Q \rangle = 1$.

Eq. (3.17) demonstrates the emergence of the exponential-like flow distributions in random networks as observed in Fig. 3.2. Moreover, the constraint of antisymmetry imposed on local

flow configurations leads to an alternation of converging and diverging local topological structures for a 3-regular flow network. Consequently, as two edges emanating for divergent bifurcations give rise to a single edge before dividing again, at the network scale, about one third of edges transmits in totality the amount of flow coming from its upstream node (Fig. 3.6). These edges might be understood as nodes within the q-model framework and consequently their associated flows are expected to be distributed according to a gamma-like *pdf* as verified in Fig. 3.7. As a consequence, the flow distribution on all edges of the network, p_Q , has to be expressed in terms of the flow distribution on edges, p_q , and on nodes, p_Q , as:

$$p_Q(Q) \approx \frac{2}{3}p_q(q) + \frac{1}{3}p_Q(Q) \quad (3.18)$$

In the following, we will refer to these particular edges which present a gamma-like distribution of flows as “node edges”, by opposition to physical edges that can be mapped by q-model edges. The latter are simply called edges. Moreover, Fig. 3.7 highlights that, similarly to p_Q , the p_q *pdf* is narrower than the analytical prediction of Eq. (3.16).

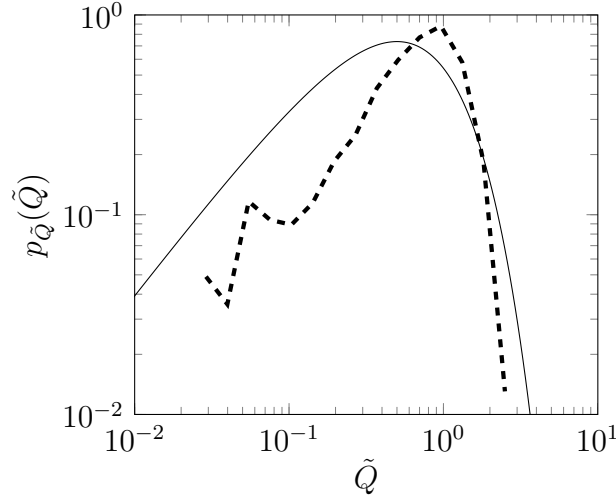


Figure 3.7: **Flow statistics for “node edges” exhibit a gamma-like distribution, the mean-field q-model with uniformly distributed flow fractions fails to predict them accurately.** Flow rate *pdf* for “node edges” (dashed line) and plot of Eq. (3.16) with $N = 2$ (full line).

We formulate two hypotheses to explain the observed deviation of flow distributions on nodes and on edges to Eq. (3.16) and Eq. (3.17):

- the distribution η_ω is not uniform.
- the correlations that are ignored within the mean-field formulation of the q-model have non-negligible impact on the flow rate statistics.

We will now examine which of these two hypotheses is more likely to produce this deviation before addressing the issue of the physical mechanisms that underly the narrowing of the flow distributions.

To begin, we tackle the question of a potentially non-uniform η_ω distribution. As a consequence, η_ω is computed distinguishing edges to “node edges” in coherence with the above remark,

i.e. the values $\omega = 1$ induced by the 3-connected topology are not taken into account in the ω 's statistics. In Fig. 3.8a, we observe that η_ω slightly differs from a uniform distribution in two ways. On one hand, it displays a smooth peaked shape around $\omega = 0.5$. On the other hand, η_ω rapidly decreases in the vicinity of 0 and 1. As stated above, we first investigate the consequences of considering this distribution, instead of a uniform one, on the flow rate statistics. The physical interpretation of this deviation will be addressed later.

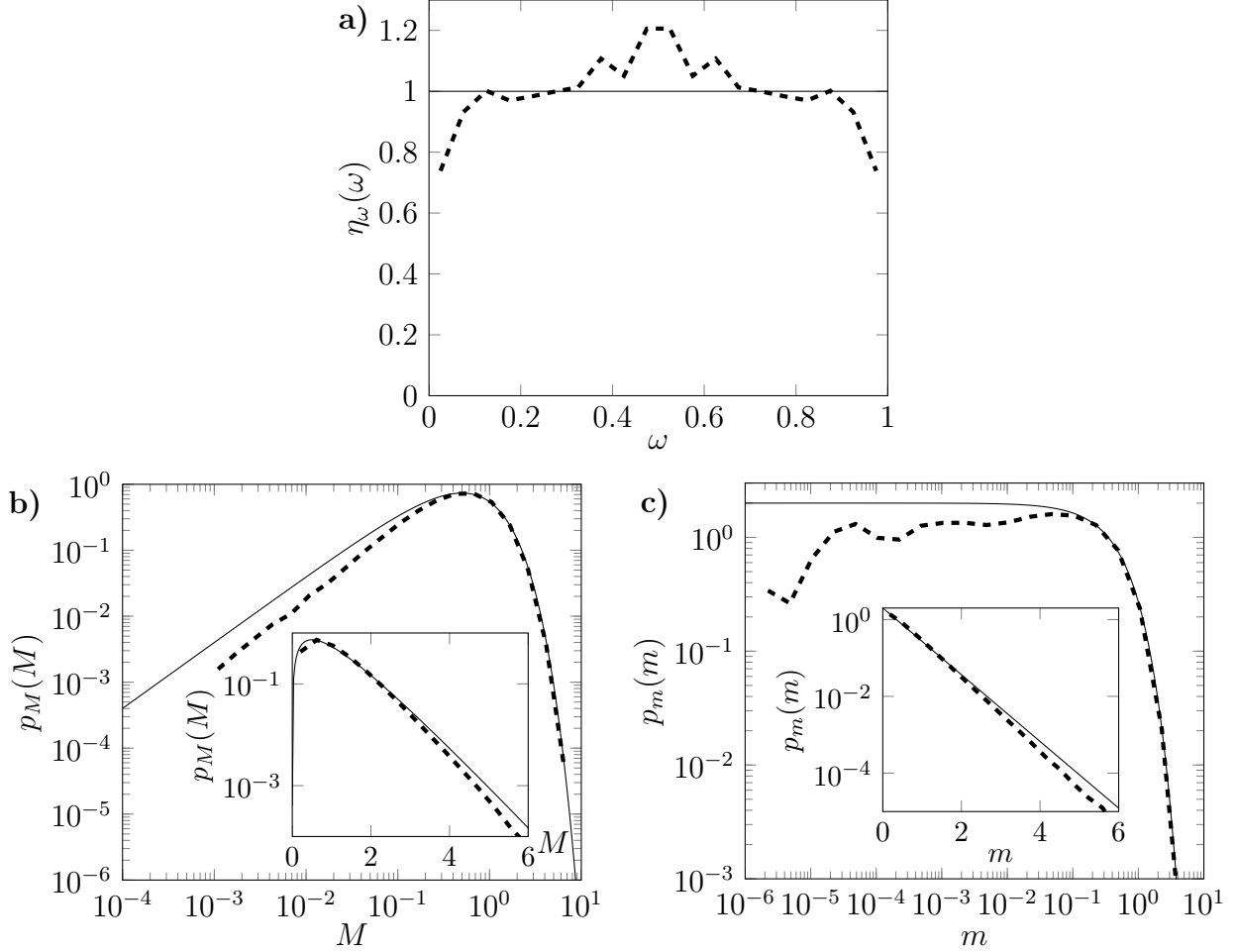


Figure 3.8: **The observed deviation to uniformity of the empirical η_ω distribution brings only minor corrections to the emerging mass (or flow) distributions.** **a)** Propagated flow fraction pdf, η_ω (dashed line) and uniform distribution (full line). **b)** Aggregated particle (or node) mass (or flow) distribution (dashed line) and plot of Eq. (3.16) (full line). Main panel: log-log scale. Inset: semi-log scale. **c)** Fractionned particle (or edge) mass (or flow) distribution (dashed line) and plot of Eq. (3.17) (full line). Main panel: log-log scale. Inset: semi-log scale.

In order to investigate the consequences of such deviation to uniformity of the η_ω distribution, we use the numerical scheme presented in the previous section. Hence, sampling the empirical η_ω distribution of Fig. 3.8a, we perform simulations of successive random fragmentations and aggregations of a pool of 5.000 particles of unit mass and compare the results of these simulations to the mean-field q-model predictions for a uniform η_ω (Fig. 3.8b and c). With the notations introduced in the previous section, the mass distributions of fractionned and aggregated particles, respectively p_m and p_M , are effectively impacted by the change in the η_ω distribution.

Nevertheless, this modification does not suffice in itself to explain the important narrowing of the flow distributions computed in the micro-vascular networks compared to the mean-field q-model predictions. This indicates that something more important is happening beyond mean-field as discussed in the following section.

3.4 Beyond the mean-field approximation

In this section, we investigate the limitations of the mean-field formulation and determine the physical mechanisms leading to it. We explore if correlations in the flow organization could explain the unexpected narrowness of p_Q (Fig. 3.2b) and p_Q (Fig. 3.7). Furthermore, we attempt to relate the emergence of these correlations to the physical properties of the medium. Doing so, we underline the importance of the distinction that we made between physical edges and q-model edges.

In the q-model, the mean-field approximation neglects the correlations that might exist between beads belonging to the same layer. In flow networks, these ignored correlations can take place between the flow fractions ω associated to the flows that sum at a given node and/or between the flows Q associated to the upstream nodes of this same node. As the impact of the non-uniformity of the η_ω distribution cannot explain on its own the observed deviation from Eq. (3.16) and Eq. (3.17), the question of the existence of correlations between, on one hand, the ω variables and, on the other, the Q variables is raised. In order to investigate those potential correlations, we split flow fractions and node flows into fifteen equiprobable classes $\mathcal{C}_i(\omega)$ and $\mathcal{C}_i(Q)$ of equal size and compute their joint probability matrices, or copula density functions [123], $p_{\mathcal{C}(\omega_2), \mathcal{C}(\omega_1)}$ and $p_{\mathcal{C}(Q_2), \mathcal{C}(Q_1)}$ respectively.

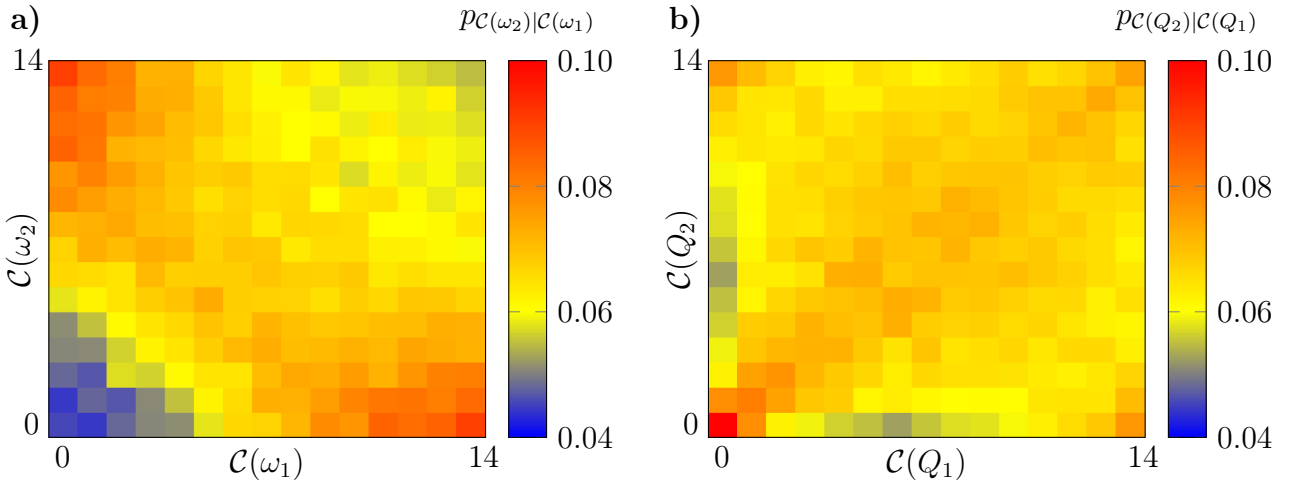


Figure 3.9: **Copula density function analysis highlights the emerging anti-correlations between flow fractions whereas node flows appear rather independent.** a) Flow fraction copula density function. b) Upstream node flow copula density function.

Copula density functions have been developed to study the correlations between random variables disregarding the marginal probability density function associated to each random variable [123]. Indeed, the classes composing the matrices are random variables with uniform marginal probability density functions by construction. Then, their joint probability is uniform for indepen-

dent random variables. Conversely, if the random variables are totally correlated, copula density function exhibits ones in the first diagonal and zeros elsewhere and if the random variables are totally anti-correlated, copula density function exhibits ones in the second diagonal and zeros elsewhere. The copula formalism has been used in a wide range of fields from quantitative finance [124] to hydrogeological transport [125–127].

In Fig. 3.9a, the flow fraction copula density function exhibits the highest probabilities in the vicinity of the second diagonal and is maximal in the bottom right-hand corner (and in top left-hand corner by symmetry of this matrix). Furthermore, the lowest probabilities are located in the bottom left-hand corner and in the top right-hand corner. This matrix structure characterizes the presence of anti-correlations between the ω variables. These anti-correlations highlight the tendency of the flow to sum small flows with large flows. In that extent, these anti-correlations are good candidates to explain the narrowing of the flow distributions. As for the upstream node flow copula density function, the conclusion is less clear. The copula density function appears rather uniform, a sign of the independence of the Q variables, however it seems to exist soft positive correlations specially for the lowest classes. Nevertheless, by comparison to the flow fraction copula density function, these correlations seem negligible. Furthermore, positive correlations would tend to increase the variability of the flow fluctuations. Then, the correlations between the Q variables cannot constitute a driver of the narrowing of the flow distributions. Hence, we disregard it in the following.

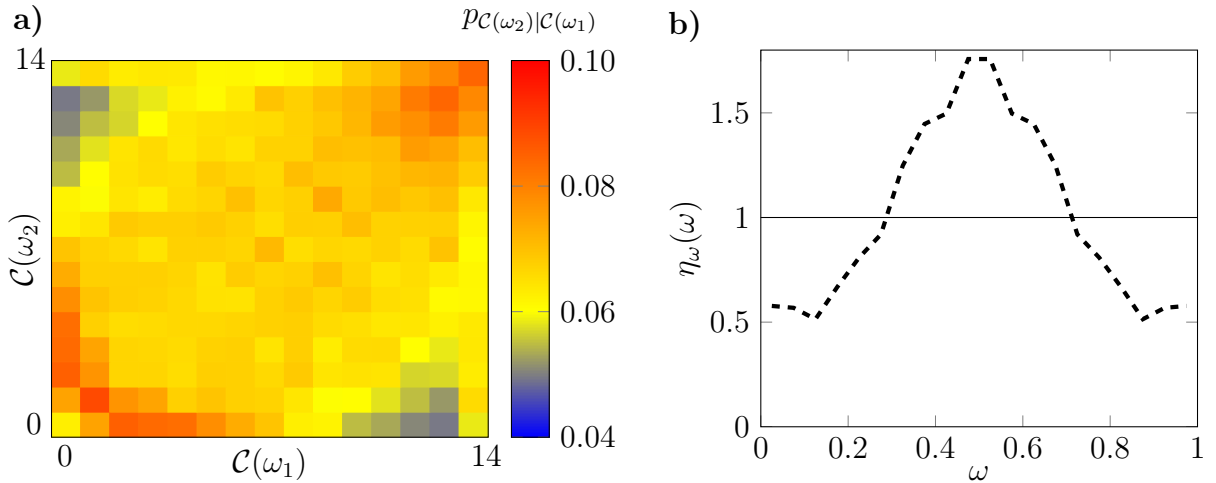


Figure 3.10: **Drastic increase of “node edge” conductance re-establishes quasi-independency between the ω variables and brings corrections to the flow fraction distribution.** a) Flow fraction copula density function. b) Flow fraction distribution (dashed line) and uniform distribution (full line).

The emergence of anti-correlations between the w random variables, associated to the approximate independancy of the Q variables, induces therefore anti-correlations between the q variables. The fact that such correlations are not observed in bead packs, and then commonly not taken into account into analytical computations, might be linked to the differences between both systems. The principal difference is a pressure difference at the boundaries of the random network for the flow to establish, whereas the weight propagating in the bead packs is the result of internal bead mass. The global pressure difference then strongly constrains the local pressure differences accross the network, i.e. the sum of the pressure drops along streamlines would need to

be equal to the global pressure difference, where the weight magnitudes can freely fluctuate. This constrain specially affects the high flow statistics. This mechanism can explain notably the sharp cut-off of the flow distributions (see e.g. Fig. 3.2b). This observation is even more relevant for what we called “node edges” whose flows are twice the order of magnitude of other edges but with comparable conductances, as discussed in the previous section. Furthermore, this explanation of the global pressure constraint is also compatible with the slight deviation from uniformity that we observed for the η_ω distribution (Fig. 3.8a). In order to respect the global constraint, downstream node flows can be forced to choose ω close to 1/2 rather than 1 (and 0 by symmetry) in order to minimize their local pressure difference in the case where the upstream node flow is high.

In order to check that the anti-correlations between added flow fractions result effectively from the limitations of the pressure dissipation along “node edges”, we increase the “node edge” diameter by a factor 5, leading to an increase of the conductance by a factor $5^4 = 625$, and recompute the flow. As the “node edge” conductance importantly increases, there is no longer theoretical limitations of their associated flow magnitude and the anti-correlations between the w variables vanish (Fig. 3.10a). However, the edge conductance is, as for it, unchanged and the limitations on largest edge flows, that we already noticed in Fig. 3.8a by a decay of the η_ω in the vicinity of 1 (and 0), considerably reinforce. Now, η_ω exhibits large deviations from uniformity in the shape of a concave distribution (Fig. 3.10b) highlighting the transfer of the pressure constraint to edges.

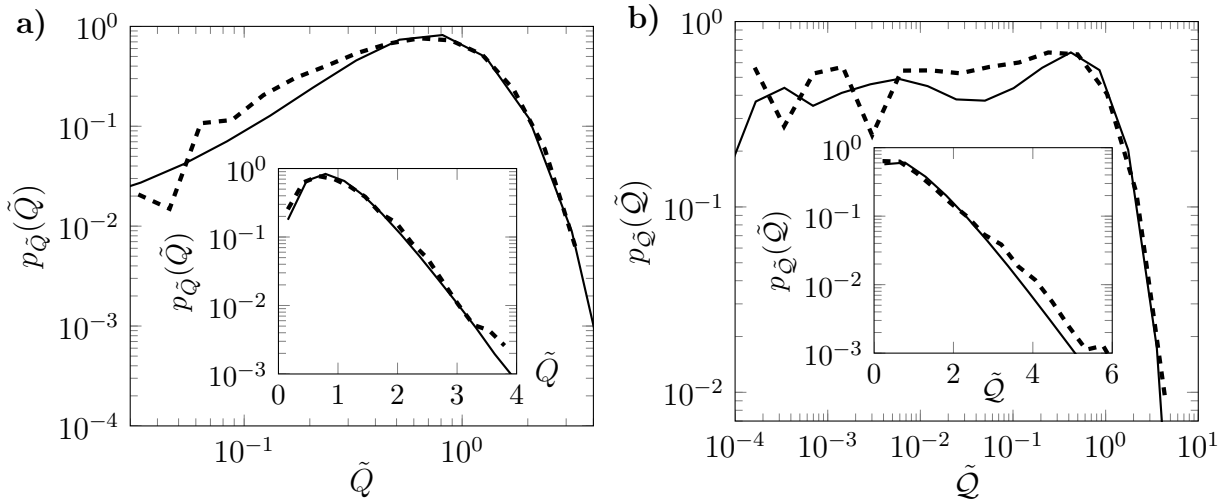


Figure 3.11: **Mean-field predictions accuracy is restored following w variable decorrelation.** **a)** Node flow distribution (dashed line) and mean-field predictions (full line). **b)** Physical edge distribution (dashed line) and mean-field predictions (full line). Main panels: log-log scale. Insets: semi-log scale. Flow fractions are sampled according to the empirical η_ω of Fig. 3.10

Finally, we verify that the accuracy of the mean-field formulation of the q-model is restored with the removal of the w anti-correlations. Doing this, we finish to demonstrate that the w anti-correlations are effectively the main driver of the mean-field fail in predicting accurately flow statistics in topology-driven random flows (Fig. 3.2b and Fig. 3.7). We then compute p_Q , the distribution of flow rates on all edges (edges and “node edges”) and p_q , the distribution of flow rates at nodes. We stress here that, because of the presence of the “node edges”, p_Q has to be expressed as $p_Q \approx 2p_q/3 + p_Q/3$ (Eq. (3.18)). In the same way as before, mean-field predictions are

obtained by simulating consecutive random aggregations and fragmentations accounting for the non-uniformity of the η_ω distribution of Fig. 3.10b. Once again, we use a pool of 5.000 particles of unit mass with mass fractions sampled according to the empirical η_ω distribution. The comparison between mean-field predictions and corresponding flow distributions is presented in Fig. 3.11 and highlights the restoration of the mean-field accuracy after ω variable decorrelation.

3.5 Conclusion and perspectives

In this chapter, we have investigated the emergence of exponential-like flow distributions in random networks through the q-model framework. This theory was first designed to predict force fluctuations in random bead packs. The use of this model to predict flow statistics in random networks is motivated by the very general constitutive elements of this model, i.e. a conservation equation, the *pdf* stability and a local recursive equation emerging from a random aggregation/fragmentation rule. However, we have shown in this section that the analogy between force fluctuations in bead packs and flows in random networks has some important limitations. First, the quantity of interest, in bead packs, is the weight supported by each bead, which focuses the study on the node of the equivalent force network. On the contrary, for flow networks, the quantity of interest is the physical edge flow statistics which can be distributed according to either q-model node or edge distributions. The second difference relies on the nature of the two systems. The imposed pressure conditions at the boundaries of the flow network constrain locally the flow propagation leading to local flow anti-correlations. These anti-correlations are responsible for the limitations of the q-model mean-field formulation to predict accurately the flow statistics in homogeneous random networks. This results in a decrease of the flow heterogeneities compared to the exponential solution of the mean-field q-model.

The presence of anti-correlations between the flow fraction random variables consists in a interesting source of complexity as they are usually considered independent in the litterature. As a consequence, this study offers new perspectives for future research. On a theoretical point of view, the integration of w anti-correlations consists in an interesting computational challenge as well for the derivation of the general q-model solutions as for the computation of possible new (anti-) correlations in the flow structure that can emerge from them [128]. Furthermore, the response of the w anti-correlations to modification of the network topology (disorder and connectivity) could be an other topic of interest. In particular, it is expected that there exists an upper connectivity above which mean-field predictions become again exact. Finally, for transport in (biological) porous media, the corrections that we highlighted to the mean-field solution could be of use to quantify properly the (bio-)chemical reaction dynamics occuring in those systems.

Chapter 4

Impact of occlusions on blood flow organization

The influence of network topological changes induced by edge removals on the organization of the flow is an open question which has been investigated for decades in the porous media community. In the context of this thesis, vessel occlusions in brain micro-vascular networks have been recently shown to be a potential mechanism explaining the decrease of cerebral blood flow at early stages of Alzheimer disease's, which may trigger the biological pathways underlying the disease [21]. For instance, it has notably been shown in this paper that such occlusions lead to cognitive decline in mice. Furthermore, this work has also highlighted that the cerebral blood flow decrease, known for long time to go along with cognitive decline [4, 11, 15–20], might also be explained by the appearance of such occlusions. Starting from this observation, our goal in this chapter is to unravel the contributions of various sources of complexity present in brain micro-vascular networks on their resilience to vessel occlusions. These sources of complexity have led us to develop novel approaches accurately describing the underlying mechanisms leading to cerebral blood flow decrease induced by a random occlusion process.

4.1 Preliminary observations

As stated in the introduction of this thesis, brain micro-vascular networks are composed of two types of structures: the capillary bed and the arterioles and venules. The capillary bed, representing about 95% of micro-vessels, is a dense space-filling network with approximately homogeneous conductances and a topological community structure. By contrast, arterioles and venules are tree-like quasi-fractal structures with a large variability of their vessel conductance. In [21], occlusions leading to cognitive decline in Alzheimer's mouse models are located in the capillary bed. As a consequence, the impact of occlusions of arterioles and venules, which lead to brain infarcts and is also a current active field in brain disease research, lies beyond the scope of this thesis. Moreover, cognitive decline in Alzheimer's mouse models starts from a low percentage of occlusions ($\sim 3\text{-}5\%$) [21] and even in extreme circumstances, e.g. after a Middle Cerebral Artery stroke, the percentage of occlusions does not exceed 30% after reperfusion [129]. As a consequence, we focus our study to low to moderate fractions of occlusions while taking margins with higher fractions of occlusions experimentally observed. In that extent, we restrict in this chapter the maximal value of occlusion fractions to 40%.

In this first section, we present the preliminary study that motivated the analysis developed

in the present chapter. Doing so, we introduce some quantities and concepts that we found relevant to characterize the system response to an occlusion process. First, we introduce p_{occ} the fraction of occluded vessels and the global cerebral blood flow Q which is the sum of the flow of all arterioles, i.e. the inlets of the micro-vascular networks. In the absence of occlusions, the global cerebral blood flow is denoted Q_0 . Hence, Q/Q_0 is the relative decrease of the cerebral blood flow induced by the capillary occlusions. For a constant imposed pressure difference between network inlets and outlets, Q/Q_0 is equivalent to the relative decrease of the network conductance. Finally, we introduce the fraction of no-flow micro-vascular inlets f , i.e. the fraction of arterioles disconnected to all possible venules. For the considered range of occlusions, or dilute regime, the conductance, or inlet flow, of lattices of resistances has been shown to evolve linearly with the fraction of removed edges as [80]:

$$\left\langle \frac{Q}{Q_0} \right\rangle = 1 - \frac{Z}{Z-2} p_{occ} \quad (4.1)$$

with the above notations and where Z is the lattice connectivity. Here, $\langle \cdot \rangle$ stands for averages over multiple realizations. In the case of micro-vascular networks, most vertices have 3 connexions so that Z can be approximated as $Z = 3$. In the following, Eq. (4.1) will serve as a reference solution and, if not stated, $\langle \cdot \rangle$ will correspond to averages over 100 realizations.

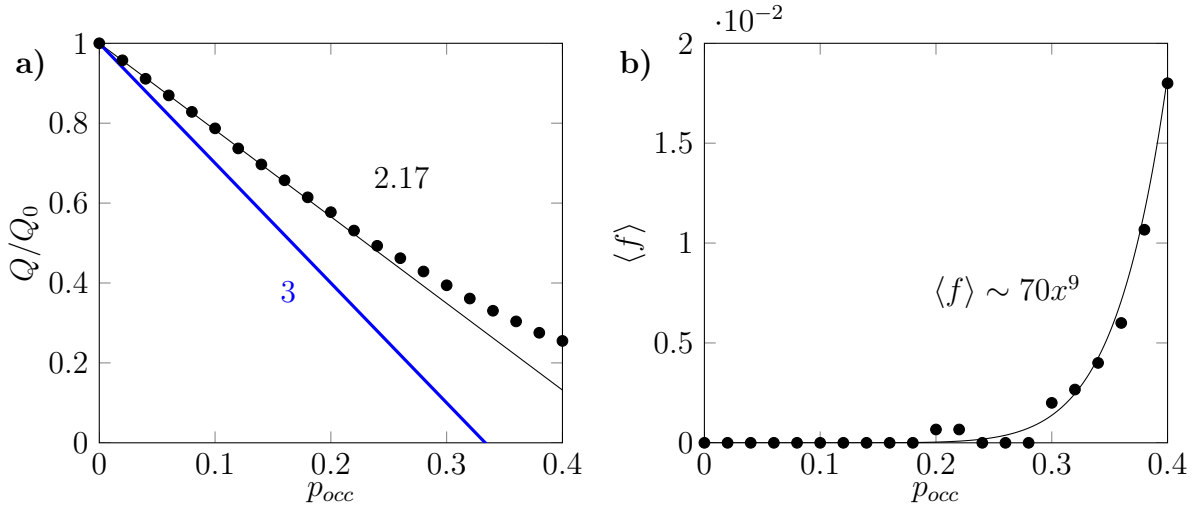


Figure 4.1: **Occlusions in the capillary bed induce a linear decrease in the cerebral blood flow before smoothening conjointly to a raise in the disconnection probability of perfusing arterioles.** **a)** Decrease of the cerebral blood flow as a function of the fraction of occluded capillaries. Average (black dots). Linear fit $y = 1 - 2.17x$ (black line). Effective medium prediction of Eq. (4.1) from [80] (thick blue line). **b)** Average fraction of no-flow arterioles as a function of the fraction of occluded capillaries (black dots) and power-law fit $y = 70x^9$ (black line).

Fig. 4.1 highlights few interesting characteristics of the micro-vascular network response to the occlusion process. First, in agreement with the behaviour in the classical dilute regime percolation, the decay of the average inlet flow is linear with the fraction of occluded vessels for a small percentage. However, the slope of the linear regime does not agree with the predictions of Eq. (4.1): instead of 3, we find a slope of about 2.17. This is consistent with the result previously

obtained in [21] where the slope is inferior, but close, to 2.5. Moreover, from $p_{occ} \approx 20\%$, the decrease of the mean inlet flow deviates from this linear trend and slows down smoothly in a non-linear fashion. This non-linearity, apparently conjoint to the start of the drastic increase of the fraction of disconnected arterioles (Fig. 4.1b), may signify the impossibility to predict this decay by effective medium approaches. In the following sections, we first investigate the physical mechanisms leading to the emergence of the fluctuations in the cerebral blood flow decrease by the study of the perturbation induced by a single occlusion. Doing so, we lay the foundations of a theoretical framework able to account for the impact of the various sources of brain micro-vascular network heterogeneities. Then, our objective in a second part is to unravel the contributions of these heterogeneities to the deviation of the average decrease of the inlet flow rate to Eq. (4.1).

4.2 Single occlusion

This section reproduces a manuscript written in collaboration with O. Giraud and B. Georgeot which has been submitted to Brain Multiphysics and is currently under review. In this article, we focus on the contribution of the capillary bed community structure [8, 9] on the flow resilience in micro-vascular networks to localized damage. Indeed, community structure has been shown in many systems, e.g. in disease spreading on networks but also for transportation or communication networks, to influence network robustness and function [130–135]. Here, we focus on the influence of the topological structure of micro-vascular networks on the variability of inlet flow decrease induced by a single occlusion neglecting for instance vessel conductance heterogeneities.

Network community structure and resilience to localized damage: application to brain microcirculation

Florian Goirand,^{1,2} Bertrand Georgeot,³ Olivier Giraud,⁴ and Sylvie Lorthois¹

¹*Institut de Mécanique des Fluides de Toulouse (IMFT), Université de Toulouse, CNRS, Toulouse, France*

²*Univ Rennes, CNRS, Géosciences Rennes, UMR 6118, 35000 Rennes, France.*

³*Laboratoire de Physique Théorique, Université de Toulouse, CNRS, UPS, France*

⁴*Université Paris Saclay, CNRS, LPTMS, 91405, Orsay, France*

(Dated: March 15, 2021)

In cerebrovascular networks, some vertices are more connected to each other than with the rest of the vasculature, defining a community structure. Here, we introduce a class of model networks built by rewiring Random Regular Graphs, which enables to reproduce this community structure and other topological properties of cerebrovascular networks. We use these model networks to study the global flow reduction induced by the removal of a single edge. We analytically show that this global flow reduction can be expressed as a function of the initial flow rate in the removed edge and of a topological quantity, both of which display probability distributions following Cauchy laws, i.e. with large tails. As a result, we show that the distribution of blood flow reductions is strongly influenced by the community structure. In particular, the probability of large flow reductions increases substantially when the community structure is stronger, weakening the network resilience to single capillary occlusions. We discuss the implications of these findings in the context of Alzheimer's Disease, in which the importance of vascular mechanisms, including capillary occlusions, is beginning to be uncovered.

I. INTRODUCTION

Cerebral hypoperfusion, i.e. the decrease of cerebral blood flow, is a common feature of many brain diseases, including neurodegenerative diseases, such as Alzheimer's Disease (AD) [1, 2], and cerebrovascular diseases, such as hypoperfusion dementia [3]. Hypoperfusion is a key player in the onset and progression of cerebrovascular diseases [3, 4] and has been considered until recently as a consequence of neurodegeneration in AD [5]. However, this view is now debated [1]. In human patients, cerebral blood flow indeed decreases — in a statistical and epidemiologic sense — before neurotoxic waste accumulate in the brain and before any measurable cognitive deficits [6]. Moreover, occlusions of capillary vessels by white blood cells (neutrophils) have been observed in animal models of AD before the accumulation of amyloid β , the main neurotoxic protein forming deposits (plaques) in AD brains [7]. Despite the small proportion of occluded vessels (1 to 4%), the pharmacological removal of these neutrophils led to a significant increase in blood flow and improved the cognitive performance of the animals. At a later stage, i.e. when the animals already showed plaques, extensive capillary constrictions have also been observed [8]. The exposition of pericytes, i.e. active mural cells wrapping around the capillaries, to increased concentrations of amyloid β has been shown to induce their contraction. This contributes to a positive feedback loop, where decreased cerebral blood flow not only triggers biological pathways leading to increased amyloid β production in the brain, but also directly impairs its elimination by the flowing blood. This results in increased amyloid β accumulation in the brain, increased pericyte contraction and further hypoperfusion [8]. In parallel, hypoperfusion also directly compromises the brain's energy supply, with deleterious neurological consequences.

A central question in this context is: to what extent could a small proportion of vessel occlusions trigger the above posi-

tive feedback loop, contributing to AD onset and progression? Using highly resolved simulations of blood flow in anatomically realistic microvascular networks from human and mice, it was previously shown that, on average, cerebral blood flow decreases linearly with an increasing proportion of capillaries occluded at random, up to 20%, i.e. without any threshold effect [7]. Thus, on average, each single capillary occlusion has a similar, and cumulative, contribution to the blood flow decrease at the scale of the network. Here, we focus on the variability of this contribution and seek to determine how it is controlled by the fundamental topological properties of cerebrovascular networks. In particular, we investigate the role of network communities, i.e. substructures with vertices more connected to each other than to other vertices, which have been identified in such networks [9, 10] and many other real-life networks [11, 12]. In social networks, for example, these communities represent groups of users with specific affinities, the identification of which is an important area of research [13, 14]. Such communities are also important to understand the organization of the World Wide Web [15, 16], as they influence the various page ranking algorithms.

In order to study the role of communities in brain microvascular networks, we take a step back and adopt a theoretical point of view, using model networks of increasing complexity, as illustrated in Fig. 1, but with a single inlet and outlet, and vessels with identical unit conductivity. On the one hand, this abstract approach enables to control the network community structure. On the other hand, it enables to derive analytical expressions, or to perform averages over many realizations of similar graphs with same properties, in order to analyze the variability of the blood flow reduction induced by the occlusion of a single vessel. We first consider simple ideal graphs known as Random Regular Graphs (RRGs) in network theory [17]. These graphs do not need to be embedded in the physical space and they are structureless. They nevertheless reproduce one of the main topological properties of cerebrovascular networks, in which most vertices have

the same coordination number (or degree), equal to three (see e.g. [9, 18, 19]). Moreover, many realizations of RRGs of arbitrary size can be easily constructed, and they locally behave like trees, enabling analytical derivations that provide insight on their asymptotic behavior in the limit of large sizes. We then modify this ideal RRG model to provide a simple generation scheme that enables to control the strength of the communities by rewiring together a finite number of elementary RRGs. As a third model, we use random networks constructed from Voronoi diagrams of sets of points homogeneously distributed in 3D space, following [19]. Such spatial networks are locally randomized but homogeneous at the network scale, and reproduce both the structure and function of brain capillary networks [19]. Finally, we also consider the intracortical vascular network from the mouse parietal cortex (15,000 vessels in a 1mm^3 region) used in [7]. In these last two anatomically realistic networks, by contrast with [20, 21], we neglect the contribution of vessel morphology, including distributions of diameters and lengths, and impose unit conductivity in all edges.

We use the above models to study the impact of single edge removal, i.e. equivalent to vessel occlusion. We show that the resulting flow reduction at network scale can be expressed as a function of the initial flow rate in the occluded vessel and a topological quantity, both of which display probability distributions with large tails. As a result, we show that the distribution of blood flow reductions may display unexpectedly large values, the probability of which increases when the community structure is stronger. Such results indicate that the topology of biological networks, including their community structure, is important to assess their functional properties, especially their biological resilience.

The paper is organized as follows. In Section II, we introduce the network models that will be considered, and investigate in Section III their topological properties compared to anatomically realistic networks. In Section IV, we consider blood flow through these networks. We uncover in particular the quantities controlling the distribution of flow reductions induced by the removal of a single edge and highlight how the network topological properties influence this distribution. Finally, in Section V, we discuss these findings and their implication for brain pathophysiology.

II. NETWORK MODELS

Network models have been used in many fields [22–27], where they proved useful to distinguish the main architectural properties of real-life complex networks that strongly impact their function from peculiarities which may depend on particular instances but do not change much the function.

Here, we start from the observation that, as stated in the Introduction, most vertices in cerebrovascular networks have three neighbours (either one vessel branches into two other vessels or two vessels merge into another one) [9, 19]. The simplest graph model one can think of to study such networks is a graph model only reproducing this feature, i.e. with con-

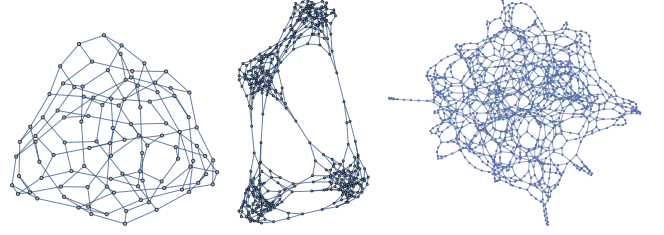


Figure 1: **Topological representation of typical realizations of various graph models.** From left to right: RRG with connectivity $z = 3$ and $N = 100$ vertices; rewired RRG obtained with $n_r = 10$ rewirings, starting from 4 RRGs of size $n_0 = 100$; Voronoi graph \mathcal{V} with $N = 1158$ vertices. Note that the figure only represents the existing connections (edges) between vertices, without accounting for their spatial position.

stant connectivity. Such graphs are known as regular graphs. Thus, the first model we consider is *random regular graphs* (RRGs), where each vertex has the same connectivity z , as illustrated in Fig. 1, left (see Appendix A for details).

RRG graphs by construction do not present specific substructures. However, in many real-life networks, including cerebrovascular networks, groups of vertices may have more links to each other than to other vertices [9, 10], defining substructures, or communities. In order to account for such communities, we also consider a slightly more elaborate model, which we call *rewired RRG* model. It is obtained by generating n_c independent RRG graphs, which may all have the same size or have a given heterogeneous size distribution, and rewiring pairs of edges at random, as illustrated in Fig. 1, middle (see Appendix A for details). In particular, we will denote by \mathcal{R}_k a subfamily of rewired RRGs built from a set of RRGs whose size is distributed to reproduce the communities of cerebrovascular networks, as further introduced in Section III B, and with k rewirings.

Both RRG and rewired RRG models are ideal graphs of infinite dimension [17, 22, 23, 28], which are not embedded in the physical space (i.e. vertices have no a priori physical spatial coordinates). Thus, to account for the 3D structure of the brain, we consider a phenomenological model, constructed from edges of Voronoi cells in the three-dimensional space, which reproduce both the structure and function of brain capillary networks [19] (see Appendix A for detail on the construction). The topology of a typical realization \mathcal{V} of such graphs, that we call *Voronoi graphs*, is displayed in Fig. 1 right.

Finally, we also construct a graph based on experimental data from a mouse brain previously acquired by [9, 18] (see Appendix A for details). By contrast to the previous graph, this experimental graph not only includes the space-filling capillary vessels, but also the tree-like penetrating arterioles and ascending venules [29]. Noteworthy, because these latter graphs are obtained from real 3D structures, vessels intersecting the edges of the considered region are cut. We recover the 3-connectivity of the graph by removing recursively all dangling vertices (vertices of connectivity one), and we keep only the largest connected component.

III. TOPOLOGICAL PROPERTIES

A. Distribution of loop lengths

The topology of a graph can be characterized by the lengths of the shortest paths connecting pairs of vertices. For instance, in scale-free graphs, hubs allow to connect any two vertices with a very short path [22]. A related quantity is the distribution of loop lengths in the graph [9, 19]. Here, we define a loop as the shortest path going from one vertex i to itself through two given neighbours of that vertex. For a vertex with z neighbours, there are $\binom{z}{2}$ loops. The loop length L is given by the total number of vertices (or edges) in the loop.

In Fig. 2, we display the loop length distribution $P(L)$ for the considered network models. As shown in the top panel, for a RRG of size N , the distribution is peaked around $2\ln N$, consistent with the RRGs being locally tree-like [30, 31]. In the same way, the loop distribution of a collection of several independent elementary RRGs of size n_0 is peaked at $2\ln n_0$. Under increased rewiring, the distribution progressively shifts

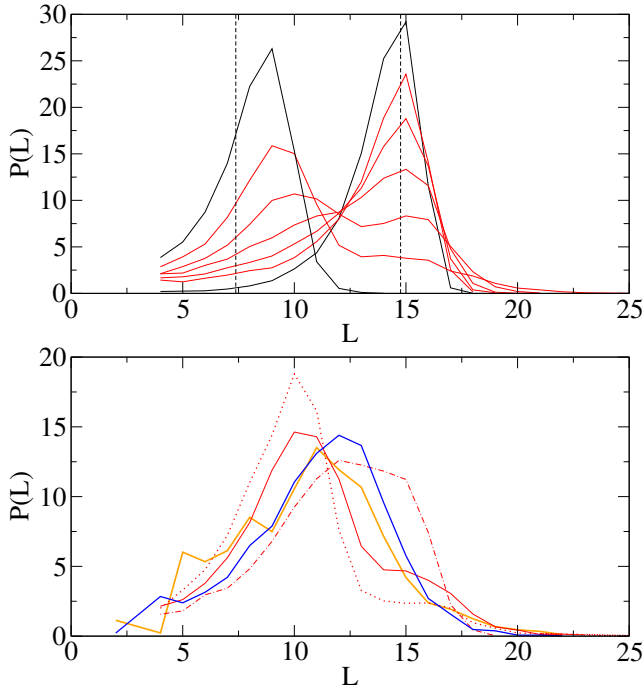


Figure 2: **Distribution of loop lengths. Top: Average loop length distribution for RRGs (black) with $N = 1600$ (right) or $N = 40$ (left), and rewired RRGs with 40 elementary RRGs of size 40 (red) and (from left to right) 100 to 500 rewirings; each histogram is obtained from 10 random realizations. The vertical dashed lines indicate $2\ln 40 \simeq 7.38$ and $2\ln 1600 \simeq 14.76$. Bottom: Distribution of loop lengths for a Voronoi graph and the mouse network, compared with distributions obtained for rewired RRGs \mathcal{R}_k of heterogeneous substructure size. Orange: Voronoi graph \mathcal{V} of Fig. 1 left; Blue: Mouse graph; Red: Average for 10 realizations of rewired RRGs \mathcal{R}_k , with $k = 40$ (dotted), 75 (solid) and 160 (dashed-dotted) rewirings.**

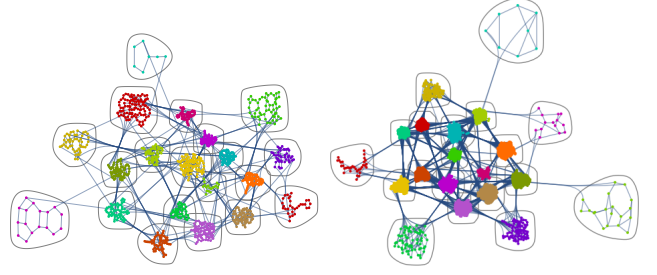


Figure 3: **Community graph plot of the Voronoi graph \mathcal{V} (left) and the mouse graph (right).** The 1158 vertices of \mathcal{V} distribute into 20 communities of sizes 103, 97, 81, 77, 74, 74, 72, 69, 68, 65, 60, 56, 53, 49, 44, 43, 31, 18, 17, 7. The 8720 vertices of the mouse graph distribute into 20 communities of sizes 833, 829, 791, 767, 757, 736, 727, 704, 696, 673, 491, 175, 155, 149, 93, 69, 34, 19, 14, 8.

towards the one of a RRG of size $N = n_c n_0$. Thus, rewired RRGs continuously interpolate between a distribution of loops peaked at a value only depending on the substructure size n_0 to one peaked at a value only depending on the total network size N .

Interpreting the loop length distribution of the Voronoi and mouse networks is less trivial. As shown in the bottom panel of Fig. 2, orange and blue lines, respectively, they are peaked at a similar value, irrespective of their different network sizes, suggesting that, for these networks, the dominant factor is the community size and not the network size. Moreover, the mouse network has a slightly larger proportion of loops with lengths above the peak compared to the Voronoi graph \mathcal{V} (orange line). This is consistent with earlier findings that the Voronoi graphs reproduce well the loop length distribution of cerebral capillary networks [19] and the additional contribution of tree-like arterioles and venules in the mouse network [32]. However, these distributions are larger than the typical distributions obtained in Fig. 2 top with rewired RRGs of equal size. Such distributions can be roughly reproduced by considering elementary RRGs with heterogeneous sizes (red lines in bottom panel). This suggests that the simple proposed model of RRG rewiring is sufficiently versatile to generate ideal graphs reproducing the topological properties of intracortical microvascular networks, by contrast to single RRGs, which do not account for the underlying substructures. In the next subsection, we thus focus on the community structure of these different networks.

B. Communities

As mentioned in the Introduction, communities are an ubiquitous feature of many real-life networks, and correspond to groups of vertices that are more likely to be connected together than with the rest of the graph. Such communities have been previously identified in brain microvascular networks [9, 10]. To identify these communities, we maximize the modularity $\mu(\mathcal{C})$ of all possible partitions \mathcal{C} , fol-

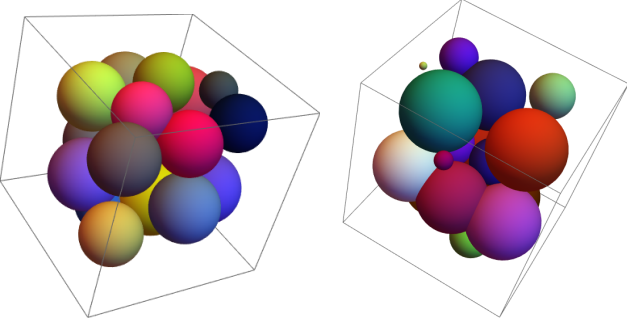


Figure 4: **Spatial localization of communities extracted from the Voronoi graph \mathcal{V} (left) and the mouse graph (right).** Spheres are centered at the barycenter of vertices in a given community, and their radius is given by the standard deviation of vertex positions around that barycenter.

lowing [11, 12, 33] and, in the case of intracortical networks, [9, 10]. The quantity $\mu(\mathcal{C})$ compares the probability of having an edge within a given subset of this partition with the probability expected by chance, i.e. from connections randomly chosen under the constraint of maintaining the graph connectivity z (see Appendix B for details). This quantity lies between $-\frac{1}{2}$ and 1, and is positive if the partition \mathcal{C} has some relevance as a graph community structure. We call modularity μ of the graph the maximal modularity over all partitions, or equivalently the modularity of the optimal partition (see Appendix B). Noteworthy, even for graphs such as single RRGs without any built-in substructures, the optimization process finds the specific partition of the graph which maximizes the modularity. The value of $\mu(\mathcal{C})$ for this particular partition is usually well above zero. Thus, for single RRGs, we obtain an average modularity $\mu_{\text{RRG}} \sim 0.661$ when averaged over many realizations. This value corresponds to purely random fluctuations, which create random clusters of vertices more tightly bound together than with the rest of the graph. Higher values are expected for the graph community structure to have any relevance. In this case, we directly use the modularity to assess the strength of the obtained community structure. For the Voronoi graph we find $\mu_{\mathcal{V}} \sim 0.827$ and for the mouse graph $\mu_{\text{mouse}} \sim 0.846$. Besides modularity, alternative quantities have also been used for that purpose, for example the exponent of the scaling law relating the number of inter- versus intra-community edges [9]. However, the range of exponents characterizing strong communities depends on the dimension of the space in which the graph is embedded [54], making it difficult to compare real-life networks and ideal graphs such as RRGs or rewired RRGs.

Below, we first examine the community structure of the Voronoi and mouse networks, and subsequently discuss how to incorporate these findings into the rewired RRG model. The community structures of the Voronoi and mouse networks are displayed in Fig. 3. Consistent with a high modularity value, the number of edges within communities is much larger than the number of edges connecting different communities. Moreover, these communities are highly segregated in

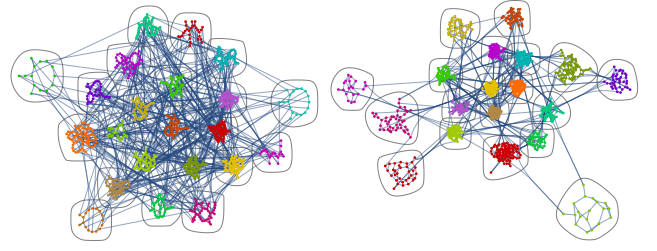


Figure 5: **Community graph plot of a generic RRG of size $N = 1000$ (left) and a rewired RRG \mathcal{R}_{75} (right).**

space, i.e. with few overlap, as displayed in Fig. 4. In this figure, we use the spatial information about vertices of our 3D graphs to represent each community by a sphere, centered at the barycenter of its vertices and with a radius equal to the standard deviation of vertex positions around that barycenter. Not surprisingly, this suggests that in such systems, communities are a manifestation of the spatial organization of the network, and that vertices in a given spatial region make extensive connections with the neighboring vertices. By contrast, in pure RRGs, the community structure is mainly irrelevant. Communities in RRG graphs are highly connected to each other (Fig. 5, left) and the average modularity is much lower ($\mu_{\text{RRG}} \sim 0.661$), even if, as said above, the maximization procedure always produces some spurious community structure by construction.

Relevant communities are recovered for the rewired RRGs (see e.g. Fig. 5, right, where communities associated to rewired RRGs of heterogeneous sizes are displayed). From the results presented in the previous Subsection, we expect that increasing the number of rewirings will result in approaching the behavior of a single, larger, RRG. This results in weaker communities, i.e. a network with lower modularity, as illustrated in Fig. 6, and increased ratio of inter- versus intra-community edges. Below, we seek to estimate the number of rewirings needed to construct heterogeneous rewired RRGs with both community structures (defined by their number and size) and modularity matching those of a given real-life network.

For example, in the case of Voronoi \mathcal{V} , the network has 1422 intra-community edges and 182 inter-community edges, and thus the ratio between inter and intra edges is ≈ 0.128 . Choosing a rewired RRG with elementary RRG sizes given by the communities of \mathcal{V} , we find a linear dependence of this ratio with the number of rewirings (inset of Fig. 6). To match the inter- over intra-edge ratio of \mathcal{V} , this yields, via the fit of Fig. 6, $n_r = 74.79 \approx 75$ rewirings. The so obtained random graphs will be denoted by \mathcal{R}_{75} in the remaining of this paper. Their average modularity (obtained by averaging over 100 realizations) is equal to $\mu_{\mathcal{R}_{75}} \approx 0.817 \pm 0.0065$, which is indeed very close to the modularity of the Voronoi and mouse graphs. [55].

Noteworthy, the resulting distribution of loop lengths $P(L)$ for such a number of rewirings matches well the distribution of loop lengths of Voronoi \mathcal{V} (see Fig. 2), despite the fact

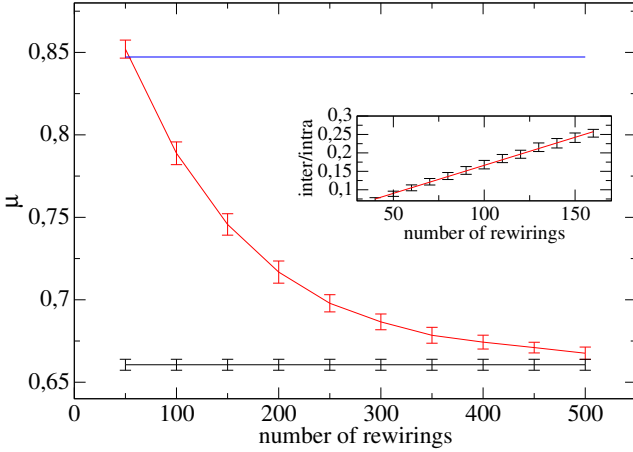


Figure 6: **Graph modularity for rewired RRGs as a function of the number k of rewirings.** Red: rewired RRGs \mathcal{R}_k , as defined in Appendix A, average and standard deviation obtained from 100 realizations; Black: result for generic RRGs of same size ($\mu = 0.661 \pm 0.003$ for 100 realizations); Blue: result for the mouse graph with one single realization. Voronoi graph \mathcal{V} has modularity $\mu = 0.827$, corresponding to ~ 70 rewirings. **Inset: Mean number of inter-versus intra-community edges in a rewired RRG \mathcal{R}_k as a function of number k of rewirings.** Average and standard deviation from 100 realizations. The red line is the best linear fit ($y = 0.0285 + 0.00304x$).

that the 3D structure is entirely absent from the rewired RRG model. This similarity also manifests in the community structure displayed in Figs. 3 and 5.

The results of this Section show that topological features such as the community structure are important properties of intracortical microvascular networks. These properties can be implemented in the RRG model by adding a community structure and a certain amount of rewiring. Such models can describe correctly the loop distribution and the modularity of the real networks, while having no other features left in the model. They also enable to perform averages over all realizations of these networks, which all have the same structure, a useful tool to get statistically significant quantities and assess the variability of the results. We will use these models in the next Section to study the resilience of the above networks to single-edge occlusion and assess its dependence on modularity.

IV. BLOOD FLOW THROUGH THE NETWORK

We now connect the previous graphs with the outer world by adding a single inlet edge and a single outlet edge (see Fig. 7). Following [20, 21], we also ignore the complex rheology of blood, so that imposing a constant pressure (potential) difference between the tips of these edges results in establishing a stationary flow field throughout the network, that can be obtained by inverting a linear system of equations [21, 34]. In the present Section, we shall examine how occluding a sin-

gle vessel affects the total flow rate transported through the network.

A. Definitions

Starting from a graph \mathcal{G} with $M = N - 2$ vertices, we pick up two edges at random, and add two vertices I and O in the middle of these edges. To these vertices, which now are the $N - 1^{th}$ and N^{th} vertices of the graph, we respectively connect an inlet vertex I' and an outlet vertex O' . Note that, in that way, a graph with constant connectivity $z = 3$ keeps that property.

Let p_i denote the potential (pressure) at vertex i for $1 \leq i \leq N$. The local flux (flow rate) from i to j is defined as

$$q_{ij} = \gamma_{ij}(p_i - p_j), \quad (1)$$

where γ is the matrix of conductivities.

For $i = 1$ to $N - 2$, Kirchhoff's current law yields

$$\sum_j \gamma_{ij} p_j - \left(\sum_j \gamma_{ij} \right) p_i = 0, \quad 1 \leq i \leq N - 2, \quad (2)$$

where γ_{ij} is the conductivity of edge ij . For $i = N - 1$ or N , there is an additional flux $\gamma_{iI'}(p_i - p_{I'})$, where $p_{I'}$ is the corresponding imposed potential ($p_{I'}$ or $p_{O'}$), yielding

$$\sum_{j \neq I'} \gamma_{ij} p_j - \left(\sum_j \gamma_{ij} \right) p_i = -\gamma_{iI'} p_{I'}, \quad i = N - 1, N \quad (3)$$

where $\gamma_{iI'}$ is the conductivity of the newly added edges, which will be denoted by $\gamma_{I'}$ for the inlet and $\gamma_{O'}$ for the outlet in the following. Let A be the $N \times N$ matrix defined by

$$A_{ij} = \begin{cases} \gamma_{ij} & \text{if } i \neq j, \\ -\sum_k \gamma_{ik} & \text{if } i = j, \end{cases} \quad (4)$$

for $1 \leq i, j \leq N$, and the sum over k runs over all neighbours of i , including i' [56]. We define vector b as the vector with entries $-\gamma_{iI'} p_{I'}$ at position $i = N - 1$ and N and 0 elsewhere, that is, $b = (0, \dots, 0, -\gamma_{I'} p_{I'}, -\gamma_{O'} p_{O'})^T$. Then, from Eqs. (2) and (3), the vector p is the unique solution of $Ap = b$. Generically, A is invertible, so that p is explicitly given by $p = A^{-1}b$.

In Fig. 7, we illustrate the fluxes q_{ij} for one inlet point I' on the left and one outlet point O' on the right of a single RRG. By mass conservation, the total flow rate Q transported through the network is equal to the inlet and outlet fluxes. Thus, with the above notations, $Q = \gamma_{I'}(p_{I'} - p_I) = \gamma_{O'}(p_O - p_{O'}) = \Gamma(p_{I'} - p_{O'})$, where Γ denotes the overall network conductance. We also denote by $\delta P = p_{I'} - p_{O'}$ the fixed value of the potential difference between the inlet and outlet. Then $Q = \Gamma \delta P$. We will now examine how Q , or equivalently Γ , is affected by the removal of one edge.

B. Flow reduction induced by removing one edge

We now denote by Q'_{ij} the total flow rate transported through the network when edge $i - j$ is removed, and by

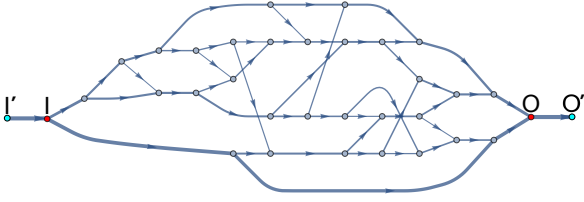


Figure 7: **Flow field in a single RRG.** Here, $M = 30$ ($N = 32$). The two boundary vertices (I' and O') are highlighted in cyan. The two vertices added to connect these boundaries to the graph (I and O), are highlighted in red. Arrows show the direction of flow q while edge thickness is proportional to $1/|\log|q||$.

$\delta Q_{ij} = Q - Q'_{ij}$ the corresponding flow reduction. This flow reduction can be expressed as follows (see Appendix C)

$$\frac{\delta Q_{ij}}{Q} \equiv \frac{(Q - Q'_{ij})}{Q} = \frac{\Gamma}{\gamma_{ij}} \frac{1}{t_{ij}} \left(\frac{q_{ij}}{Q} \right)^2, \quad (5)$$

where q_{ij} is the initial flux in the removed edge and $t_{ij} = 1 + \gamma_{ij}[(A^{-1})_{ii} + (A^{-1})_{jj} - 2(A^{-1})_{ij}]$ is non-dimensional.

In what follows, for simplicity, we will only consider the case where the pressure reduction $\delta P = p_{I'} - p_{O'} = 1$ is fixed, so that $Q = \Gamma$, and where all conductivities γ_{ij} are taken equal to 1. Equation (5) reduces to

$$\delta Q_{ij} = \frac{q_{ij}^2}{t_{ij}}. \quad (6)$$

Equation (6) states that the total flow reduction induced by removing one edge $i - j$ is quadratic in the initial flux q_{ij} through this edge, and inversely proportional to t_{ij} . Below, we further examine the properties of these two quantities governing the flow reduction.

C. Cauchy laws for the quantities governing the flow reduction

It is first possible to get an insight into the denominator t_{ij} in Eq. (6) by considering the asymptotic case of very large regular trees (see e.g. [35, 36]). For that purpose, let us denote by $G(x) = (A - x\mathbb{1})^{-1}$ the Green function of matrix A , so that $A^{-1} = G(0)$. In the case where the off-diagonal elements of A are those of the adjacency matrix of an infinite regular tree, one can find a recursive relation between the diagonal elements of $G(x)$. The latter expresses $G_{ii}(x)$ as a function of the $G_{jj}(x)$, with j the children of i , and of the diagonal elements of A (see e.g. [35, 36]). For infinite trees, all vertices i are at the root of statistically identical trees. Therefore $G_{ii}(x)$ behaves as a random variable G and all $G_{jj}(x)$ behave as independent random variables G_p with the same distribution as G . These are solutions of the recursive equation

$$G = \frac{1}{c - x - \sum_{p=1}^{z-1} G_p}, \quad (7)$$

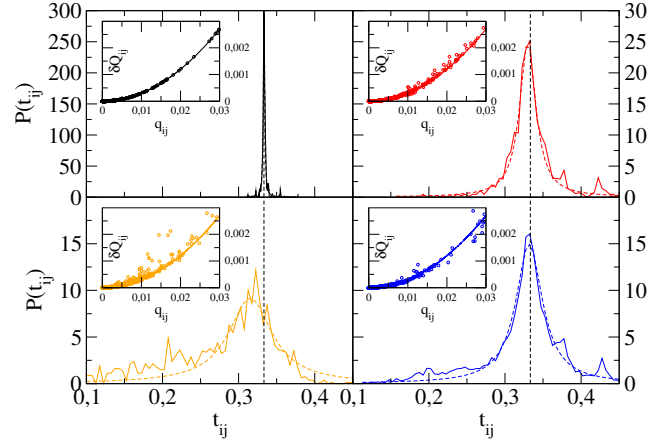


Figure 8: **Distribution of t_{ij} for (i, j) running over all edges of a single realization of a graph.** Solid lines display numerical results, dashed lines Cauchy fits (8). Top: RRG (left), rewired RRG \mathcal{R}_{75} (right); Bottom: Voronoi \mathcal{V} (left), Mouse (right). **Insets: flow reduction δQ_{ij} as a function of q_{ij} , illustrating the quadratic dependence given by Eq. (6).**

where z is the graph connectivity and c is a random variable distributed in the same way as the diagonal elements of A . When the graph is no longer an infinite tree but a finite random regular graph, Eq. (7) is only approximate.

It is known in statistical physics [35] that the mean-field solution of this recursive equation amounts to approximating the exact solution (in the form of a probability distribution of $G_{ii}(x)$ as a random variable) by symmetric Cauchy distributions. As a result, $(A^{-1})_{ii}$ is expected to follow a Cauchy distribution, so that, by stability of Cauchy distributions, the quantity $t_{ij} = 1 + (A^{-1})_{ii} + (A^{-1})_{jj} - 2(A^{-1})_{ij}$, which corresponds to the denominator in (6), is also likely to follow a Cauchy distribution.

In Fig. 8, we plot the distributions of t_{ij} for all our networks models, from RRGs to the mouse network. Whatever the considered graph, these distributions are indeed well-fitted by Cauchy distributions

$$P(t) = \frac{1}{\pi} \frac{a}{a^2 + (t - t_0)^2}, \quad (8)$$

where t_0 is the median value and a is the half width at half maximum (HWHM) [37]. Besides, in all cases, we numerically find that the median value t_0 is close to $1/3$, and thus the prefactor of q_{ij}^2 in (6) is close to 3. This result can be recovered by generalizing the reasoning of [21, 38], initially introduced to study the dilute regime of bond percolation. For regular networks of connectivity z with a single inlet and outlet, we show in Appendix D that the flow reduction can be approximated by

$$\delta Q_{ij} = \frac{z}{z-2} (p_i - p_j)^2 \quad (9)$$

in the limit of infinite size and under the assumption that the graph is isotropic at the inlet and outlet. The inset of Fig. 8

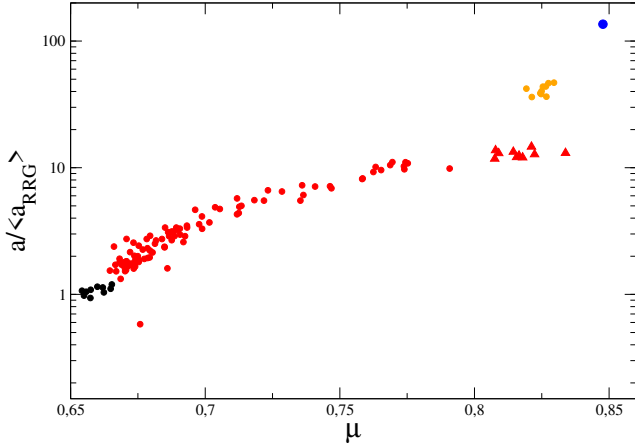


Figure 9: **Width a of the Cauchy distribution (8) (normalized by the average Cauchy width of a RRG graph of same size) as a function of graph modularity.** Each point is a single graph realization. RRG (black), rewired RRG (red) for \mathcal{R}_{75} (triangles) and \mathcal{R}_k with $k = 100$ to 200 (circles) rewirings, Voronoi (orange), and Mouse (blue).

shows that this quadratic law is well verified whatever the considered graph. In our case, $z = 3$ and thus the prefactor of $(p_i - p_j)^2$ in (9) is $\frac{z}{z-2} = 3$, recovering $1/3$ as the median value t_0 of the Cauchy distribution for t_{ij} .

In addition, Cauchy laws have fat tails. As a result, the occurrence probability of small and large values of quantities following Cauchy distributions is much larger than for normal distributions. For instance, the probability of values smaller than $t_0 - 3a$, where t_0 denotes the median and a is the HWHM, is ≈ 0.0002 for a Gaussian distribution whereas it is ≈ 0.1 for a Cauchy distribution, i.e. five hundred times higher. Thus, there is a number of values of the t_{ij} which are very small. When such an edge $i - j$ is removed, this translates into a prefactor of the flow reduction q_{ij} which is particularly high, inducing a significant drop in the total flow Q . As a result, the larger the Cauchy distribution in Fig. 8, the larger the fluctuations observed around Eq. (9) in the corresponding inset.

Importantly, the half width a of the Cauchy distribution strongly depends on the community structure of the underlying graph. In Fig. 9, we show that for graphs of comparable size, the width increases with the graph modularity, significantly increasing the probability of large flow reductions resulting from the removal of a single edge.

We now turn to the distribution of q_{ij} , the numerator in (6). This distribution can be understood based on similar arguments as above. From (1), local fluxes are indeed obtained by linear combinations of potentials $p = A^{-1}b$, leading to a Cauchy distribution in the case of infinite trees. Besides, because of flow reversibility, its median value is expected to be zero. This is consistent with the blood flow distributions computed in realistic intracortical networks from mice [39]. These distributions have fat algebraic tails (power laws with exponent -2) characteristic of Cauchy distributions, which can alternately be interpreted, based on hydrodynamic arguments,

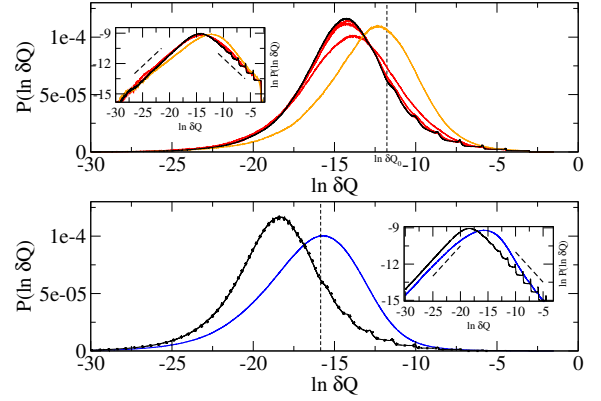


Figure 10: **Top panel: Distribution of $\ln \delta Q$ for (i, j) over all edges.** Black : 100 realizations of generic RRGs with $N_1 = 1176$; Orange: Voronoi (100 realizations); Red: 1000 realizations of rewired RRGs \mathcal{R}_k with random k , $100 \leq k \leq 600$, divided into 20 sets of 50 realizations, where in each set graphs have approximately the same modularity; histograms for sets 10, 15 and 20 are shown (three red curves with modularity increasing from left to right). All histograms are averaged over windows of size ~ 1 in $\ln \delta Q$. The dashed vertical line indicates position $\ln \delta Q_0 = -11.773$ where 25% of the probability lies on the right for the generic RRG of size N_1 . **Bottom panel: same for mouse (blue) and RRGs with $N_2 = 8720$ (black, 100 realizations)** ; dotted black corresponds to the RRG of size N_1 translated to the left by $\ln \frac{N_2^2}{N_1^2} \simeq 4$ units in logarithmic scale. With this translation, both RRG distributions coincide, showing that the $1/N^2$ scaling obtained in Appendix E corrects perfectly for the size effect in case of RRGs. The dashed vertical line corresponds to the vertical line in the top panel translated in the same way. **Insets: same in log scale.** Dashed lines indicate slopes $\pm \frac{1}{2}$.

as emerging from dipole-driven flows on random networks. Their properties have been investigated in [39], but the impact of the community structure has not been considered. Following the same approach as above, we find however that modularity affects significantly less the width of the distribution of q_{ij} compared to the one of t_{ij} .

D. Distribution of flow reductions

After having determined the distribution of the denominators and numerators in Eq. (6), we now turn to the distribution of flow reductions δQ_{ij} , which controls the variability of the global network response to the removal of a single edge. There is no general result which describes this distribution for both q_{ij} and t_{ij} following Cauchy distributions. In Appendix E, however, assuming that the distribution of flow reductions is mainly controlled by the distribution of flow rates within the network, we show that for a regular graph and in the limit of large sizes, the left tail of the distribution of $\ln \delta Q_{ij}$ is expected to follow $P(\ln \delta Q) \sim 1/\delta Q^{-1/2}$ and the right tail is expected to follow $P(\ln \delta Q) \sim 1/\delta Q^{1/2}$.

As shown in Fig. 10 (insets), this asymptotic behavior is indeed correctly reproduced for the elementary RRGs (black

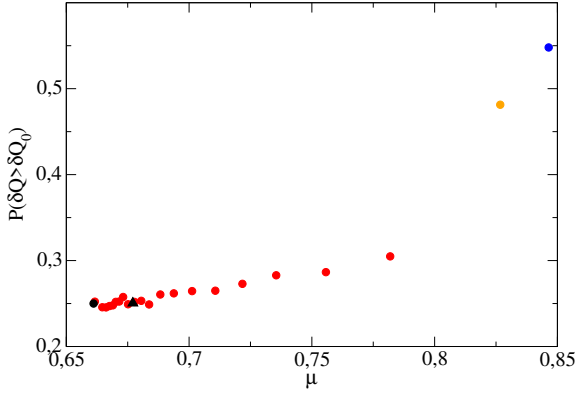


Figure 11: **Probability of flow reductions larger than flow threshold δQ_0 as a function of modularity.** δQ_0 is chosen to correspond to the third quartile of the distribution obtained for the RRG of same size, as displayed in Fig. 10 by dashed vertical lines. Same color code as Fig. 10 (RRG with $N_1 = 1176$ is the black circle, RRG with $N_2 = 8720$ is the black triangle).

lines), so that the distribution of $\ln \delta Q$ is approximately symmetric. For these structureless graphs, it is also obvious that the position of its maximum, denoted by $\ln \widehat{\delta Q}$, strongly depends on the network size (compare black lines in top ($N_1=1176$) versus bottom ($N_2=8720$) panel in Fig. 10). As shown in Appendix E for large RRGs, we expect $\widehat{\delta Q}$ to scale as $1/N^2$. Thus, the two distributions obtained for RRGs with sizes $N_1 = 1176$ and $N_2 = 8720$ should match by a translation of the former by N_2^2/N_1^2 to the left. This is verified in the bottom panel of Fig. 10 (superimposed black line and black dots) and suggests that, for these structureless graphs, the distribution of flow reductions is indeed controlled by the distribution of flow rates throughout the network. However, whatever the graph size, the distributions of $\ln \delta Q$ become distorted towards larger values when the modularity increases, i.e. for graphs with substructures. As a result, the corresponding distributions slowly depart from the above predicted scalings, especially for large values of δQ_{ij} , and the location of their maxima increases. This is consistent with the concomitant increase of a , the width of the distribution of the denominator in Eq. (6), demonstrated in the previous Section.

To further quantify the effect of modularity, we plot in Fig. 11 the probability of flow reductions larger than a given threshold δQ_0 , chosen to correspond to the third quartile of the distribution obtained for the RRG of same size [57]. From this arbitrary choice, this proportion is obviously 25% for both RRGs. It increases almost linearly for increasing modularities, up to $\sim 30\%$ for the rewired RRGs. It even increases by almost two-fold for the Voronoi and mouse networks. Thus, in general, a stronger community structure is clearly associated with a higher probability of large flow reductions when removing one edge. As a result, in brain microvascular networks, the removal (or equivalently the occlusion) of one single vessel yields probabilities of large blood flow reductions that may be more than twice the prediction for graphs without substructures.

V. CONCLUSION AND PERSPECTIVES

We have investigated the topological structure of cerebrovascular networks, based on an anatomical network extracted from a mouse brain, model capillary networks derived from space-filling Voronoi tessellations and different graph models belonging to the class of Random Regular Graphs. We have shown that the anatomical network contains substructures corresponding to communities of vessels, which are geographically localized in 3D. The proposed models including such communities provide a reasonable representation of the topology of cerebrovascular networks, as highlighted by their similar loop distributions.

We have then studied how the strength of these communities affects the distribution of global flow reductions when an edge is removed, or, equivalently, when a single vessel is occluded. For that purpose, we have shown that the resulting flow reduction at network scale can be expressed as a function of the initial flow rate in the occluded vessel and a topological quantity. Both of them display probability distributions with large tails, resulting in a large probability of rare events. The presence of community structures even enlarges the tail of the distribution of the topological quantity, resulting in general in a distribution of flow reductions shifted towards larger and larger values when the community structure becomes more pronounced. In other words, the community structure weakens the network resilience to capillary occlusions, by increasing the probability of larger flow reductions, inducing a large variability of the impact of a single vessel occlusion depending on its location in the network.

The proposed theoretical approach neglects the heterogeneity of vessel conductivities. In other words, by contrast to [20, 21, 40], we ignored the contribution of vessel morphology, including distributions of diameters and lengths. We also ignored the complex rheology of blood [34, 41, 42]. Our results are nevertheless consistent with recent work modeling the impact of single capillary occlusion in highly resolved numerical simulations accounting for blood microvascular rheology in anatomically realistic microvascular networks [40], focusing on local flow reorganizations in the vicinity of the occluded vessel. Not surprisingly, the results, obtained for a total of 96 occluded capillaries representing less than 1% of capillaries, exhibited considerable numerical dispersion, which has been pointed out by the authors as a methodological difficulty. Nevertheless, the median volume of the region with flow reductions above 20% has been shown to increase by a factor 2.5 between capillaries with low initial flow rate and those with high initial flow rate. This suggests that the present theoretical framework, which enables using graph models and focusing on network topology, keeps enough physical ingredients to be relevant.

While this does not sufficiently reduce the complexity of the problem to yield a complete theory relating the community structure to the shape of the distribution of flow reductions (providing e.g full analytical derivations), it still enables to deduce relevant asymptotic scalings for all quantities controlling this distribution, which considerably helps to interpret the numerical results obtained in the mouse and Voronoi networks.

Noteworthy, the last decades have seen tremendous progress of in vivo experimental techniques, including multiphoton microscopy and laser-based techniques that enable to selectively occlude microvessels in rodent brains [43]. This offers large possibilities of data collection, which may be useful to validate our findings. In a complementary way, the present theoretical framework may help enrich data interpretation, e.g. by considering the impact of network communities on flow reorganizations or by enabling the expected broad distribution of flow reductions to be taken into account in the statistical design of the studies.

Moreover, the present work provides a theoretical basis for future studies about the impact of multiple capillary occlusions [7] on cerebrovascular function. As mentioned in the Introduction, this may help to understand the interplay between hypoperfusion and amyloid-induced neurodegeneration in the onset and progression of AD [1]. We may in particular speculate that the microvascular community structure evolves with disease progression. For example, capillary occlusions at early stages of the disease, i.e. in healthy networks, may strengthen their community structure. This would increase the probability of larger blood flow reductions induced by further occlusions, providing an additional self-amplificatory mechanism in the positive feedback loop linking hypoperfusion and neurodegeneration in AD [1]. In the same way, different network organizations in different brain areas (e.g. primary versus secondary cortex, subcortical regions, hippocampus), which are being uncovered thanks to whole brain post-mortem vascular network reconstructions in rodents [44], may be a clue to explain their different vulnerabilities, e.g. understand why the hippocampus is one of the first damaged brain regions exhibiting cognitive deficits in AD. Long-term vascular remodelling, including capillary rarefaction, in normal or pathological aging [45] may also contribute to modify the community structure of vascular networks in the brain, thus providing an additional mechanism which may explain the considerable overlap between vascular pathology and AD [3, 5].

To investigate the above assumptions, new datasets finely mapping the whole-brain vascular architecture of rodents in normal aging and at different stages of various brain diseases, including AD, are needed. Moreover, the present framework should be enriched to account for multiple occlusions, e.g. by introducing a perturbation approach valid in the dilute limit, where the removal of edges can still be considered independent of each other. Multiple network inlets and outlets should also be considered. The vascular network within the brain cortex is indeed fed and drained by a large number of penetrating arterioles and ascending venules [9, 46], which may contribute to enhance the network resilience to capillary occlusions. By contrast, occlusions of penetrating arterioles induce dramatic damage, as shown by a comprehensive series of in vivo experiments [9, 29, 47–49]. This has been interpreted as resulting from insufficient compensatory collateral flow from other network inlets through the capillary bed, as reviewed in [46]. Our result suggest that it may alternately be understood as resulting from the hierarchical organization of the network, inlet (and outlet) vessels being those carrying the largest flow rates, thus leading to the largest flow reduc-

tions, both at network scale and, by extension, recursively in the neighborhood of the occluded vessel. This phenomenon is likely to be increased if conductance heterogeneities are taken into account, such vessels displaying the largest conductances, leading to correlations between high flow and high conductance, while such correlations are negligible in the capillary network. Besides AD, this would open perspectives in the context of ischemic stroke, where neutrophil occlusions of up to 30% of capillary vessel have been recently discovered, preventing reperfusion after recanalization of the upstream cerebral artery [50].

Acknowledgements.

Research reported in this publication was supported by the European Research Council under ERC grant agreements 615102 (BrainMicroFlow) and 648377 (ReactiveFronts) and by the NIH (awards R21CA214299 and 1RF1NS110054). We gratefully acknowledge P. Blinder, P. Tsai and D. Kleinfeld for sharing anatomical networks. OG wishes to thank Laboratoire de Physique Théorique (IRSAMC, Toulouse) for their kind hospitality.

Appendix A: Details on the construction of network models

All network models considered in the present paper are defined using a graph description of their topology, i.e. including a set of N vertices connected by edges. Thus, each edge $i - j$ is uniquely defined by its two endpoint vertices i and j . In addition, when the network model is embedded in the 3D physical space, all vertices i have distinct coordinates (x_i, y_i, z_i) .

There is a finite number of graphs with a fixed number N of vertices. If we assign a certain probability to each of them, we get ensembles of *random graphs*. Random graphs allow to make generic statistical predictions on real-life systems (see [51] for a review). The most popular models are regular graphs [25] (in which each vertex has the same connectivity z), Erdős-Rényi graphs [52, 53], or scale-free graphs [22], depending on the problem under consideration. Here we consider the following models.

Random regular graphs. Random regular graphs (RRGs) denotes a subset of graphs uniformly distributed over the finite set of random regular graphs of size N with a given connectivity z . Algorithms have been proposed to randomly generate such a subset [28]. In practice, we use the Random-Graph function of Mathematica. Note that for a graph with N vertices, there are in total zN edge endpoints, and since each edge has two endpoints, zN must be even. In particular, for $z = 3$, as is the case in this paper, we must choose N to be even.

Rewired random regular graphs. We start from a set of n_c independent RRGs of arbitrary even size. We then pick a pair of edges $(i - j, i' - j')$ at random and replace it with $(i - j', i' - j)$. We iterate this random rewiring n_r times. At moderate n_r , the graph keeps some remnant features of its

initial elementary components, while for $n_r \rightarrow \infty$, it behaves like a single RRG. The initial n_c RRG graphs may have all the same size or different ones. In most numerical applications, we will consider a rewired RRG built from 20 elementary RRGs of sizes 102, 96, 80, 76, 74, 74, 72, 68, 68, 64, 60, 56, 52, 48, 44, 42, 30, 18, 16, 6. These sizes correspond to those of the communities of one of the Voronoi graphs (denoted \mathcal{V} in the text and defined below), see caption of Fig. 3, with odd sizes rounded off to even numbers. Such a rewired RRG with k rewirings will be denoted \mathcal{R}_k .

Voronoi graphs. In addition to having mostly 3-connected vertices, the network of capillary vessels, i.e. the smallest vessels within the brain cortex, is space-filling [19, 32]. This last property can be reproduced by constructing 3D Voronoi diagrams from sets of seed points randomly distributed under the strong constraint that there is only one seed point in each cube of a 3D cubic grid. However, these Voronoi diagrams have high connectivity, with many vertices of degree up to 5. By randomly merging, pruning or adding vertices following the geometrical constraints described in [19], we get 3D model networks statistically reproducing most of the morphological, topological and transport properties of brain capillary networks [19]. Because these networks are generated in a 3D cubic region, all boundary edges are cut and dangling, so that their outer boundary vertex is only 1-connected. In the present paper, we recursively remove these dangling edges, so that all remaining vertices are at least of degree 2. For simplicity, the resulting graphs are described as *Voronoi graphs* in the present paper. One of them, which we denote \mathcal{V} , serves as an illustration throughout the paper.

Mouse graph. We use the graph description of a large postmortem dataset ($\sim 1 \text{ mm}^3$ and $\sim 15,000$ vessel segments) from the mouse vibrissa primary sensory (vS1) cortex previously obtained by [9, 18]. While this dataset contains vessel diameters and labels classifying vessels in arterioles, capillaries and venules, we discard this information and consider that all edges are equivalent, with unit conductivities. As above, we recursively remove all dangling edges.

Appendix B: Communities and modularity

A graph \mathcal{G} with N vertices can be partitioned into communities, which are subsets \mathcal{C}_k of vertices. Intuitively, a community \mathcal{C}_k is such that vertices in \mathcal{C}_k are highly connected to one another, with comparatively fewer edges connecting them to vertices outside the community. There is however no unique answer to the question of what a meaningful partition of a graph is. Under reasonable assumptions, it is possible to construct many functions that quantify the relevance of a given partition for community detection [12].

One such function which has been very much used for that purpose in network theory is the modularity [33], which for a

given partition \mathcal{C} into subsets \mathcal{C}_k is defined as

$$\mu(\mathcal{C}) = \frac{1}{2m} \sum_k \sum_{i,j \in \mathcal{C}_k} \left(a_{ij} - \frac{d_i d_j}{2m} \right). \quad (\text{B1})$$

In this expression a_{ij} is equal to 1 if there is an edge connecting vertices i and j , and to 0 otherwise, d_i is the number of outgoing edges of i , m is the total number of edges, and the sum runs over all subsets \mathcal{C}_k in the partition. The sum $\sum_{i,j \in \mathcal{C}_k} a_{ij}$ gives (twice) the number of edges within the set \mathcal{C}_k . The number $d_i d_j$ is the number of edges that could connect i and j if they were taken at random. The modularity thus compares the mean probability of having an edge of the graph \mathcal{G} within a set \mathcal{C}_k to the probability of having such an edge in a graph \mathcal{G}' where all vertices have the same degree as in \mathcal{G} but edges are chosen at random.

The various possible functions characterizing the relevance of the partition lead to different methods for community detection in graphs (for a review see [12]). We used modularity-based clustering algorithms, which go through the space of possible partitions trying to maximize the modularity. In practice, we use the FindGraphCommunities function of Mathematica. The algorithm finds the optimal partition with the largest modularity for a given graph. This enables to define the modularity of the graph, which we identify with the modularity of this optimal partition, or equivalently the maximal modularity over all partitions \mathcal{C} :

$$\mu = \text{Max}_{\mathcal{C}} \mu(\mathcal{C}). \quad (\text{B2})$$

We then define the community structure of a graph as the partition with this maximal modularity (B2).

Appendix C: Removing one edge

We recall that potentials are solution of $A p = b$, where A is the matrix of conductances and b is the given by the right-hand side of Eq. (2), namely $b = (0, \dots, 0, -\gamma_{I'} p_{I'}, -\gamma_{O'} p_{O'})^T$ (i.e. potentials $p_{I'}$ and $p_{O'}$ are imposed at inlet vertex I' and outlet vertex O' , respectively, see Fig. 7). We now examine the consequence, on the total flow rate Q , of removing one edge from the network. Let us first suppose, without loss of generality, that there is some edge connecting vertices 1 and 2 and that we remove it. Let us denote by A' the matrix Eq. (4) with edge 1-2 removed. The new potentials p'_j in the absence of edge 1-2 are solution of $A' p' = b$.

Matrices A and A' only differ by their upper-left 2×2 corner: the off-diagonal elements are indeed given by $A_{12} = \gamma_{12}$ when edge 1-2 is present, and $A'_{12} = 0$ when it has been removed, while the diagonal elements change from A_{ii} to $A'_{ii} = A_{ii} + \gamma_{12}$. Introducing the column vector u defined by $u^T = \{1, -1, 0, \dots, 0\}$, this can be reexpressed as

$$A' = A + \gamma_{12} u u^T. \quad (\text{C1})$$

Therefore, A' is a rank-one extension of A . The inverse of such a rank-one extension can be obtained from the Sherman-

Morrison formula [37]

$$(A + \gamma_{12}uu^T)^{-1} = A^{-1} - \gamma_{12} \frac{A^{-1}uu^TA^{-1}}{1 + \gamma_{12}u^TA^{-1}u}. \quad (C2)$$

Multiplying both members of this equation by vector b^T on the left and b on the right, we get

$$b^T p' = b^T p - \gamma_{12} \frac{p^T uu^T p}{1 + \gamma_{12}u^TA^{-1}u}, \quad (C3)$$

where $p' = (A + \gamma_{12}uu^T)^{-1}b$ is the solution to the flow equation with edge 1-2 removed. From the definition of u , the scalar product of p and u is $p^T u = p_1 - p_2$. As for the scalar product $b^T p$, we use the fact that $Q = \gamma_{l'}(p_{l'} - p_l) = \gamma_{o'}(p_o - p_{o'}) = \Gamma \delta P$, which leads to

$$\begin{aligned} p_l &= p_{l'} - \frac{\Gamma}{\gamma_{l'}} \delta P \\ p_o &= p_{o'} + \frac{\Gamma}{\gamma_{o'}} \delta P. \end{aligned} \quad (C4)$$

Then, recalling that $\delta P = p_{l'} - p_{o'}$,

$$b^T p = -\gamma_{l'} p_l p_{l'} - \gamma_{o'} p_o p_{o'} \quad (C5)$$

$$= -\gamma_{l'} p_{l'}^2 - \gamma_{o'} p_{o'}^2 + \Gamma (\delta P)^2. \quad (C6)$$

Equation (C3) then directly yields

$$\delta P(Q - Q'_{(12)}) = \frac{\gamma_{12}(p_1 - p_2)^2}{1 + \gamma_{12}[(A^{-1})_{11} + (A^{-1})_{22} - 2(A^{-1})_{12}]}, \quad (C7)$$

where Q'_{12} is the new total flow after removal of edge 1-2.

This equation is exact, and since there is nothing special about vertices 1 and 2, it remains valid for any arbitrary edge removed. Thus, in general, we have

$$\frac{\delta Q_{ij}}{Q} = \frac{\gamma_{ij}}{\Gamma} \frac{1}{t_{ij}} \left(\frac{p_i - p_j}{\delta P} \right)^2, \quad (C8)$$

where $\delta Q_{ij} = Q - Q'_{ij}$, and $t_{ij} = 1 + \gamma_{ij}[(A^{-1})_{ii} + (A^{-1})_{jj} - 2(A^{-1})_{ij}]$ only depends on the network topology and is dimensionless. This equation is homogeneous and leads to Eq. (5).

Appendix D: Typical value of t_{ij}

In this section we want to estimate the typical value of denominators t_{ij} in Eq. (6). We will do so by following a reasoning analogous to the ones in [21, 38]. As we shall see, this reasoning is general and does not depend on the values of the edge conductances γ_{ij} ; we therefore keep them in this Appendix.

As in Appendix C, we consider, without loss of generality, that the edge is between vertices 1 and 2. The corresponding t_{ij} is defined (see Appendix C) as $t_{12} = 1 + \gamma_{12}[(A^{-1})_{11} + (A^{-1})_{22} - 2(A^{-1})_{12}]$. Let $u = (1, -1, 0, \dots, 0)$, and denote by \tilde{p} the solution of the equation $A\tilde{p} = \tilde{b}$, where \tilde{b} is a vector

such that $p + \tilde{p} = p'$. That is, \tilde{p} is the correction that one has to superimpose to the potential p in order to reproduce the solution p' in the absence of edge 1-2. Since we have $A(p + \tilde{p}) = b + \tilde{b}$ and $A'p' = b$, this leads to $\tilde{b} = (A - A')p'$. Recalling that $A' = A + \gamma_{12}uu^T$, we finally get $\tilde{b} = qu$, with $q = \gamma_{12}(p'_2 - p'_1)$.

The solution \tilde{p} thus corresponds to a pressure distribution where an ingoing edge is attached to vertex 1 and an outgoing edge to vertex 2, with an incoming and outgoing flux equal to some value q_0 (see Eq. (3)). For $\tilde{p} \ll 1$, we have $q_0 \simeq q$.

Using the definition of t_{ij} , we then have

$$1 - t_{12} = -\gamma_{12}u^TA^{-1}u = -\frac{\gamma_{12}}{q}u^T \tilde{p} = -\frac{\gamma_{12}}{q}(\tilde{p}_2 - \tilde{p}_1). \quad (D1)$$

If the network is large and homogeneous enough, the solution \tilde{p} can be seen as obtained from the superposition of a current q coming in at vertex 1 and going out at infinity, and a current q coming from infinity and going out at vertex 2. The flux q entering from outside at vertex 1 will spread evenly along the z wires of the graph connected with it, so that each edge, among which edge 1-2, will carry a flux q/z . Similarly the flux outgoing at 2 will create a flux q/z in all edges arriving at 2, in particular the edge from 1 to 2. By superposition, the flux from 1 to 2 will be $\gamma_{12}(\tilde{p}_1 - \tilde{p}_2) = 2q/z$. Thus, using (D1), we get $t_{ij} = 1 - 2/z$. The prefactor in Eq. (6) is then equal to

$$\frac{1}{t_{ij}} = \frac{z}{z-2}, \quad (D2)$$

which, for connectivity $z = 3$, yields a prefactor 3.

Appendix E: Distribution of the logarithm of the flow reduction: asymptotic scaling and position of the maximum

Equation (6) relates the flow variation δQ due to the removal of an edge with flow rate q as $\delta Q = q^2/t$. As mentioned in Section IV, both q and t are distributed according to Cauchy distributions and they may be correlated. However, for large RRGs, we have shown that the Cauchy distribution of t is narrow (Fig. 8), so that we can assume that fluctuations of t are small enough to be neglected compared to flow rate fluctuations. We further assume that the absolute value of q is distributed following the Cauchy distribution $\mathcal{P}(|q|) = \frac{2}{\pi Q_c} \frac{1}{1 + (|q|/Q_c)^2}$ [39], where Q_c is the smallest flow rate characterizing the power law regime.

Replacing t by its median value, we get from Eq. (6)

$$P(\delta Q) = \mathcal{P}(q) \frac{dq}{d\delta Q} \sim \frac{1}{\sqrt{\delta Q}(1 + \delta Q/(3Q_c^2))} \quad (E1)$$

for the distribution of δQ . Setting $X = \ln(\delta Q)$ and recalling that $p(X)dX = P(\delta Q)d\delta Q$, we have

$$p(X) \sim \frac{e^{X/2}}{1 + e^X/(3Q_c^2)}, \quad (E2)$$

and thus

$$\ln p(X) = a + \frac{X}{2} - \ln \left(1 + \frac{e^X}{3Q_c^2} \right), \quad (\text{E3})$$

where a is some constant that accounts for the prefactor in (E2). At small values of δQ we have $X \rightarrow -\infty$ and therefore the scaling behaviour

$$\ln p(X) \simeq a + \frac{X}{2}. \quad (\text{E4})$$

At large values of δQ we get

$$\ln p(X) \simeq a' - \frac{X}{2}, \quad (\text{E5})$$

with a' some constant. Besides, the root of the derivative of Eq. (E2) yields the maximum of the distribution p for $\widehat{\delta Q} = 3Q_c^2$. Finally, in the limit of large sizes, RRGs of connectivity 3 with one additional inlet and outlet behave like the union of two balanced binary trees of equal height H [37], with roots corresponding to the inlet and outlet. Thus, we have $N = 2(2^H - 1) - N_l$, $N_l = 2^{(H-1)}$ corresponding to the number of leaves that merge to connect the two trees. For such a graph, the distribution of absolute flow rate is fully described by the power-law regime, so that Q_c is equal to the lowest value of the distribution, i.e. in the graph leaves. As a result, $Q_c = Q/N_l$. Combining these two equations leads to $Q_c = 3Q/(N+1)$, so that, in the limit of large sizes, $\widehat{\delta Q}$ scales as $1/N^2$.

-
- [1] N. Korte, R. Nortley and D. Attwell, Cerebral blood flow decrease as an early pathological mechanism in Alzheimer's disease. *Acta Neuropathol.* 140 (2020) 793–810. <https://doi.org/10.1007/s00401-020-02215-w>
 - [2] M. Cortes-Canteli and C. Iadecola, Alzheimer's Disease and Vascular Aging, *Journal of the American College of Cardiology* 75 (2020) 942–951. <https://doi.org/10.1016/j.jacc.2019.10.062>.
 - [3] C. Iadecola, The Pathobiology of Vascular Dementia. *Neuron* 80 (2013) 844–866.
 - [4] S. Dong, S. Maniar, M.D. Manole and D. Sun. Cerebral hypoperfusion and other shared brain pathologies in ischemic stroke and Alzheimer's disease *Translational Stroke Research* 9 (2018), 238–250.
 - [5] C. Iadecola, The overlap between neurodegenerative and vascular factors in the pathogenesis of dementia. *Acta Neuropathologica* 120 (2010), 287–296.
 - [6] Y. Iturria-Medina, R. C. Sotero, P. J. Toussaint, J. M. Mateos-Pérez and A. C. Evans, The Alzheimer's Disease Neuroimaging, Early role of vascular dysregulation on late-onset Alzheimer's disease based on multifactorial data-driven analysis. *Nat Commun* 7 (2016) 11934.
 - [7] J. C. Cruz Hernández, O. Bracko, C. J. Kersbergen, V. Muse, M. Haft-Javaherian, M. Berg, L. Park, L. K. Vinarsik, I. Ivasyk, D. A. Rivera, Y. Kang, M. Cortes-Canteli, M. Peyrounette, V. Doyeux, A. Smith, J. Zhou, G. Otte, J. D. Beverly, E. Davenport, Y. Davit, C. P. Lin, S. Strickland, C. Iadecola, S. Lorthois, N. Nishimura and C. B. Schaffer, Neutrophil adhesion in brain capillaries reduces cortical blood flow and impairs memory function in Alzheimer's disease mouse models. *Nature Neuroscience* 22(3) (2019) 413–420.
 - [8] R. Nortley, N. Korte, P. Izquierdo, C. Hirunpattarasilp, A. Mishra, Z. Jaunmuktane, V. Kyrargyri, T. Pfeiffer, L. Khennouf, C. Madry, H. Gong, A. Richard-Loendt, W. Huang, T. Saito, T. C. Saido, S. Brandner, H. Sethi and D. Attwell, 2019. Amyloid β oligomers constrict human capillaries in Alzheimer's disease via signaling to pericytes. *Science* 365 (2019) eaav9518.
 - [9] P. Blinder, P. S. Tsai, J.P. Kaufhold, P.M. Knutsen, H. Suhl and D. Kleinfeld, The cortical angiome: an interconnected vascular network with noncolumnar patterns of blood flow, *Nature Neuroscience* 16 (2013) 889–897.
 - [10] A. Hahn, J. Bode, T. Krüwel, G. Solecki, S. Heiland, M. Bendzus, B. Tews, F. Winkler, M.O. Breckwoldt and F.T. Kurz, Glioblastoma multiforme restructures the topological connectivity of cerebrovascular networks. *Sci. Rep.* 9 (2019) 11757.
 - [11] S. Fortunato and C. Castellano, Community Structure in Graphs, Chapter of Springer's *Encyclopedia of Complexity and System Science*, Springer, 2007.
 - [12] S. Fortunato, Community detection in graphs, *Phys. Rep.* 486 (2010) 75–174.
 - [13] J. S. Coleman, Introduction to mathematical sociology (1964).
 - [14] L. Freeman, The development of social network analysis, *A Study in the Sociology of Science* 1 (2004) 687.
 - [15] Y. Dourisboure, F. Geraci and M. Pellegrini, Extraction and classification of dense communities in the web, In *Proceedings of the 16th international conference on World Wide Web* (2007), 461–470.
 - [16] G.W. Flake, S. Lawrence, C. L. Giles and F. M. Coetzee, Self-organization and identification of web communities, *Computer* 35(3) (2002) 66–70.
 - [17] N. C. Wormald, Models of random regular graphs, *London Mathematical Society Lecture Note Series* (1999) 239–298.
 - [18] P. S. Tsai, J. P. Kaufhold, P. Blinder, B. Friedman, P. J. Drew, H.J. Karten, P.D. Lyden and D. Kleinfeld, 2009. Correlations of Neuronal and Microvascular Densities in Murine Cortex Revealed by Direct Counting and Colocalization of Nuclei and Vessels. *Journal of Neuroscience* 29 (2009) 14553–14570.
 - [19] A. F. Smith, V. Doyeux, M. Berg, M. Peyrounette, M. Haft-Javaherian, A.-E. Larue, J. H. Slater, F. Lauwers, P. Blinder, P. Tsai, D. Kleinfeld, C. B. Schaffer, N. Nishimura, Y. Davit and S. Lorthois, Brain capillary networks across species: a few simple organizational requirements are sufficient to reproduce both structure and function. *Front. Physiol.* 10 (2019) 233
 - [20] A. G. Hudetz, Percolation Phenomenon: The Effect of Capillary Network Rarefaction. *Microvascular Research* 45 (1993) 1–10. <https://doi.org/10.1006/mvre.1993.1001>.
 - [21] C. Pozrikidis, On the performance of damaged linear networks. *J. Appl. Math. Comput.* 39 (2012) 489–510. <https://doi.org/10.1007/s12190-012-0540-5>.
 - [22] A. L. Barabási and R. Albert, *Science* 286 (1999) 509–512.
 - [23] S. Boccaletti, V. Latora, Y. Moreno, M. Chavez and D. U. Hwang, Complex networks: Structure and dynamics, *Phys. Rep.* 424 (4-5) (2006) 175–308.
 - [24] S. N. Dorogovtsev and J. F. F. Mendes, *Evolution of Networks*, Oxford University Press, Oxford (2003).
 - [25] B. Bollobas, *Random graphs*, Cambridge studies in advanced Mathematics 73 (2001) 264–267.
 - [26] R. Albert and A.-L. Barabási, Topology of Evolving Networks: Local Events and Universality, *Phys. Rev. Lett.* 85 (2000) 5234–

- 5237.
- [27] S. N. Dorogovtsev, J. F. F. Mendes and A.N. Samukhin, Principles of statistical mechanics of uncorrelated random networks, *Nuclear Physics B* 666 (3) (2003) 396-416.
- [28] J. H. Kim and V. H. Vu, Generating random regular graphs, in : Proceedings of the thirty-fifth annual ACM symposium on Theory of computing, (2003) 213-222.
- [29] J. Nguyen, N. Nishimura, R. N. Fetcho, C. Iadecola, C. B. Schaffer, Occlusion of Cortical Ascending Venules Causes Blood Flow Decreases, Reversals in Flow Direction, and Vessel Dilation in Upstream Capillaries, *Journal of Cerebral Blood Flow and Metabolism* 31 (2011) 2243-2254.
- [30] S. N. Dorogovtsev, A. V. Goltsev, J. F. F. Mendes, and A. N. Samukhin, Spectra of complex networks, *Phys. Rev. E* 68 (2003) 046109.
- [31] N.C. Wormald, The asymptotic connectivity of labelled regular graphs, *J. Comb. Theory, Ser. B* 31 (1981) 156-168.
- [32] S. Lorthois and F. Cassot, Fractal analysis of vascular networks: Insights from morphogenesis. *Journal of Theoretical Biology* 262 (2010) 614-633. <https://doi.org/10.1016/j.jtbi.2009.10.037>
- [33] M. E. J. Newman and M. Girvan, Finding and evaluating community structure in networks, *Phys. Rev. E* 69 (2004) 026113.
- [34] S. Lorthois, Blood suspension in a network, in: Viallat, A., Abkarian, M. (Eds.), *Dynamics of Blood Cell Suspensions in Microflows*. CRC Press, Boca Raton: CRC Press (2020) 257-286. <https://doi.org/10.1201/b21806-8>
- [35] E. Bogomolny and O. Giraud, Calculation of mean spectral density for statistically uniform tree-like random models, *Phys. Rev. E* 88 (2013) 062811.
- [36] R. Abou-Chakra, D. J. Thouless and P. W. Anderson, A self-consistent theory of localization, *Journal of Physics C: Solid State Physics* 6 (1973) 1734-1752.
- [37] E. C. Weisstein, *CRC concise encyclopedia of mathematics*, (1988) CRC Press.
- [38] S. Kirkpatrick, Percolation and Conduction, *Rev. Mod. Phys.* 45 (1973) 574-588.
- [39] F. Goirand, Statistical modelling of blood flow and transport in brain micro-vascular networks, PhD Thesis to be defended May 2021, Toulouse University.
- [40] F. Schmid, G. Conti, P. Jenny and B. Weber. The severity of microstrokes depends on local vascular topology and baseline perfusion. Preprint, Biorxiv (doi.org/10.1101/2020.07.05.188565).
- [41] A.R. Pries, T.W. Secomb and P. Gaehtgens, Biophysical aspects of blood flow in the microvasculature. *Cardiovascular research* 32 (1996) 654-667.
- [42] T.W. Secomb, Blood Flow in the Microcirculation. *Annual Review of Fluid Mechanics* 49 (2017), 443-461.
- [43] A. Y. Shih, J. D. Driscoll, P. J. Drew, N. Nishimura, C. B. Schaffer and D. Kleinfeld, Two-Photon Microscopy as a Tool to Study Blood Flow and Neurovascular Coupling in the Rodent Brain. *Journal of Cerebral Blood Flow and Metabolism* 32 (2012) 1277-1309.
- [44] C. Kirst, S. Skriabine, A. Vieites-Prado, T. Topilko, P. Bertin, G. Gerschenfeld, F. Verry, P. Topilko, N. Michalski, M. Tessier-Lavigne, N. Renier, 2020. Mapping the Fine-Scale Organization and Plasticity of the Brain Vasculature, *Cell* 180 (2020) 780-795 <https://doi.org/10.1016/j.cell.2020.01.028>
- [45] M. D'Esposito, L. Y. Deouell, A. Gazzaley, Alterations in the BOLD fMRI signal with ageing and disease: a challenge for neuroimaging. *Nature Reviews Neuroscience* 4 (2003) 863-872. <https://doi.org/10.1038/nrn1246>
- [46] A. Y. Shih, C. Rühlmann, P. Blinder, A. Devor, P. J. Drew, B. Friedman, P. M. Knutsen, P.D. Lyden, C. Matéo, L. Melander, N. Nishimura, C. B. Schaffer, P. S. Tsai, D. Kleinfeld, Robust and fragile aspects of cortical blood flow in relation to the underlying Angioarchitecture. *Microcirculation* 22 (2015) 204-218.
- [47] N. Nishimura, C.B. Schaffer, B. Friedman, P.D. Lyden, D. Kleinfeld, Penetrating arterioles are a bottleneck in the perfusion of neocortex. *Proceedings of the National Academy of Sciences* 104 (2007) 365-370.
- [48] N. Nishimura, C.B. Schaffer, B. Friedman, P.S. Tsai, P.D. Lyden, D. Kleinfeld, Targeted insult to subsurface cortical blood vessels using ultrashort laser pulses: three models of stroke. *Nature Methods* 3 (2006) 99-108.
- [49] A. Y. Shih, P. Blinder, P.S. Tsai, B. Friedman, G. Stanley, P.D. Lyden, D. Kleinfeld. The smallest stroke: occlusion of one penetrating vessel leads to infarction and a cognitive deficit. *Nature Neuroscience* 16 (2012) 55-63.
- [50] M. El Amki, C. Glück, N. Binder, W. Middleham, M.T. Wyss, T. Weiss, H. Meister, A. Luft, M. Weller, B. Weber and S. Wegener, Neutrophils obstructing brain capillaries are a major cause of no-reflow in ischemic stroke. *Cell Reports* 33 (2020), 108260.
- [51] R. Albert and A. L. Barabási, Statistical mechanics of complex networks, *Rev. Mod. Phys.* 74 (2002) 47-97.
- [52] P. Erdős and A. Rényi, On Random Graphs, *Publicationes Mathematicae, Debrecen* 6 (1959) 290-297 (1959).
- [53] P. Erdős and A. Rényi, On the evolution of random graphs, *Publ. Math. Inst. Hung. Acad. Sci.* 5 (1960) 17-60.
- [54] Following [9], the upper-limit corresponds to homogeneous space-filling networks. For such networks in 3D, the number of edges in cubic regions with side L scales as L^3 , while the number of edges connecting it region to the rest of the network scales as L^2 . As a result, a power-law with exponent $2/3$ is obtained for the number of inter-versus intra-community edges. This exponent is $1/2$ in 2D and 1 in infinite dimension.
- [55] Note that it would also have been possible to choose the number of rewirings that matches the modularity $\mu_{\gamma} \sim 0.827$ of the Voronoi graph. From the main panel of Fig. 6, this would correspond to taking 70 rewirings.
- [56] Note that if all $\gamma_{ij} = 1$, then A is simply the adjacency matrix of the graph, to which we add the diagonal elements $-z_i \delta_{ij}$, for $1 \leq i, j \leq N$, where z_i is the connectivity of vertex i .
- [57] This definition of δQ_0 is equivalent as translating all distributions of the above panel of Fig. 10 by $-(8720/1176)^2$, consistent with the size dependence obtained for RRGs in appendix E.

4.3 Successive occlusions

In the previous section, we have laid the foundation of a generalized dilute regime formalism able to account for both the topological particularities and flow organization of brain micro-vascular networks (Eq. (9) for networks with unit vessel conductance and Eq. (C8) for the general case). However, this study was limited to the removal of a single edge. In the following, our objective is to unravel the different contributions of brain micro-vascular network heterogeneities in the context of multiple occlusions. To do so, we investigate the evolution of the flow properties during this occlusion process in model networks with controlled degrees of heterogeneity.

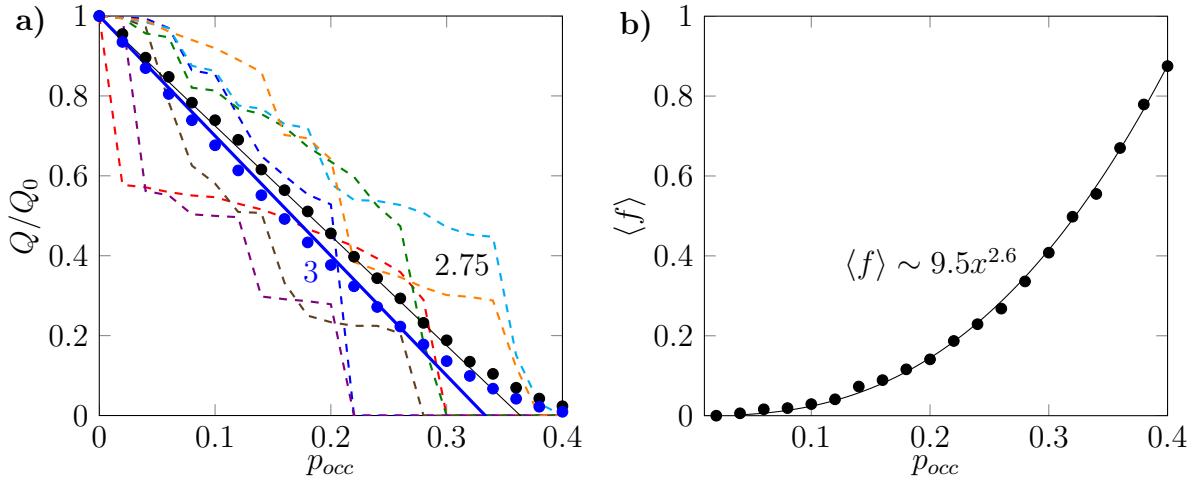


Figure 4.2: **Percolation analysis performed on a bio-mimetic capillary bed with dipolar boundary conditions shows that the flow organization not only affects fluctuations of the flow reduction but also the average decrease and disconnection probability.** **a)** Evolution of the average inlet flow rate decrease with dipolar boundary conditions obtained for 500 realizations (black dots) and with fixed pressure drop applied on two opposite faces (blue dots). Inlet flow decrease associated to different progressive occlusion realizations with dipolar configuration of sources: each occlusion increment is added with memory of the previous ones (thin colored dashed lines). Linear fit $y = 1 - 2.75x$ (black line). Effective medium prediction of Eq. (4.1) (thick blue line). **b)** Disconnection probability (black dots). Power-law fit $y = 9.5x^{2.6}$.

Impact of flow organization Here, the study is performed on a bio-mimetic capillary bed [8] with dipolar injection, i.e. flow is injected and pumped by and from only two edges with low topological distance at the network surface. This network has been chosen for this study as it allows to easily manipulate the boundary conditions with fixed topological structure. Fig. 4.2a shows that the large fluctuations highlighted in the previous section persist for successive occlusions. Interestingly, the computed average differs slightly from the effective medium prediction of Eq. (4.1): the computed slope in the linear regime is found to be equal to 2.75 instead of 3. This deviation cannot be explained by the topology of the bio-mimetic network as it does not appear while performing the percolation analysis on this network with fixed pressure drop applied on two opposite faces¹ (see Fig. 3.1 for an illustration of the organization of the pressure field in such conditions). Moreover, the average fraction of disconnected inlets, which is equivalent to the

¹This configuration of boundary conditions corresponds to the one applied in [80] in order to perform the percolation analysis.

percolation probability in the case of a single input, shows a different scaling law from [80]. Here, the probability to break the flow increases non-linearly since the first percentages of occlusions (Fig. 4.2b).

Impact of micro-vascular network topology As a second step of this study, we reproduce the above analysis with a model network only accounting for the micro-vascular topology. To do so, we impose the inlet and outlet pressures on one arteriole and one venule randomly chosen among the 14 arterioles and 28 venules. We also set all the conductances at the same value. In addition, contrary to the analysis performed in the preliminary section where only capillaries were occluded, here, all vessels can be occluded including arterioles and venules. As expected, the flow decrease is still submitted to large fluctuations (Fig 4.3a). More interestingly, the micro-vascular topology induces an increased robustness to flow decrease in the first occlusion percentages compared to bio-mimetic networks (Fig 4.3a). The flow decrease exhibits two different linear decays characterized respectively by a first slope of 2.17 and a second slope, identical to the previous study on bio-mimetic networks, of 2.75. This change in slope is located around 20% of occlusions (Fig 4.3a). As this break in slope was not present in the previous analysis, we can assert that it is a consequence of a topological difference between micro-vascular networks and bio-mimetic networks. Bio-mimetic networks only mimicking the capillary bed, we could see here the impact of the composite nature of micro-vascular networks: tree-like arterioles and venules and mesh-like capillary bed. Here, the disconnection probability does not change fundamentally and sees only small parametric corrections (Fig. 4.3b).

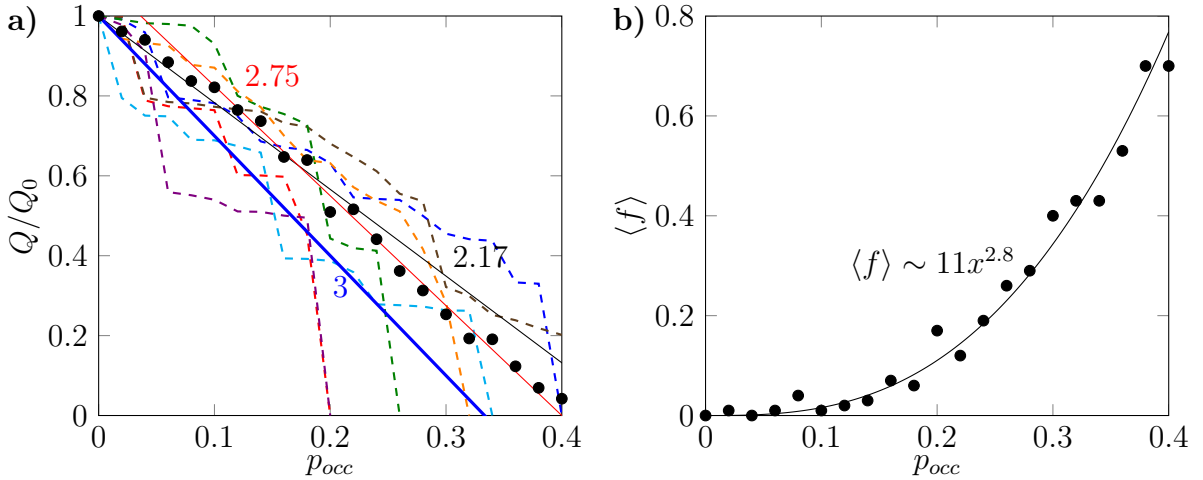


Figure 4.3: **Percolation analysis on the mouse micro-vascular networks displayed in Fig. 5 or Fig. S1 of Chapter 2 with only one inlet and outlet and uniformized conductances highlights a change in slope around $p_{occ} = 20\%$ delimiting a regime of increased flow robustness for a low percentage of occlusions.** **a)** Evolution of the average inlet flow rate decrease (black dots). Linear fit $y = 1 - 2.17x$ (black line). Linear fit $y = 1.1 - 2.75x$ (red line). Effective medium prediction of Eq. (4.1) (thick blue line). **b)** Disconnecting probability (black dots). Power-law fit $y = 11x^{2.8}$ (black line).

Impact of multiple inlets/outlets As a third step of this study, we start from the previous configuration but now allowing all arterioles and venules to perfuse and drain the micro-vasculature. Fig. 4.4a shows a drastic decrease of the fluctuations around the computed average.

On the other hand, the two regime decay remains and the value of the associated slopes slightly decreases, 1.9 for the first regime and 2.6 for the second and the value of the transition between the two regimes appears to slightly increase. Moreover, the scaling law associated to the fraction of disconnected arterioles sees no drastic changes except the value of its pre-factor which goes from 11 to 6 (Fig. 4.4a). However, even if the individual disconnection probability does not much vary with the addition of all inlets/outlets, the addition of multiple inlets and outlet considerably increase the flow resilience at the scale of the network. This can be emphasized by a simple first order evaluation of the total disconnection probability, i.e. the probability to observe a zero flow at every inlets, by $\langle f \rangle^{n_A}$, where n_A is the number of inlets in the system. With $n_A = 14$ in our micro-vascular networks, the total disconnection probability can be estimated to be about 10^{-5} for 40% of occlusions. As a comparison, the percolation threshold is at about 40% of missing bonds in bio-mimetic networks with boundary conditions classically used in percolation analysis (Fig. 4.1a). This result is quite interesting. It suggests that despite of the low resilience of the flow with a unique dipolar configuration of sources, the increase in inlets/outlets number considerably strengthens the flow resilience to an extent that it becomes more resilient than a flow induced by boundary conditions classically used in percolation theory. The fact the multi-dipole configuration of sources is precisely the one that appears in the brain micro-circulation can lead us to think that this configuration has emerged from an evolutionary process tending to optimize blood flow resilience in this vital organ.

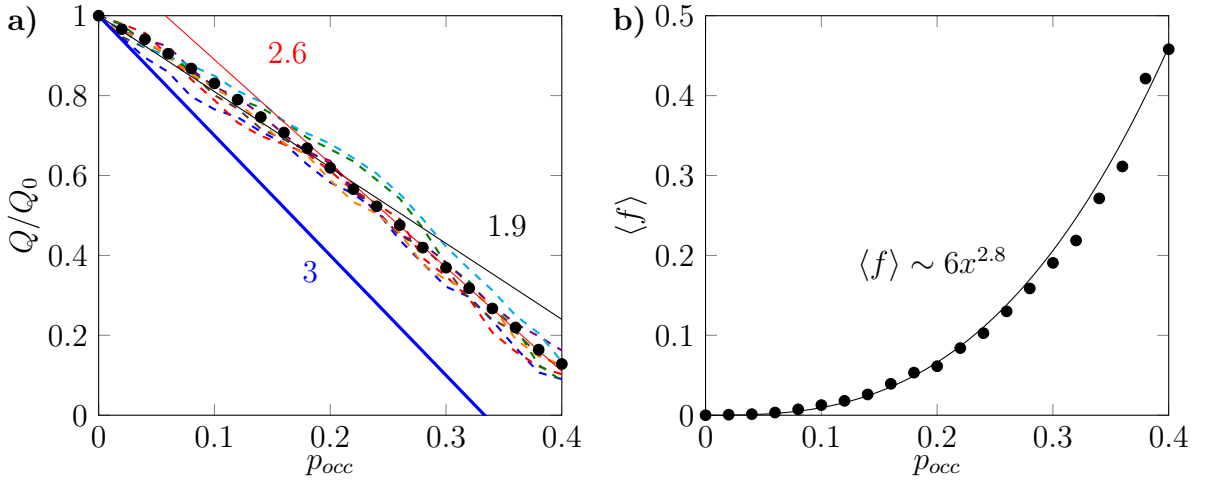


Figure 4.4: **Percolation analysis on micro-vascular network with all arterioles and venules and uniformized conductances displays a drastic decrease of flow decrease fluctuations.** **a)** Evolution of the average inlet flow rate decrease (black dots). Linear fit $y = 1 - 1.9x$ (black line). Linear fit $y = 1.1 - 2.6x$ (red line). Effective medium prediction of Eq. (4.1) (thick blue line). **b)** Average fraction of disconnected arterioles (black dots). Power-law fit $y = 6x^{2.8}$ (black line).

Impact of restraining the occlusion process to the capillary bed Until there, in this section, we have performed the occlusion process independently of the vessel type. However, as stated in the Preliminary Section, the occlusions that are suspected to trigger Alzheimer's disease occur in the capillary bed. In this ultimate analysis, starting from the last configuration, we now bias the occlusion process to occur uniquely within the capillary bed. The idea underlying this procedure is to see if the arterioles and venules can create topological unalterable paths reinforcing

the global flow resilience to random occlusions. Unfortunately, restraining the occlusion process to the capillary bed only leads to an other slight parametric correction of the previous scaling laws (Fig. 4.5). Nevertheless, by comparison to Fig. 4.1, this result indicates that something relevant to understand cerebral blood flow decrease induced by capillary occlusion was neglected in this study: the conductance heterogeneity. In the light of this ultimate analysis, it seems clear that arterioles and venules as highly conductive trees are in themselves an element of robustness, preventing the emergence of the second decay regime and decreasing significantly the probability to see an inlet disconnected.

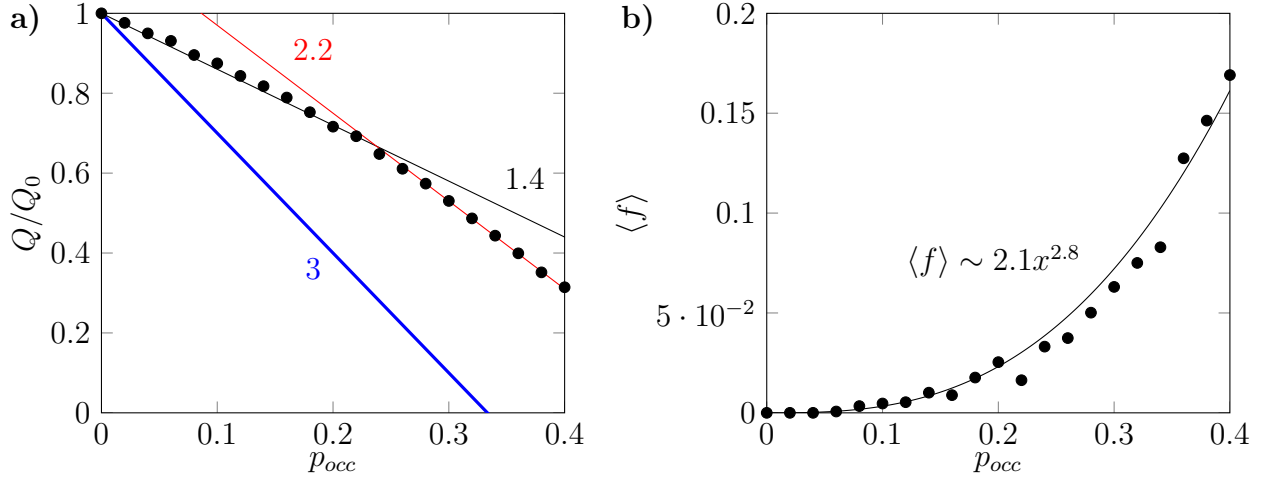


Figure 4.5: **Percolation analysis restrained on the capillary bed of micro-vascular networks with uniformized conductances shows only parametric corrections to the previous results.** **a)** Evolution of the average inlet flow rate decrease (black dots). Linear fit $y = 1 - 1.4x$ (black line). Linear fit $y = 1.1 - 2.2x$ (red line). Effective medium prediction of Eq. (4.1) (thick blue line). **b)** Average fraction of disconnected arterioles (black dots). Power-law fit $y = 2.1x^{2.8}$ (black line).

To conclude this section, we recap the key points of this study:

- The dipole flow organization not only produces large fluctuations around the average flow reduction as shown in Section 2, but also modifies the average flow reduction in itself and the percolation probability expected by classical results on percolation on lattices.
- The topological structure of micro-vascular networks induces a two linear regime decay separated by a change in slope for about 20% of occlusions. This peculiar behaviour is probably induced by the composite nature of micro-vascular networks connecting tree-like arterioles and venules with mesh-like capillary bed.
- The presence of multiple inlets and outlets, i.e. arterioles and venules, considerably increases the resilience of the flow to occlusions by reducing the fluctuations of inlet flow decrease and total disconnection probability. This may suggest the presence of a passive flow compensatory mechanism between arterioles (or venules) in the case of a flow decrease in a neighbouring one.
- At the cost of a slightly steeper decrease of the first decay regime, high arteriolar and venular conductances create preferential and unalterable paths decreasing drastically the

fraction of disconnected arterioles and allowing to prevent the emergence of the second linear decay regime of inlet flow reduction, in the context of capillary occlusions. As a consequence, arterioles and venules play an important role in blood flow resilience in brain micro-circulation.

4.4 Perturbations induced by capillary occlusions

In percolation theory, the question of the quantification of the local perturbation of the flow induced by edge removals is rarely addressed. However, in the context of biological systems, and here brain micro-vascular networks, the flow is oftenly coupled to (bio-)chemical reactions. Given that (bio-)chemical reactions have their own kinetics, flow kinetics should be compatible with reaction kinetics in order to let the time for the reaction to settle but, at the same time, to avoid stagnation points. In that extent, transport in biological media should satisfy a certain kind of optimality criterion [122]. In this brief section, such local flow perturbations are investigated by computing their statistics across two networks with different boundary conditions: the mouse micro-vascular network with occlusions in the capillary bed and the bio-mimetic capillary bed with fixed pressure drop applied on two opposite faces. The use of two different networks with different flow organizations aims to test the potential independence of these flow perturbations on the network topology and flow organization. This analysis is performed for low fraction of occlusions (1%, 5% and 10%) where the dilute regime of percolation applies. Furthermore, the perturbation statistics are obtained by performing averages on 10 realizations in order to limit the impact of the inlet flow fluctuations that have been highlighted in the previous section. Hence, we define δq_0^i is the perturbation of the initial flow of edge i as follows:

$$\delta q_0^i = \frac{q^i}{q_0^i(1 - \alpha p_{occ})} \quad (4.2)$$

where α is the slope of the linear decay corresponding to the studied range of occlusions, q^i is the flow of edge i after the occlusion of a fraction p_{occ} of vessels. As shown in Eq. (4.2), we make discard the linear tendency from the computation of the flow perturbation. Finally, we define $p_{\delta q_0}$, the probability density function of the above local flow perturbations.

Fig. 4.6 shows the large perturbations of the flow in the shape of a Cauchy distribution, independently of the applied boundary conditions and the considered network. The emergence of such Cauchy distributions is not surprising in the light of this thesis work. In Appendix D of Section 2, we indeed showed that occlusions, or edge removals, were equivalent to introducing a potential correction at each node of the removed edges in order to produce flow correction of same magnitude and opposite direction within the removed edges (Eq. (D1)). This configuration closely corresponds to the dipole flow. Further, we have shown that this dipole flow configuration induces a Cauchy law distribution on networks (see Section 1 of Chapter 2).

The fraction of vessels perturbed by the introduction of occlusions can be obtained by the computation of the integral of the Cauchy distribution. This integral is found to evolve non-linearly with the fraction of occluded vessels highlighting the long range of the perturbations induced by capillary occlusions. Fig. 4.6 shows that the integral of the Cauchy distribution is approximately equal to 8%, 26% and 40% respectively for 1%, 5% and 10% of occlusions in the bio-mimetic network and to 7%, 23% and 33% respectively for 1%, 5% and 10% of occlusions in the micro-vascular networks.

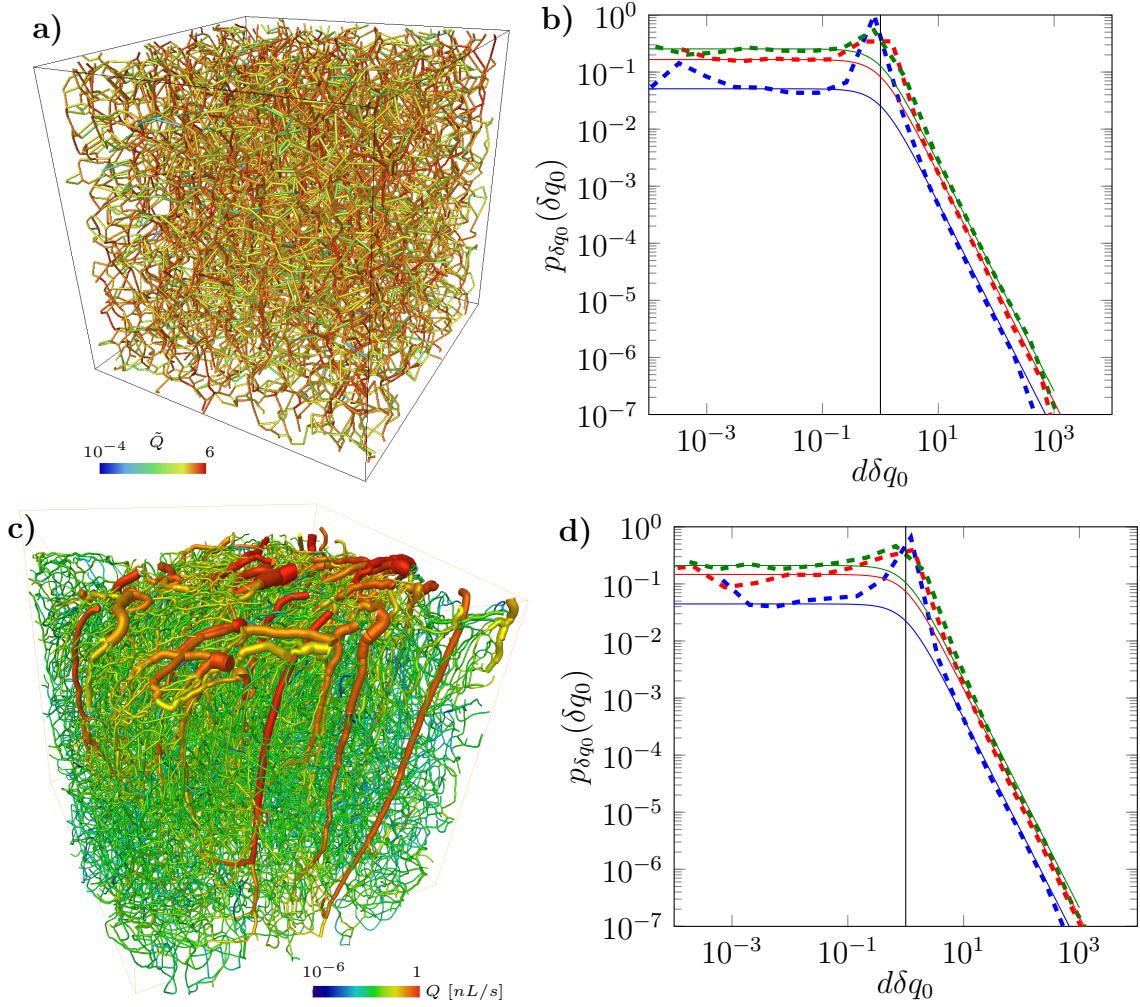


Figure 4.6: **Random occlusions in flow networks induce broadly distributed flow perturbations in the shape of a Cauchy distribution independently of network topology and flow organization.** **a-b)** Flow distribution in bio-mimetic capillary networks with fixed pressure drop applied on two opposite faces and the associated probability density functions of perturbation statistics induced by vessel occlusion (dashed line). Cauchy fits with integral 0.08 (blue full line), 0.26 (red full line) and 0.40 (green full line). **c-d)** Flow distribution in microvascular networks with anatomically realistic boundary conditions and the associated probability density functions of perturbation statistics induced by capillary occlusion (dashed line). Cauchy fits with integral 0.07 (blue full line), 0.23 (red full line) and 0.33 (green full line). In **b)** and **d)**, blue, red and green respectively label the results for 1%, 5% and 10% of occluded vessels.

Quantitatively, it appears that there is a little dependency on the flow organization or/and the network topology but this has to be investigated with more accuracy, performing for example a systematic analysis of this Cauchy law integral, to provide a definitive conclusion. This difference might be linked to the factors of flow robustness that we have highlighted in the previous Section. Given that asymptotic scalings for the Cauchy distribution are a uniform distribution and a power law with exponent -2 (see Section 1 of Chapter 2), we can easily compute the fraction of vessels

which are submitted to large flow perturbations, $\delta q_0 < 0.1$ and $\delta q_0 > 10$:

$$\begin{cases} f(\delta q_0 < 0.1) = \frac{2C(p_{occ})}{\pi} \int_0^{0.1} d\delta q_0 = 0.1 \frac{2C(p_{occ})}{\pi} \\ f(\delta q_0 > 10) = \frac{2C(p_{occ})}{\pi} \int_{10}^{\infty} (\delta q_0)^{-2} d\delta q_0 = 0.1 \frac{2C(p_{occ})}{\pi} \end{cases} \quad (4.3)$$

where $C(p_{occ})$ is the Cauchy integral.

With this quick estimation, we can conclude that beyond inducing a break in the flow at their location, occlusions induce large fluctuations to a fraction of vessels of the same order of magnitude than the fraction of occluded vessels themselves. This mechanism reinforces all the more the detrimental consequences of capillary occlusions on cerebral blood flow and metabolism.

4.5 Conclusion and perspectives

In this section, we investigated the global flow decrease in brain micro-vascular networks induced by occlusions of capillary vessels. Motivated by the observation of a linear decrease of the global flow, in average, with the increase in the fraction of occluded vessels until 20% [21], we have adopted the point of view of percolation on networks, which predicts such type of linear decrease for the considered range of occlusion fractions. However, both the topology of the micro-vasculature and the resulting organization of the blood flow have been found to produce a new phenomenology poorly investigated to the best of our knowledge by state of the art theories. These sources of complexity have led us to develop novel approaches to describe accurately the mechanism leading to the emergence of these new properties. Hence, we have laid the foundation of a generalized framework to study the dilute regime of percolation with non-trivial flow organization and network topological structures. Within this framework, we have notably unveiled that the flow reduction induced by a single occlusion has a quadratic dependence on the flow initially present in the vessel and is inversely proportionnal to a topological term. We have shown that this topological term is sensitive to the presence of a community structure in networks. In particular, for micro-vascular networks, this topological term is distributed according to a Cauchy law, increasing the probability to observe large flow reductions compared to networks with no underlying community structure.

Next, we have performed a quantitative study of the influence of different sources of complexity present in the micro-vascular structure on the global flow decrease and the probability to disconnect a micro-vascular inlet, or arteriole, for successive occlusions. In particular, in this second part, we have focused on the impact of, on one hand, the composite nature of the micro-vasculature which is made of highly conductive and heterogeneous tree-like structures connected by homogenous mesh-like networks, and, on the other hand, the large density of inlets and outlets. Unfortunately, all these particularities do affect, at least parametrically, the global flow decrease and the arteriole disconnection probability. However, more interestingly, some elements appear to be invariant. First, the dipole flow organization induces a power law evolution of the inlet disconnection probability since the very first percentages of occlusions. Secondly, in agreement with the results presented in Section 2, such flow organization generates large fluctuations of the flow decrease around a linear average trend. Thirdly, the observed transition in the decay of the global flow decrease in micro-vascular networks for about 20% of occlusions is undoubtedly a consequence of the peculiar topological structure of the micro-vascular networks. Fourthly, the presence of multiple inlets and outlets, without changing significantly the inlet disconnection

probability, drastically reduces the global flow decrease fluctuations around the computed average. Finally, we have shown that vessel occlusions induce large perturbations of the flow within a fraction of vessels comparable to the fraction of occluded vessels.

Overall, the study presented in this chapter emphasizes that beyond on site break in the flow, capillary occlusions exhibit at least two other major detrimental consequences: the decrease of the global flow and the large perturbations of the flow within a fraction of vessels of the same order than the fraction of effectively occluded vessels. The percolation framework that we have developed in order to describe the impact of a single occlusion on blood flow organization in Section 2 is only the first step in the way to model the impact of multiple vessel occlusions on brain micro-vascular networks with their full complexity. The fact that the average global flow decrease in the dilute regime, as shown in Section 3, is still linear while increasing the complexity is a good sign that our framework can be extended. Within this framework, it could be notably interesting to describe the mechanisms that lead to the drastic decrease of global flow fluctuations in the presence of multiple inlets and outlets. Such a description could importantly benefit to the understanding of potential compensatory mechanisms ensuring an increased resilience of the blood flow supply to brain cells. Moreover, performing a purely topological percolation analysis, i.e. focusing on the size and number of connected components, on the micro-vascular networks could provide information on the mechanism that leads to the observed transition around 20% of occlusions in the decay of the global flow. This transition has been shown to induce a discontinuous change in slope in micro-vascular networks with uniform conductances. This may indicate the presence of a topological first order phase transition [136] at this fraction of occlusions with potential disconnection of large scale vessel clusters. This should be investigated in the future by the study, for instance, of the evolution of the distribution of disconnected cluster sizes. It would be interesting to perform this study in comparison to the study that we have led in this thesis on the community structure of micro-vascular networks. Conjointly, it seems appropriate to investigate more precisely why this sharp transition in micro-vascular networks with uniform conductances is avoided in anatomical micro-vascular networks. This could be a clue to progress on the understanding of the role of arterioles and venules on network robustness and/or flow resilience [118] and consequently on the understanding of the physical mechanism linking micro-vascular occlusions to cognitive dysfunction.

To conclude this chapter, we stress on a critical point of this study. In Alzheimer's disease, occlusions have been shown to be mediated by White Blood Cell (WBC) adhesion on vessel walls. In that extent, occlusions result from a dynamical process directly induced by the micro-vascular transport properties in themselves. Consequently, WBC can potentially only occlude vessels with non-zero flow rate. This defines a conceptual framework slightly different from the classical percolation approach where edges can be removed independently of their flow value. In that extent, the percolation analysis presented above could consist in a lower bound of the effective impact of occlusions in the micro-circulation [137]. This remark invites potentially to treat WBC mediated occlusions on a dynamical point of view rather than on a static one to account for the consecutive re-organization of the flow after each occlusion. More generally, whether the occlusion process is tackled from a dynamical or static point of view, it could be refined by considering some correlations between the spatial location of occlusions or weighting the occlusion probability by a coefficient accounting for the local flow magnitude or/and vessel diameter.

Chapter 5

General conclusion and perspectives

Blood circulation supplies organs with vital chemical species, e.g oxygen and nutrients, maintains the physiological constants at their optimal value and removes metabolic waste. Brain perfusion is mediated at the cellular scale by a system of small vessels whose diameters range from a few to hundred microns: the micro-vascular networks. These micro-vascular networks have a composite structure including tree-like supplying and draining networks, known respectively as arterioles and venules, connected together by a space-filling network: the capillary bed. Beyond maintaining physiological constants, brain micro-vascular networks have been shown to play an active role in the regulation of the cerebral blood flow in order to match the increase of the metabolic demand induced by brain activation. This mechanism is called neuro-vascular coupling.

Despite of the essential role of blood flow in making neurons thrive and in preserving neuronal life as much as possible under pathological stress, its organization at the micro-vascular scale is poorly understood. The first elements of description of blood flow organization in micro-vascular networks have emerged only recently principally thanks to the improvement of imaging techniques. Such techniques allow direct measurements of hemodynamic quantities, e.g. Red Blood Cell velocities, but also imaging the micro-vascular network structure, which enable to perform realistic blood flow simulations on anatomically accurate networks. On a medical point of view, some of these imaging techniques, while offering poor spatial resolutions, have turned out to be of a great help in the understanding of cerebral pathologies. Hence, for instance, functional Magnetic Resonance Imaging (fMRI) and Positron Emission Tomography (PET) have highlighted the vascular component of Alzheimer's disease highlighted by a decrease of the cerebral blood flow jointly with the cognitive decline [138]. More recently, thanks to in vivo optical imaging technique with much higher spatial resolution,, a micro-vascular occlusive process has been proposed as a potential biological mechanism leading to the cognitive decline in mice [21].

In that context, the aim of this thesis has been to unveil the blood flow organization and its transport properties in healthy but also in partially occluded brain micro-vascular networks. Based on highly resolved blood flow simulations in anatomically accurate mouse brain micro-vascular networks, our aim was to understand how the local description of the flow and the structure of the micro-vascular networks interplay to give rise to flow organization and transport properties at the network scale. To do so, we have adopted different statistical physics formalisms appropriate to this objective.

In Chapter 2, we have first highlighted the large distributions of blood flow and transport properties in the brain micro-circulation. We have notably revealed the crucial role of long time transport dynamics in the supply of vital chemical species and on the removal of metabolic wastes.

This observation is one of the key results of this thesis work as no experiment and theoretical approach, until now, has described with such a level of accuracy this part of the transport effectively involved in these vital biological mechanisms. Furthermore, we have ensured the reproducibility and the generality of this observation providing a physical explanation linking the emergence of these flow properties to the structure of micro-vascular networks. Hence, we have shown the close correspondance between the micro-vascular blood flow organization and the one engendered by dipolar flows on random networks. From these insights, we have derived a semi-analytical stochastic model belonging to the class of Continuous Time Random Walks, which accounts for such a non-trivial flow organization. This model is in good agreement with our (reactive) transport simulations and notably with the evolution of the size of regions with pathologically low oxygen and amyloid concentrations.

In Chapter 3, we have investigated the impact of the disordered structure of the homogeneous and space-filling capillary bed on the flow organization. We have demonstrated the presence of local flow anti-correlations adapting a model coming from the physics of granular media, the q-model. Notably, we have shown that these anti-correlations induce a narrowing of the flow fluctuations compared to the mean-field exponential solution of the q-model. Finally, we have established that these anti-correlations result from the limitations of homogenous networks to dissipate high pressure gradients.

In Chapter 4, we have focused on the impact of micro-vascular occlusions on blood flow organization. First, we have demonstrated that the community structure, i.e. substructures with vertices more connected to each other than to other vertices, is a factor of vulnerability of the blood flow supply in micro-vascular networks under localized damages. For this, we have developed a new theoretical framework within the dilute regime of percolation. We have also highlighted the contribution of various sources of complexity present in brain micro-vascular networks, e.g. conductance and topological heterogeneities or multiple inlets and outlets, on blood supply resilience. Our findings highlight that it is difficult to make accurate predictions on the impact of occlusions on blood flow decrease and inlet disconnection probability without accounting for this whole complexity. However some important invariant behavior has appeared. The topology of micro-vascular networks is responsible for a change of behaviour in the global flow rate decrease for about 20% of occluded capillaries. The presence of multiple network inlets and outlets considerably reduces the fluctuations precendently highlighted by our renewed percolation framework. This observation could be seen as a compensatory mechanism aiming to increase the resilience of the blood supply function of micro-vascular networks. The highly conductive tree-like structure of arterioles and venules creates preferential paths which are not altered by capillary occlusions. These robust structures prevent the increase of the global flow reduction after 20% of occlusions and drastically decrease the arteriole disconnecting probability. Eventually, we have shown that occlusions induce large flow perturbations in addition to the global decrease of the flow already highlighted in [21]. We have provided a physical explanation to these perturbations and the first elements of quantification of the magnitude of their impact on the remaining vessels. The work presented in this thesis does not cover all the aspects of the modelling of blood flow and transport in brain micro-vascular networks and some questions or improvements could be interestingly be investigated in the context of future research.

In Chapter 2, we have identified four major issues that would be interesting to be adressed in future research. First, it would be very useful to perform blood flow and transport simulations on larger, and more specifically deeper or even whole brain, cerebral micro-vascular networks to quantify the impact of a change of the system size on the observations that we made in this

work. This would allow to improve the accuracy of our transport model. In the same spirit, it would be also very interesting to have large and anatomically accurate human brain micro-vascular networks to confirm that they have the same transport properties as the mouse networks used here. Secondly, the impact of capillary bed heterogeneities, notably induced by vessel shrinkage [11, 14–17, 20], could be an other interesting perspective to explore specially in the context of Alzheimer’s disease. Like occlusions, vessel shrinkages have been identified as a mechanism leading to cerebral blood flow decrease in Alzheimer’s disease. Investigating the impact of the such vessel diameter modifications on blood flow and transport properties could provide a complementary analysis to the one performed in this thesis. The third question concerns the improvement of the chemical reaction modelling. In this thesis, we have made important simplifying approximations specially for oxygen reaction kinetics. A very promising improvement of this thesis work would be to account for the whole oxygen reaction kinetics within the micro-vasculature and notably to account for the oxygen desorption kinetics from the red blood cells. This could lead to a modelling framework, accounting for all the reactive processes, oxygen desorption as we have already said but also metabolic kinetics, into a single reactive transport model. Finally a further improvement of the transport model that we have designed in this thesis would be the introduction of a spatial dependency of the reactive transport model. This would allow to predict the spatial distribution of concentrations accross the micro-vasculature and to perform local spatial averages providing a description of the concentrations of chemical species in brain tissues. In addition to these four major perspectives, we identify three perspectives slightly apart from this thesis work. First, it would be interesting to obtain accurate experimental data on the late time transport regime, which plays a central role in the onset of brain pathologies. The principal challenge in the production of such data is to prevent the recirculation of the contrast agent. A solution, if realizable, would be to perform the acquisition by multi-photon microscopy of a bolus experiment with non-metabolizable and low diffusible contrast agent in rodents under dialysis. The second perspective concerns the improvement of minimally invasive imaging techniques. We have stated in the State of the Art (Section 2) that the determination of blood flow by minimally invasive imaging techniques was in fact an inverse problem necessitating a “transfer function” to account for unresolved transport processes below the image pixel size. Until here, only empirical functions were used. It would be interesting to see if the physics-based transport framework that we developed in this thesis may provide a new operational tool for these techniques for these techniques. Finally, it would be interesting to see in what extent our transport model can be adapted to other organs or other regions of the brain.

In Chapter 3, the demonstration of the presence of local flow anti-correlations in random flows in homogeneous networks offers also interesting perspectives. First, on a theoretical point of view, the design of a correlated q-model has, to the best of our knowledge, never been performed in the litterature. The resolution of this computational challenge could potentially lead to new classes of solutions for this process that can be used in a wide range of fields from physics of granular media to theoretical chemistry and obviously flows into disordered porous media. On the point of view of flows into disordered porous media, the presence of such anti-correlations raises the question of the potential non-negligible correlations in the sampling of the velocity distribution by Lagrangian particles. This question has already been tackled in the context of transport into heterogeneous disordered porous media, e.g. [81], but not in homogenous disordered porous media. Furthermore, it has been shown in [128] that mass conservation in the q-model induces non-local mass correlations in space and in time. The result of the competition between these correlations and the anti-correlations that we have unveiled in this thesis is an other interesting

question. On the point of view of reactive transport, these anti-correlations are expected to be a passive mechanism leading to the homogeneization of concentrations in homogeneous networks. Indeed, as highest flows have a tendency to mix with lowest ones, we could expect that these anti-correlations induce a tendency of the highest concentrations to be mixed with the lowest ones. This deserves to be investigated in more details. Finally, in the context of micro-vascular circulation, this correlated q-model could be a relevant tool to predict the concentrations of red blood cells accross the micro-vasculature opening new avenues for the description of oxygen supply to brain cells.

In Chapter 4, the design of a renewed percolation framework offers interesting perspectives to predict accurately the perturbation of the blood flow organization in micro-vascular networks in its full complexity. The first generalization step would be to extend this framework to an arbitrary number of micro-vascular inlets and outlets. With this formulation, it will be useful to study or demonstrate the existence of a passive compensatory mechanism between arterioles and between venules. Then, this framework could be generalized to an arbitrary number of occlusions in order to predict the global blood flow decrease induced by a realistic fraction of vessel occlusions to mimick the first stages of Alzheimer's disease. This would be a crucial step in the understanding of the onset and the progression of this disease. The last step would be to account for the whole complexity of the micro-vascular networks but given the parametric dependence on such a large number of micro-vascular network particularities, i.e. a specific conductance distribution in arterioles and venules and a biased sampling of vessels to occlude only capillaries, it is likely that an accurate description of blood flow corrections would not be obtained in an other way than by numerical resolution. Finally, two issues have not yet be addressed. First, it would be interesting to investigate the transition from the first regime to the second one in the decrease of the average blood flow. An analysis of the distribution of cluster sizes and/or an analysis of the number of independant clusters might highlight a (first order) topological transition for 20% of occlusions. If such a transition exists, this would be characterized for instance by the creation of disconnected sub-graphs. This would be a major aspect of the decrease of the resilience of the blood supply function of micro-vascular networks in the case of a moderate fraction of occlusions. Furthermore, it would be interesting to see if the spatial localization of these sub-graphs matches with the spatial localization of the communities that we have unveiled in this thesis. Finally, the quantification of the impact of the flow perturbations induced by capillary occlusions has to be completed in order to predict notably the impact of such perturbations on the distributions of the concentration of chemical species accross the micro-vasculature. For nutrients or oxygen, we expect the emergence of regions with high concentrations, in which the flow has considerably increased, and the emergence of regions with low concentrations, downstream to the regions where the flow has considerably decreased. Conversely, for waste, we expect the emergence of regions with low concentrations, in which the flow has considerably increased, and the emergence of regions with high concentrations, downstream to the regions where the flow has considerably decreased. This mechanism could contribute to alterate the brain metabolic processes with possible link with the progress of neuro-degenerative diseases like Alzheimer's and raises the question of optimal transport in brain micro-vascular networks.

Bibliography

- [1] Karol Miller. *Biomechanics of the Brain*. Springer, 2011.
- [2] Henri M Duvernoy, SLVJ Delon, and JL Vannson. Cortical blood vessels of the human brain. *Brain research bulletin*, 7(5):519–579, 1981.
- [3] Pablo Blinder, Andy Y Shih, Christopher Rafie, and David Kleinfeld. Topological basis for the robust distribution of blood to rodent neocortex. *Proceedings of the National Academy of Sciences*, 107(28):12670–12675, 2010.
- [4] Andy Y Shih, Charlotta Rühlmann, Pablo Blinder, Anna Devor, Patrick J Drew, Beth Friedman, Per M Knutsen, Patrick D Lyden, Celine Mateo, Lisa Mellander, et al. Robust and fragile aspects of cortical blood flow in relation to the underlying angioarchitecture. *Microcirculation*, 22(3):204–218, 2015.
- [5] Henri M Duvernoy. Blood supply of the cerebral cortex. In *The Human Brain*, pages 431–458. Springer, 1999.
- [6] Yoshiki Hase, Ren Ding, Gina Harrison, Emily Hawthorne, Amilia King, Sean Gettings, Charlotte Platten, William Stevenson, Lucinda JL Craggs, and Raj N Kalaria. White matter capillaries in vascular and neurodegenerative dementias. *Acta neuropathologica communications*, 7(1):1–12, 2019.
- [7] Sylvie Lorthois and Francis Cassot. Fractal analysis of vascular networks: insights from morphogenesis. *Journal of theoretical biology*, 262(4):614–633, 2010.
- [8] Amy F Smith, Vincent Doyeux, Maxime Berg, Myriam Peyrounette, Mohammad Haft-Javaherian, Anne-Edith Larue, John H Slater, Frédéric Lauwers, Pablo Blinder, Philbert Tsai, et al. Brain capillary networks across species: a few simple organizational requirements are sufficient to reproduce both structure and function. *Frontiers in physiology*, 10:233, 2019.
- [9] Pablo Blinder, Philbert S Tsai, John P Kaufhold, Per M Knutsen, Harry Suhl, and David Kleinfeld. The cortical angiome: an interconnected vascular network with noncolumnar patterns of blood flow. *Nature neuroscience*, 16(7):889, 2013.
- [10] Sava Sakadžić, Emiri T Mandeville, Louis Gagnon, Joseph J Musacchia, Mohammad A Yaseen, Meryem A Yucel, Joel Lefebvre, Frédéric Lesage, Anders M Dale, Katharina Eikermann-Haerter, et al. Large arteriolar component of oxygen delivery implies a safe margin of oxygen supply to cerebral tissue. *Nature communications*, 5(1):1–11, 2014.
- [11] Costantino Iadecola. Neurovascular regulation in the normal brain and in alzheimer’s disease. *Nature Reviews Neuroscience*, 5(5):347–360, 2004.

- [12] David A Boas, Stephanie R Jones, Anna Devor, Theodore J Huppert, and Anders M Dale. A vascular anatomical network model of the spatio-temporal response to brain activation. *Neuroimage*, 40(3):1116–1129, 2008.
- [13] Francisco Fernández-Klett, Nikolas Offenhauser, Ulrich Dirnagl, Josef Priller, and Ute Lindauer. Pericytes in capillaries are contractile in vivo, but arterioles mediate functional hyperemia in the mouse brain. *Proceedings of the National Academy of Sciences*, 107(51):22290–22295, 2010.
- [14] Catherine N Hall, Clare Reynell, Bodil Gesslein, Nicola B Hamilton, Anusha Mishra, Brad A Sutherland, Fergus M O’Farrell, Alastair M Buchan, Martin Lauritzen, and David Attwell. Capillary pericytes regulate cerebral blood flow in health and disease. *Nature*, 508(7494):55–60, 2014.
- [15] Eszter Farkas and Paul GM Luiten. Cerebral microvascular pathology in aging and alzheimer’s disease. *Progress in neurobiology*, 64(6):575–611, 2001.
- [16] Berislav V Zlokovic. Neurovascular pathways to neurodegeneration in alzheimer’s disease and other disorders. *Nature Reviews Neuroscience*, 12(12):723–738, 2011.
- [17] Philip B Gorelick, Angelo Scuteri, Sandra E Black, Charles DeCarli, Steven M Greenberg, Costantino Iadecola, Lenore J Launer, Stephane Laurent, Oscar L Lopez, David Nyenhuis, et al. Vascular contributions to cognitive impairment and dementia: a statement for health-care professionals from the american heart association/american stroke association. *Stroke*, 42(9):2672–2713, 2011.
- [18] Manon Brundel, Jeroen De Bresser, Jeroen J Van Dillen, L Jaap Kappelle, and Geert Jan Biessels. Cerebral microinfarcts: a systematic review of neuropathological studies. *Journal of Cerebral Blood Flow & Metabolism*, 32(3):425–436, 2012.
- [19] Andy Y Shih, Pablo Blinder, Philbert S Tsai, Beth Friedman, Geoffrey Stanley, Patrick D Lyden, and David Kleinfeld. The smallest stroke: occlusion of one penetrating vessel leads to infarction and a cognitive deficit. *Nature neuroscience*, 16(1):55–63, 2013.
- [20] Leif Østergaard, Thorbjørn S Engedal, Fiona Moreton, Mikkel B Hansen, Joanna M Wardlaw, Turgay Dalkara, Hugh S Markus, and Keith W Muir. Cerebral small vessel disease: capillary pathways to stroke and cognitive decline. *Journal of Cerebral Blood Flow & Metabolism*, 36(2):302–325, 2016.
- [21] Jean C Cruz Hernández, Oliver Bracko, Calvin J Kersbergen, Victorine Muse, Mohammad Haft-Javaherian, Maxime Berg, Laibaik Park, Lindsay K Vinarsik, Iryna Ivasyk, Daniel A Rivera, et al. Neutrophil adhesion in brain capillaries reduces cortical blood flow and impairs memory function in alzheimer’s disease mouse models. *Nature neuroscience*, 22(3):413–420, 2019.
- [22] Y.P. Ma, A. Koo, H.C. Kwan, and K.K. Cheng. On-line measurement of the dynamic velocity of erythrocytes in the cerebral microvessels in the rat. *Microvascular Research*, 8(1):1–13, 1974.

- [23] KP Ivanov, MK Kalinina, and Yu I Levkovich. Blood flow velocity in capillaries of brain and muscles and its physiological significance. *Microvascular research*, 22(2):143–155, 1981.
- [24] RS Frackowiak, GL Lenzi, T Jones, and JD Heather. Quantitative measurement of regional cerebral blood flow and oxygen metabolism in man using ^{15}O and positron emission tomography: theory, procedure, and normal values. *Journal of computer assisted tomography*, 4(6):727–736, December 1980.
- [25] Edgar A. DeYoe, Peter Bandettini, Jay Neitz, David Miller, and Paula Winans. Functional magnetic resonance imaging (fmri) of the human brain. *Journal of Neuroscience Methods*, 54(2):171–187, 1994. Imaging Techniques in Neurobiology.
- [26] Nikos K Logothetis. The underpinnings of the bold functional magnetic resonance imaging signal. *Journal of Neuroscience*, 23(10):3963–3971, 2003.
- [27] Charles Smart Roy and Charles S Sherrington. On the regulation of the blood-supply of the brain. *The Journal of physiology*, 11(1-2):85–158, 1890.
- [28] Megan H Lee, Christopher D Smyser, and Joshua S Shimony. Resting-state fmri: a review of methods and clinical applications. *American Journal of neuroradiology*, 34(10):1866–1872, 2013.
- [29] Bernd J Pichler, Hans F Wehrli, and Martin S Judenhofer. Latest advances in molecular imaging instrumentation. *Journal of Nuclear Medicine*, 49(Suppl 2):5S–23S, 2008.
- [30] Clifford S Patlak, Ronald G Blasberg, and Joseph D Fenstermacher. Graphical evaluation of blood-to-brain transfer constants from multiple-time uptake data. *Journal of Cerebral Blood Flow & Metabolism*, 3(1):1–7, 1983.
- [31] Maithili Sharan, MD Jones, RC Koehler, RJ Traystman, and AS Popel. A compartmental model for oxygen transport in brain microcirculation. *Annals of biomedical engineering*, 17(1):13–38, 1989.
- [32] Mark A Mintun, Brian N Lundstrom, Abraham Z Snyder, Andrei G Vlassenko, Gordon L Shulman, and Marcus E Raichle. Blood flow and oxygen delivery to human brain during functional activity: theoretical modeling and experimental data. *Proceedings of the National Academy of Sciences*, 98(12):6859–6864, 2001.
- [33] Romain Valabrègue, Agnès Aubert, Jacques Burger, Jacques Bittoun, and Robert Costalat. Relation between cerebral blood flow and metabolism explained by a model of oxygen exchange. *Journal of Cerebral Blood Flow & Metabolism*, 23(5):536–545, 2003.
- [34] Agnès Aubert, Robert Costalat, Pierre J Magistretti, and Luc Pellerin. Brain lactate kinetics: modeling evidence for neuronal lactate uptake upon activation. *Proceedings of the National Academy of Sciences*, 102(45):16448–16453, 2005.
- [35] Marcus E Raichle, Ann Mary MacLeod, Abraham Z Snyder, William J Powers, Debra A Gusnard, and Gordon L Shulman. A default mode of brain function. *Proceedings of the National Academy of Sciences*, 98(2):676–682, 2001.

- [36] Scott K Holland, Elena Plante, Anna Weber Byars, Richard H Strawsburg, Vince J Schmithorst, and William S Ball Jr. Normal fmri brain activation patterns in children performing a verb generation task. *Neuroimage*, 14(4):837–843, 2001.
- [37] Matthias JP van Osch, Evert-jan PA Vonken, Ona Wu, Max A Viergever, Jeroen van der Grond, and Chris JG Bakker. Model of the human vasculature for studying the influence of contrast injection speed on cerebral perfusion mri. *Magnetic Resonance in Medicine: An Official Journal of the International Society for Magnetic Resonance in Medicine*, 50(3):614–622, 2003.
- [38] Leif Østergaard, Robert M Weisskoff, David A Chesler, Carsten Gyldensted, and Bruce R Rosen. High resolution measurement of cerebral blood flow using intravascular tracer bolus passages. part i: Mathematical approach and statistical analysis. *Magnetic resonance in medicine*, 36(5):715–725, 1996.
- [39] Leif Østergaard, Robert M Weisskoff, David A Chesler, Carsten Gyldensted, and Bruce R Rosen. High resolution measurement of cerebral blood flow using intravascular tracer bolus passages. part i: Mathematical approach and statistical analysis. *Magnetic resonance in medicine*, 36(5):715–725, 1996.
- [40] Arno Villringer, Andreas Them, Ute Lindauer, K Einhüpl, and Ulrich Dirnagl. Capillary perfusion of the rat brain cortex. an in vivo confocal microscopy study. *Circulation research*, 75(1):55–62, 1994.
- [41] Winfried Denk, James H Strickler, and Watt W Webb. Two-photon laser scanning fluorescence microscopy. *Science*, 248(4951):73–76, 1990.
- [42] Andy Y Shih, Jonathan D Driscoll, Patrick J Drew, Nozomi Nishimura, Chris B Schaffer, and David Kleinfeld. Two-photon microscopy as a tool to study blood flow and neurovascular coupling in the rodent brain. *Journal of Cerebral Blood Flow & Metabolism*, 32(7):1277–1309, 2012.
- [43] Bojana Stefanovic, Elizabeth Hutchinson, Victoria Yakovleva, Vincent Schram, James T Russell, Leonardo Belluscio, Alan P Koretsky, and Afonso C Silva. Functional reactivity of cerebral capillaries. *Journal of Cerebral Blood Flow & Metabolism*, 28(5):961–972, 2008.
- [44] Eugenio Gutiérrez-Jiménez, Changsi Cai, Irene Klærke Mikkelsen, Peter Mondrup Rasmussen, Hugo Angleys, Mads Merrild, Kim Mouridsen, Sune Nørhøj Jespersen, Jonghwan Lee, Nina Kerting Iversen, et al. Effect of electrical forepaw stimulation on capillary transit-time heterogeneity (cth). *Journal of Cerebral Blood Flow & Metabolism*, 36(12):2072–2086, 2016.
- [45] Dominik Obrist, Bruno Weber, Alfred Buck, and Patrick Jenny. Red blood cell distribution in simplified capillary networks. *Philosophical Transactions of the Royal Society A: Mathematical, Physical and Engineering Sciences*, 368(1921):2897–2918, 2010.
- [46] Sune N Jespersen and Leif Østergaard. The roles of cerebral blood flow, capillary transit time heterogeneity, and oxygen tension in brain oxygenation and metabolism. *Journal of cerebral blood flow & metabolism*, 32(2):264–277, 2012.

- [47] Francis Cassot, Frederic Lauwers, Céline Fouard, Steffen Prohaska, and Valerie Lauwers-Cances. A novel three-dimensional computer-assisted method for a quantitative study of microvascular networks of the human cerebral cortex. *Microcirculation*, 13(1):1–18, 2006.
- [48] Laurent Risser, Franck Plouraboué, and Xavier Descombes. Gap filling of 3-d microvascular networks by tensor voting. *IEEE transactions on medical imaging*, 27(5):674–687, 2008.
- [49] Stefan Heinzer, Gisela Kuhn, Thomas Krucker, Eric Meyer, Alexandra Ulmann-Schuler, Marco Stampanoni, Max Gassmann, Hugo H Marti, Ralph Müller, and Johannes Vogel. Novel three-dimensional analysis tool for vascular trees indicates complete micro-networks, not single capillaries, as the angiogenic endpoint in mice overexpressing human vegf165 in the brain. *Neuroimage*, 39(4):1549–1558, 2008.
- [50] Philbert S. Tsai, John P. Kaufhold, Pablo Blinder, Beth Friedman, Patrick J. Drew, Harvey J. Karten, Patrick D. Lyden, and David Kleinfeld. Correlations of neuronal and microvascular densities in murine cortex revealed by direct counting and colocalization of nuclei and vessels. *Journal of Neuroscience*, 29(46):14553–14570, 2009.
- [51] Demirhan Kobat, Nicholas G Horton, and Chris Xu. In vivo two-photon microscopy to 1.6-mm depth in mouse cortex. *Journal of biomedical optics*, 16(10):106014, 2011.
- [52] Nicholas G Horton, Ke Wang, Demirhan Kobat, Catharine G Clark, Frank W Wise, Chris B Schaffer, and Chris Xu. In vivo three-photon microscopy of subcortical structures within an intact mouse brain. *Nature photonics*, 7(3):205–209, 2013.
- [53] Sven Hirsch, Johannes Reichold, Matthias Schneider, Gábor Székely, and Bruno Weber. Topology and hemodynamics of the cortical cerebrovascular system. *Journal of Cerebral Blood Flow & Metabolism*, 32(6):952–967, 2012.
- [54] Timothy W Secomb. Blood flow in the microcirculation. *Annual Review of Fluid Mechanics*, 49:443–461, 2017.
- [55] Robin Fåhræus. The suspension stability of the blood. *Physiological Reviews*, 9(2):241–274, 1929.
- [56] Axel R Pries, Timothy W Secomb, P Gaehtgens, and JF Gross. Blood flow in microvascular networks. experiments and simulation. *Circulation research*, 67(4):826–834, 1990.
- [57] Robin Fahraeus and Torsten Lindqvist. The viscosity of the blood in narrow capillary tubes. *American Journal of Physiology-Legacy Content*, 96(3):562–568, 1931.
- [58] Axel R Pries, Klaus Ley, M Claassen, and P Gaehtgens. Red cell distribution at microvascular bifurcations. *Microvascular research*, 38(1):81–101, 1989.
- [59] AR Pries, Timothy W Secomb, and P Gaehtgens. Biophysical aspects of blood flow in the microvasculature. *Cardiovascular research*, 32(4):654–667, 1996.
- [60] Meongkeun Ju, Swe Soe Ye, Bumseok Namgung, Seungkwan Cho, Hong Tong Low, Hwa Liang Leo, and Sangho Kim. A review of numerical methods for red blood cell flow simulation. *Computer methods in biomechanics and biomedical engineering*, 18(2):130–140, 2015.

- [61] Chenghai Sun and Lance L Munn. Lattice-boltzmann simulation of blood flow in digitized vessel networks. *Computers & Mathematics with Applications*, 55(7):1594–1600, 2008.
- [62] Abtin Rahimian, Ilya Lashuk, Shravan Veerapaneni, Aparna Chandramowlishwaran, Dhairya Malhotra, Logan Moon, Rahul Sampath, Aashay Shringarpure, Jeffrey Vetter, Richard Vuduc, et al. Petascale direct numerical simulation of blood flow on 200k cores and heterogeneous architectures. In *SC’10: Proceedings of the 2010 ACM/IEEE International Conference for High Performance Computing, Networking, Storage and Analysis*, pages 1–11. IEEE, 2010.
- [63] Peter Balogh and Prosenjit Bagchi. Direct numerical simulation of cellular-scale blood flow in 3d microvascular networks. *Biophysical journal*, 113(12):2815–2826, 2017.
- [64] Jean Leonard Poiseuille. *Recherches expérimentales sur le mouvement des liquides dans les tubes de très-petits diamètres*. Imprimerie Royale, 1844.
- [65] Annie Viallat and Manouk Abkarian. *Dynamics of Blood Cell Suspensions in Microflows*. CRC Press, 2019.
- [66] Johannes Reichold, Marco Stampanoni, Anna Lena Keller, Alfred Buck, Patrick Jenny, and Bruno Weber. Vascular graph model to simulate the cerebral blood flow in realistic vascular networks. *Journal of Cerebral Blood Flow & Metabolism*, 29(8):1429–1443, 2009.
- [67] Romain Guibert, Caroline Fonta, and Franck Plouraboué. Cerebral blood flow modeling in primate cortex. *Journal of Cerebral Blood Flow & Metabolism*, 30(11):1860–1873, 2010.
- [68] Lauwers F Lorthois S, Cassot F. Simulation study of brain blood flow regulation by intra-cortical arterioles in an anatomically accurate large human vascular network: Part i: methodology and baseline flow. *Neuroimage*, 54(2):1031–1042, 2011.
- [69] Sylvie Lorthois, Francis Cassot, and Frédéric Lauwers. Simulation study of brain blood flow regulation by intra-cortical arterioles in an anatomically accurate large human vascular network. part ii: flow variations induced by global or localized modifications of arteriolar diameters. *Neuroimage*, 54(4):2840–2853, 2011.
- [70] Myriam Peyrounette, Yohan Davit, Michel Quintard, and Sylvie Lorthois. Multiscale modelling of blood flow in cerebral microcirculation: Details at capillary scale control accuracy at the level of the cortex. *PloS one*, 13(1):e0189474, 2018.
- [71] Rebecca J Shipley, Amy F Smith, Paul W Sweeney, Axel R Pries, and Timothy W Secomb. A hybrid discrete–continuum approach for modelling microcirculatory blood flow. *Mathematical medicine and biology: a journal of the IMA*, 37(1):40–57, 2020.
- [72] Michel Quintard and Stephen Whitaker. Transport in ordered and disordered porous media: volume-averaged equations, closure problems, and comparison with experiment. *Chemical Engineering Science*, 48(14):2537–2564, 1993.
- [73] M. Berg, Y. Davit, M. Quintard, and S. Lorthois. Modelling solute transport in the brain microcirculation: is it really well mixed inside the blood vessels? *Journal of Fluid Mechanics*, 884:A39, 2020.

- [74] Jacob Bear. *Dynamics of fluids in porous media*. Courier Corporation, 2013.
- [75] Muhammad Sahimi. *Flow and transport in porous media and fractured rock: from classical methods to modern approaches*. John Wiley & Sons, 2011.
- [76] A-RA Khaled and K Vafai. The role of porous media in modeling flow and heat transfer in biological tissues. *International Journal of Heat and Mass Transfer*, 46(26):4989–5003, 2003.
- [77] Karen Alim. Fluid flows shaping organism morphology. *Philosophical Transactions of the Royal Society B: Biological Sciences*, 373(1747):20170112, 2018.
- [78] Marco Dentz, Peter K Kang, Alessandro Comolli, Tanguy Le Borgne, and Daniel R Lester. Continuous time random walks for the evolution of lagrangian velocities. *Physical Review Fluids*, 1(7):074004, 2016.
- [79] SN Coppersmith, C-h Liu, Satya Majumdar, Onuttom Narayan, and TA Witten. Model for force fluctuations in bead packs. *Physical Review E*, 53(5):4673, 1996.
- [80] Scott Kirkpatrick. Percolation and conduction. *Reviews of modern physics*, 45(4):574, 1973.
- [81] Peter K Kang, Marco Dentz, Tanguy Le Borgne, and Ruben Juanes. Spatial markov model of anomalous transport through random lattice networks. *Physical review letters*, 107(18):180602, 2011.
- [82] Karen Alim, Shima Parsa, David A Weitz, and Michael P Brenner. Local pore size correlations determine flow distributions in porous media. *Physical review letters*, 119(14):144501, 2017.
- [83] Elliott W Montroll and George H Weiss. Random walks on lattices. ii. *Journal of Mathematical Physics*, 6(2):167–181, 1965.
- [84] Albert Einstein. *Investigations on the Theory of the Brownian Movement*. Courier Corporation, 1956.
- [85] V Balakrishnan and M Khantha. First passage time and escape time distributions for continuous time random walks. *Pramana*, 21(3):187–200, 1983.
- [86] Gennady Margolin and Brian Berkowitz. Continuous time random walks revisited: first passage time and spatial distributions. *Physica A: Statistical Mechanics and its Applications*, 334(1-2):46–66, 2004.
- [87] B Meyer, C Chevalier, R Voituriez, and O Bénichou. Universality classes of first-passage-time distribution in confined media. *Physical Review E*, 83(5):051116, 2011.
- [88] Harvey Scher and Melvin Lax. Stochastic transport in a disordered solid. i. theory. *Physical Review B*, 7(10):4491, 1973.
- [89] Enrico Scalas. The application of continuous-time random walks in finance and economics. *Physica A: Statistical Mechanics and its Applications*, 362(2):225–239, 2006.

- [90] Stefan Wieland, Tomas Aquino, and Ana Nunes. The structure of coevolving infection networks. *EPL (Europhysics Letters)*, 97(1):18003, 2012.
- [91] Felix Höfling and Thomas Franosch. Anomalous transport in the crowded world of biological cells. *Reports on Progress in Physics*, 76(4):046602, 2013.
- [92] Brian Berkowitz, Andrea Cortis, Marco Dentz, and Harvey Scher. Modeling non-fickian transport in geological formations as a continuous time random walk. *Reviews of Geophysics*, 44(2), 2006.
- [93] VM Kenkre, EW Montroll, and MF Shlesinger. Generalized master equations for continuous-time random walks. *Journal of Statistical Physics*, 9(1):45–50, 1973.
- [94] Tomás Aquino and Marco Dentz. Chemical continuous time random walks. *Physical review letters*, 119(23):230601, 2017.
- [95] Tanguy Le Borgne, Marco Dentz, and Jesus Carrera. Lagrangian statistical model for transport in highly heterogeneous velocity fields. *Physical review letters*, 101(9):090601, 2008.
- [96] Marco Dentz, Peter K Kang, and Tanguy Le Borgne. Continuous time random walks for non-local radial solute transport. *Advances in water resources*, 82:16–26, 2015.
- [97] C-h Liu, Sydney R Nagel, DA Schecter, SN Coppersmith, Satya Majumdar, Onuttom Narayan, and TA Witten. Force fluctuations in bead packs. *Science*, 269(5223):513–515, 1995.
- [98] Ascânio D Araújo, Wagner B Bastos, José S Andrade Jr, and Hans J Herrmann. Distribution of local fluxes in diluted porous media. *Physical Review E*, 74(1):010401, 2006.
- [99] M von Smoluchowski. Drei vortrage uber diffusion, brownsche bewegung und koagulation von kolloidteilchen. *Zeitschrift fur Physik*, 17:557–585, 1916.
- [100] A Vledouts, N Vandenberghe, and E Villermaux. Fragmentation as an aggregation process. *Proceedings of the Royal Society A: Mathematical, Physical and Engineering Sciences*, 471(2184):20150678, 2015.
- [101] Kyle Kawagoe, Greg Huber, Marc Pradas, Michael Wilkinson, Alain Pumir, and Eli Ben-Naim. Aggregation-fragmentation-diffusion model for trail dynamics. *Physical Review E*, 96(1):012142, 2017.
- [102] Pietro de Anna, Bryan Quaife, George Biros, and Ruben Juanes. Prediction of the low-velocity distribution from the pore structure in simple porous media. *Physical Review Fluids*, 2(12):124103, 2017.
- [103] Simon R Broadbent and John M Hammersley. Percolation processes: I. crystals and mazes. In *Mathematical proceedings of the Cambridge philosophical society*, volume 53, pages 629–641. Cambridge University Press, 1957.
- [104] BJ Last and DJ Thouless. Percolation theory and electrical conductivity. *Physical review letters*, 27(25):1719, 1971.

- [105] Scott Kirkpatrick. Classical transport in disordered media: scaling and effective-medium theories. *Physical Review Letters*, 27(25):1722, 1971.
- [106] Geoffrey Grimmett. What is percolation? In *Percolation*, pages 1–31. Springer, 1999.
- [107] Duncan S Callaway, Mark EJ Newman, Steven H Strogatz, and Duncan J Watts. Network robustness and fragility: Percolation on random graphs. *Physical review letters*, 85(25):5468, 2000.
- [108] Steven H Strogatz. Exploring complex networks. *nature*, 410(6825):268–276, 2001.
- [109] Reuven Cohen, Keren Erez, Daniel Ben-Avraham, and Shlomo Havlin. Breakdown of the internet under intentional attack. *Physical review letters*, 86(16):3682, 2001.
- [110] Reuven Cohen, Daniel Ben-Avraham, and Shlomo Havlin. Percolation critical exponents in scale-free networks. *Physical Review E*, 66(3):036113, 2002.
- [111] Xuqing Huang, Jianxi Gao, Sergey V Buldyrev, Shlomo Havlin, and H Eugene Stanley. Robustness of interdependent networks under targeted attack. *Physical Review E*, 83(6):065101, 2011.
- [112] Peng Zhang, Baisong Cheng, Zhuang Zhao, Daqing Li, Guangquan Lu, Yunpeng Wang, and Jinghua Xiao. The robustness of interdependent transportation networks under targeted attack. *EPL (Europhysics Letters)*, 103(6):68005, 2013.
- [113] Alfredo Braunstein, Luca Dall’Asta, Guilhem Semerjian, and Lenka Zdeborová. Network dismantling. *Proceedings of the National Academy of Sciences*, 113(44):12368–12373, 2016.
- [114] Xiao-Long Ren, Niels Gleinig, Dirk Helbing, and Nino Antulov-Fantulin. Generalized network dismantling. *Proceedings of the national academy of sciences*, 116(14):6554–6559, 2019.
- [115] Nicholas C Wormald et al. Models of random regular graphs. *London Mathematical Society Lecture Note Series*, pages 239–298, 1999.
- [116] Allen J Wood, Bruce F Wollenberg, and Gerald B Sheblé. *Power generation, operation, and control*. John Wiley & Sons, 2013.
- [117] Debsankha Manik, Martin Rohden, Henrik Ronellenfitsch, Xiaozhu Zhang, Sarah Hallerberg, Dirk Witthaut, and Marc Timme. Network susceptibilities: Theory and applications. *Physical Review E*, 95(1):012319, 2017.
- [118] Tatyana Gavrilchenko and Eleni Katifori. Resilience in hierarchical fluid flow networks. *Physical Review E*, 99(1):012321, 2019.
- [119] Richard J O’Brien and Philip C Wong. Amyloid precursor protein processing and alzheimer’s disease. *Annual review of neuroscience*, 34:185–204, 2011.
- [120] Rachel Potter, Bruce W Patterson, Donald L Elbert, Vitaliy Ovod, Tom Kasten, Wendy Sigurdson, Kwasi Mawuenyega, Tyler Blazey, Alison Goate, Robert Chott, et al. Increased in vivo amyloid- β 42 production, exchange, and loss in presenilin mutation carriers. *Science translational medicine*, 5(189):189ra77–189ra77, 2013.

- [121] Peter Atkins and Julio De Paula. *Physical chemistry for the life sciences*. Oxford University Press, USA, 2011.
- [122] Felix J Meigel and Karen Alim. Flow rate of transport network controls uniform metabolite supply to tissue. *Journal of The Royal Society Interface*, 15(142):20180075, 2018.
- [123] Abe Sklar. Random variables, joint distribution functions, and copulas. *Kybernetika*, 9(6):449–460, 1973.
- [124] Umberto Cherubini, Elisa Luciano, and Walter Vecchiato. *Copula methods in finance*. John Wiley & Sons, 2004.
- [125] Anne-Catherine Favre, Salaheddine El Adlouni, Luc Perreault, Nathalie Thiémonge, and Bernard Bobée. Multivariate hydrological frequency analysis using copulas. *Water resources research*, 40(1), 2004.
- [126] CP Haslauer, P Guthke, A Bárdossy, and EA Sudicky. Effects of non-gaussian copula-based hydraulic conductivity fields on macrodispersion. *Water Resources Research*, 48(7), 2012.
- [127] Arash Massoudieh, Marco Dentz, and Jamal Alikhani. A spatial markov model for the evolution of the joint distribution of groundwater age, arrival time, and velocity in heterogeneous media. *Water Resources Research*, 53(7):5495–5515, 2017.
- [128] R Rajesh and Satya N Majumdar. Exact calculation of the spatiotemporal correlations in the takayasu model and in the q model of force fluctuations in bead packs. *Physical Review E*, 62(3):3186, 2000.
- [129] Mohamad El Amki, Chaim Glück, Nadine Binder, William Middleham, Matthias T Wyss, Tobias Weiss, Hanna Meister, Andreas Luft, Michael Weller, Bruno Weber, et al. Neutrophils obstructing brain capillaries are a major cause of no-reflow in ischemic stroke. *Cell Reports*, 33(2):108260, 2020.
- [130] Brian Karrer, Elizaveta Levina, and Mark EJ Newman. Robustness of community structure in networks. *Physical review E*, 77(4):046119, 2008.
- [131] Marcel Salathé and James H Jones. Dynamics and control of diseases in networks with community structure. *PLoS Comput Biol*, 6(4):e1000736, 2010.
- [132] Randi H Griffin and Charles L Nunn. Community structure and the spread of infectious disease in primate social networks. *Evolutionary Ecology*, 26(4):779–800, 2012.
- [133] Yingying Duan and Feng Lu. Structural robustness of city road networks based on community. *Computers, Environment and Urban Systems*, 41:75–87, 2013.
- [134] Oriol Lordan, Jose M Sallan, Pep Simo, and David Gonzalez-Prieto. Robustness of the air transport network. *Transportation Research Part E: Logistics and Transportation Review*, 68:155–163, 2014.
- [135] Sebastian Wandelt, Xing Shi, and Xiaoqian Sun. Estimation and improvement of transportation network robustness by exploiting communities. *Reliability Engineering & System Safety*, 206:107307, 2021.

- [136] Steffen Bohn and Marcelo O Magnasco. Structure, scaling, and phase transition in the optimal transport network. *Physical review letters*, 98(8):088702, 2007.
- [137] Antal G Hudetz. Percolation phenomenon: the effect of capillary network rarefaction. *Microvascular research*, 45(1):1–10, 1993.
- [138] Yasser Iturria-Medina, Roberto C Sotero, Paule J Toussaint, José María Mateos-Pérez, and Alan C Evans. Early role of vascular dysregulation on late-onset alzheimer’s disease based on multifactorial data-driven analysis. *Nature communications*, 7(1):1–14, 2016.

Abstract Micro-vascular networks play a key role in the blood supply to brain cells: they ensure an accurate delivery of oxygen and nutrients and the removal of toxic metabolic wastes. The joint alterations of these networks and of the cerebral micro-circulation have been recently highlighted as a critical mechanism in cognitive decline in (micro-)strokes or neuro-degenerative diseases like Alzheimer's. However, little is known about how the structure of brain micro-vascular networks influences the blood flow organization and its transport properties.

In a first part, we demonstrate that the micro-vascular structure drives the blood flow organization similarly to dipole flows on random networks. This organization implies anomalous transport properties characterized by a broad distribution of Lagrangian particle travel times in the micro-vasculature. These transport properties are successfully captured by our Continuous Time Random Walk model which predicts notably the non-linear increase of the size of areas with abnormal concentrations of oxygen or metabolic wastes with global blood flow reduction. In a second part, we highlight the presence of local flow anti-correlations in homogeneous random networks. We demonstrate, thanks to the q-model framework, that these anti-correlations result from the limitations of such networks to dissipate the pressure along their edges. In a final part, we highlight that the spatialized community structure of micro-vascular networks weakens their resilience to vessel occlusions compared to unstructured random networks. We quantify the role of these communities thanks to the design of a model inspired by percolation theory which allows to account for micro-vascular flow and structure heterogeneities. Furthermore, we show the existence of large flow perturbations induced by vessel occlusions. This work provides new theoretical tools to understand the onset and/or the progression of neuro-degenerative diseases.

Résumé Les réseaux micro-vasculaires jouent un rôle clé dans l'apport sanguin aux cellules cérébrales : ils assurent un approvisionnement précis en oxygène et nutriments et l'évacuation des déchets métaboliques toxiques. Les altérations conjointes de ces réseaux et de la micro-circulation cérébrale ont été récemment mises en évidence comme un mécanisme critique dans le déclin des capacités cognitives lors de (micro) accidents vasculaires cérébraux ou de maladies neuro-dégénératives comme la maladie d'Alzheimer. Cependant, le lien entre la structure des réseaux micro-vasculaires cérébraux, l'organisation de l'écoulement sanguin et ses propriétés de transport reste un mystère.

Dans une première partie, nous démontrons que la structure micro-vasculaire détermine l'organisation de l'écoulement sanguin similairement à un écoulement dipolaire sur un réseau aléatoire. Cette organisation implique des propriétés de transport anormales caractérisées par une distribution large des temps de trajet des particules lagrangiennes dans la micro-vasculature. Ces propriétés de transport sont capturées avec succès par notre modèle de Marcheur Aléatoire en Temps Continu qui prédit notamment l'augmentation non-linéaire de la taille des régions présentant des concentrations anormales en oxygène ou en déchets métaboliques avec la diminution du débit sanguin global. Dans une seconde partie, nous dévoilons la présence d'anti-corrélations, localement dans l'écoulement, dans les réseaux aléatoires homogènes. Nous démontrons, grâce au cadre théorique du q-modèle, que ces anti-corrélations résultent de la limitation de ces réseaux à dissiper la pression le long de leurs liens. Dans une dernière partie, nous dévoilons que la structure en communautés spatialisées des réseaux micro-vasculaires fragilise leur résilience à l'occlusion de vaisseaux par rapport à des réseaux aléatoires non-structurés. Nous quantifions le rôle de ces communautés grâce au développement d'un modèle inspiré de la théorie de la percolation qui permet la prise en compte des hétérogénéités de structure et d'écoulement dans la micro-vasculature. Enfin, nous montrons l'existence de larges perturbations de l'écoulement induites par ces occlusions. Ce travail fournit de nouveaux outils théoriques pour comprendre le déclenchement et/ou la progression de maladies neuro-dégénératives.